

Basal crevasses and suture zones in the Larsen C Ice Shelf, Antarctica:

Implications for ice shelf stability in a warming climate

by

Daniel J. McGrath

B.A. Bowdoin College, 2006

M.A. University of Colorado Boulder, 2009

A thesis submitted to the

Faculty of the Graduate School of the

University of Colorado in partial fulfillment

of the requirement for the degree of

Doctor of Philosophy

Department of Geography

2013

**This thesis titled:
Basal crevasses and suture zones in the Larsen C Ice Shelf, Antarctica:
Implications for ice shelf stability in a warming climate,
written by Daniel J. McGrath
has been approved for the Department of Geography by:**

Dr. Konrad Steffen (Geography)

Dr. Waleed Abdalati (Geography)

Dr. Mark Serreze (Geography)

Dr. Ted Scambos (NSIDC/Geography)

Dr. Harihar Rajaram (Civil, Environmental, and Architectural Engineering)

Date _____

**The final copy of this thesis has been examined by the signatories, and we find that
both the content and the form meet acceptable presentation standards
of scholarly work in the above mentioned discipline.**

McGrath, Daniel J. (Ph.D., Geography)

Basal crevasses and suture zones in the Larsen C Ice Shelf, Antarctica: Implications for ice shelf stability in a warming climate

Thesis directed by Professor Konrad Steffen

Understanding ice shelf structure and processes is paramount to future predictions of sea level rise, as nearly 75% of the ice flux from the Antarctic Ice Sheet (AIS) passes through these gates. The breakup of an ice shelf removes the longitudinal back stress acting on the grounded inland ice and leads to flow acceleration, dynamic thinning and frontal retreat, processes that can be sustained for more than a decade. Increased ice discharge to the ocean contributes to global sea level rise. This dissertation investigates basal crevasses and suture zones, two key structural components of ice shelves, in order to understand how the structure of an ice shelf influences its stability in a warming climate. Ground penetrating radar, high-resolution satellite imagery and a variety of modeling approaches are utilized to assess these features on the Larsen C Ice Shelf but in a manner that considers their influence on ice shelf stability around the AIS. Basal crevasses are large-scale (~66% of ice thickness and ten's of kms in length) and abundant features that are significant structural weaknesses. The viscoplastic deformation of the ice shelf in response to the perturbed hydrostatic balance leads to the formation of both surface depressions and crevasses, hence weakening the ice shelf further. Basal crevasses increase the local ice-ocean interface by ~30%, thereby increasing basal roughness and altering ice-ocean interactions. Ice-shelf fractures frequently terminate where they encounter suture zones, regions of material heterogeneity that form at the lateral bounds

of meteoric inflows to ice shelves. The termination of a 25 km-long rift in the Churchill Peninsula suture zone is investigated and found to contain ~60 m of accreted marine ice. Steady-state basal melting/freezing rates are determined for the ice shelf and applied to a flowline model to examine the along-flow evolution of ice shelf structure. The thickening surface wedge of locally accumulated meteoric ice, which likely has limited lateral variation in its mechanical properties, accounts for ~60% of the total ice thickness near the calving front. This suggests that the material heterogeneities present in the lower ~40% of the ice column are responsible for resisting fracture propagation and thereby delaying tabular calving events. This represents a highly sensitive aspect of ice-shelf stability, as changes in the oceanic forcing may lead to the loss of this heterogeneity.

Acknowledgments

I thank my adviser Dr. Konrad Steffen for the guidance, encouragement, intellectual freedom and financial support to complete my dissertation. This work would not have been possible without the additional support of my committee members, including Dr. Ted Scambos, Dr. Waleed Abdalati, Dr. Hari Rajaram and Dr. Mark Serreze. Each of you made important contributions to this work and to my development as a scientist.

Numerous other individuals have provided either important insight or supportive words at key times, including Dr. Paul Holland, Dr. Jay Zwally, Dr. Doug MacAyeal, Dr. Bob Jacobel and Dr. Eric Rignot. I thoroughly enjoyed working with and learning from my fellow graduate students, including Dr. Liam Colgan, Dr. Atsu Muto, Nicolas Bayou, Dr. John Adler and Dr. Thomas Phillips. Field research support from the British Antarctic Survey and in particular, the personnel of Rothera Research Station, including Tom Weston, Paul (Toddy) Terode, Tamsin Gray, Andy Barker and the Twin Otter pilots made working on Larsen C a productive and enjoyable experience. I am indebted to Dr. Collin Roesler at Bowdoin College for sending me down this road with her class “Poles Apart: Comparing the Arctic and Antarctic” and Dr. Don Perovich for providing my first polar research experience in Barrow, Alaska.

I am thankful for the support and encouragement of my family throughout these years. You’ve made it incredibly easy to follow my dreams. Lastly, but certainly not least, my girlfriend, Stephanie Engel has provided loving support during this journey. Thank you!

This work was funded by the National Science Foundation IPY project 0732946.

Table of Contents

1. Introduction.....	1
1.1 – Antarctic Climate.....	1
1.1.1 – Paleoclimate Overview.....	1
1.1.2 – Large-scale Atmospheric and Oceanic Circulation.....	5
1.1.3 – Observed Changes since 1950.....	7
1.1.4 – Antarctic Peninsula.....	11
1.1.5 – Recent Cooler Conditions on the Antarctic Peninsula.....	15
1.2 – Ice Sheet Mass Balance.....	20
1.2.1 – Antarctic Mass Balance.....	20
1.2.2 – Antarctic Peninsula Mass Balance.....	22
1.3 – Ice Shelves: Properties and Processes.....	24
1.4 – Thesis Impetus.....	29
2. Basal crevasses and associated surface crevassing on the Larsen C Ice Shelf, Antarctica and their role in ice shelf instability.....	31
2.1 – Introduction.....	32
2.2 – Study Site.....	35
2.3 – Methods.....	37
2.3.1 – Data Acquisition and Processing.....	37
2.3.2 – Basal Crevasse Propagation Model.....	39
2.4 – Results.....	40
2.4.1 – Radar Survey.....	40

2.4.2 – Satellite Imagery.....	42
2.4.3 – Model.....	44
2.5 – Discussion.....	46
2.6 – Conclusions.....	55
3. Basal crevasses on the Larsen C Ice Shelf, Antarctica: Implications for meltwater ponding and hydrofracture.....	57
3.1 – Introduction.....	58
3.2 – Methods.....	61
3.3 – Results and Discussion.....	62
3.4 – Implications.....	67
3.5 – Elastic Beam Model.....	72
4. The structure and effect of suture zones in the Larsen C Ice Shelf, Antarctica...75	75
4.1 – Introduction.....	76
4.2 – Radar Survey.....	85
4.2.1 – Methods.....	85
4.2.2 – Radar Observations.....	86
4.3 – Evolution of ice shelf structure.....	92
4.3.1 – Basal melting/freezing rates.....	92
4.3.2 – Along-flow evolution.....	95
4.4 – Discussion.....	100
4.5 – Conclusions.....	108

5. Summary and Future Directions.....	109
5.1 – Summary.....	109
5.2 – Future Directions.....	113
References.....	117

List of Tables

1.1.....19

List of Figures

1.1.....	4
1.2.....	8
1.3.....	18
1.4.....	21
2.1.....	36
2.2.....	41
2.3.....	43
2.4.....	45
2.5.....	47
3.1.....	60
3.2.....	63
3.3.....	65
3.4.....	68
3.5.....	74
4.1.....	77
4.2.....	79
4.3.....	82
4.4.....	84
4.5.....	88
4.6.....	91
4.7.....	94
4.8.....	98

4.9.....	105
4.10.....	107

Chapter 1

Introduction

1.1 - Antarctic Climate

1.1.1 - Paleoclimate Overview

The Antarctic Ice Sheet (AIS) first formed around 34 million years ago (Ma) in response to an atmospheric cooling of ~ 3 °C, although temperatures were still likely ~ 4 °C warmer than present (*SCAR*, 2009). The ice sheet expanded to the continental edge during this time, although it was likely thinner and warmer than its modern configuration. This is in stark contrast to the lush forests and dinosaurs that inhabited Antarctica during the Cretaceous Period (140 Ma to 66 Ma), at a time when CO₂ concentrations ranged from 3000 ppm to 1000 ppm (*SCAR*, 2009). Continental drift isolated Antarctica around 14 Ma, allowing the Antarctic Circumpolar Current (ACC) to form, further increasing the physical and thermal isolation of the continent (*SCAR*, 2009). This contributed to the ice sheet approaching its current state. During the Pliocene (5-3 Ma), CO₂ levels were ~ 400 ppm, resulting in higher temperatures and reduced continental ice, which consequently raised sea levels 15-25 m higher than today (*SCAR*, 2009).

The past 1.8 Ma have been characterized by long intervals of cold temperatures, known as glacial periods, followed by rapid transitions to warm interglacial periods.

Atmospheric warming of 2-5 °C during interglacial periods melted continental ice and caused global sea levels to rise by 4-6 m (*SCAR*, 2009). The cyclic nature of glacial-interglacial periods is driven by variations in the Earth's orbit around the Sun, known as the Milankovitch cycles, which occur at frequencies of 20,000, 41,000 and 100,000 years.

Around 1 Ma, this cycle switched from being dominated by a 41,000-year cycle to a 100,000-year cycle, the cause of which is still not fully understood. The most recent interglacial, the Eemian, lasted from 130,000 to 114,000 years ago and resulted in sea levels 4-6 m higher than present (*Overpeck et al., 2006*). A recent ice core showed that Greenland thinned less than previously thought during this period and therefore, contributed less to documented sea level rise (*Dahl-Jensen et al., 2012*). This in turn implies that Antarctica likely contributed between 2-4 m of global sea level rise during this time, as had been previously suggested (*Overpeck et al., 2006*). The Last Glacial Maximum occurred 21,000 years before present, during which the AIS expanded to the edge of the continental shelf, which in combination with the growth of Northern Hemisphere continental ice lowered global sea level by 125-130 m (*Clark et al., 2009*). Onset of deglaciation for the West Antarctic Ice Sheet (WAIS) began between 15,000-14,000 years ago and likely contributed to an abrupt rise in sea level ~14,500 years ago (*Clark et al., 2009*).

The current interglacial period, which began with this deglaciation and continues to present, is referred to as the Holocene. During the early-Holocene climatic optimum (12,000 to 9,200 years ago), temperatures were 1.3 ± 0.3 °C warmer than present on the northern Antarctic Peninsula (AP; *Mulvaney et al., 2012*). At the end of this warm period, the George VI Ice Shelf collapsed, although evidence suggests it coincided with the arrival of warm, sub polar waters on the western side of the AP, suggesting that this ice shelf may be most sensitive to oceanic forcings (Figure 1.1; *Bentley et al., 2009*). Following this climatic optimum, temperatures cooled slightly on the AP, reaching

temperatures comparable to today, and were largely stable from 9,200 to 2,500 years ago (Mulvaney *et al.*, 2012). Some evidence suggests a second warm period also occurred from 4,500 to 2,800 years ago although much of the evidence comes from either sub polar regions or marine sources (Bentley *et al.*, 2009). From 2,500 years ago to present, the AP climate exhibited strong east-west anomalies, with the east side first cooling, reaching temperatures 0.7 ± 0.3 °C cooler than present, although on the decadal scale it may have been as much as 1.8 ± 0.3 °C cooler than present (Mulvaney *et al.*, 2012). Marine sediment temperature reconstructions from the western AP suggest an equally large but positive anomaly during this time (Shevenell *et al.*, 2011). Sustained warming began 600 years ago on the peninsula, with a pre-anthropogenic increase of 0.22 ± 0.06 °C per century from A.D. 1410 to 1850 (Mulvaney *et al.*, 2012). There is some evidence for a Little Ice Age signal on the peninsula, largely in the form of more persistent sea ice coverage and the advance of certain glaciers and ice shelves on the northern AP, but lacks the spatial coherency found in the Northern Hemisphere (Bentley *et al.*, 2009). Over the past 100 years, the northern AP has warmed by 1.56 ± 0.42 °C, although 1.3 ± 0.6 °C of this warming has occurred in the last 50 years (Mulvaney *et al.*, 2012).

Ice shelf extent and stability has fluctuated throughout the Holocene in response to climatic forcings and therefore provides an important context for the recent observed changes. Prince Gustav Channel, along the northeastern edge of the peninsula, alternated between ice-free and ice shelf conditions from ~10,000 years ago to 1,500 years ago, at which point, atmospheric cooling led to a persistent ice shelf until its collapse in 1995

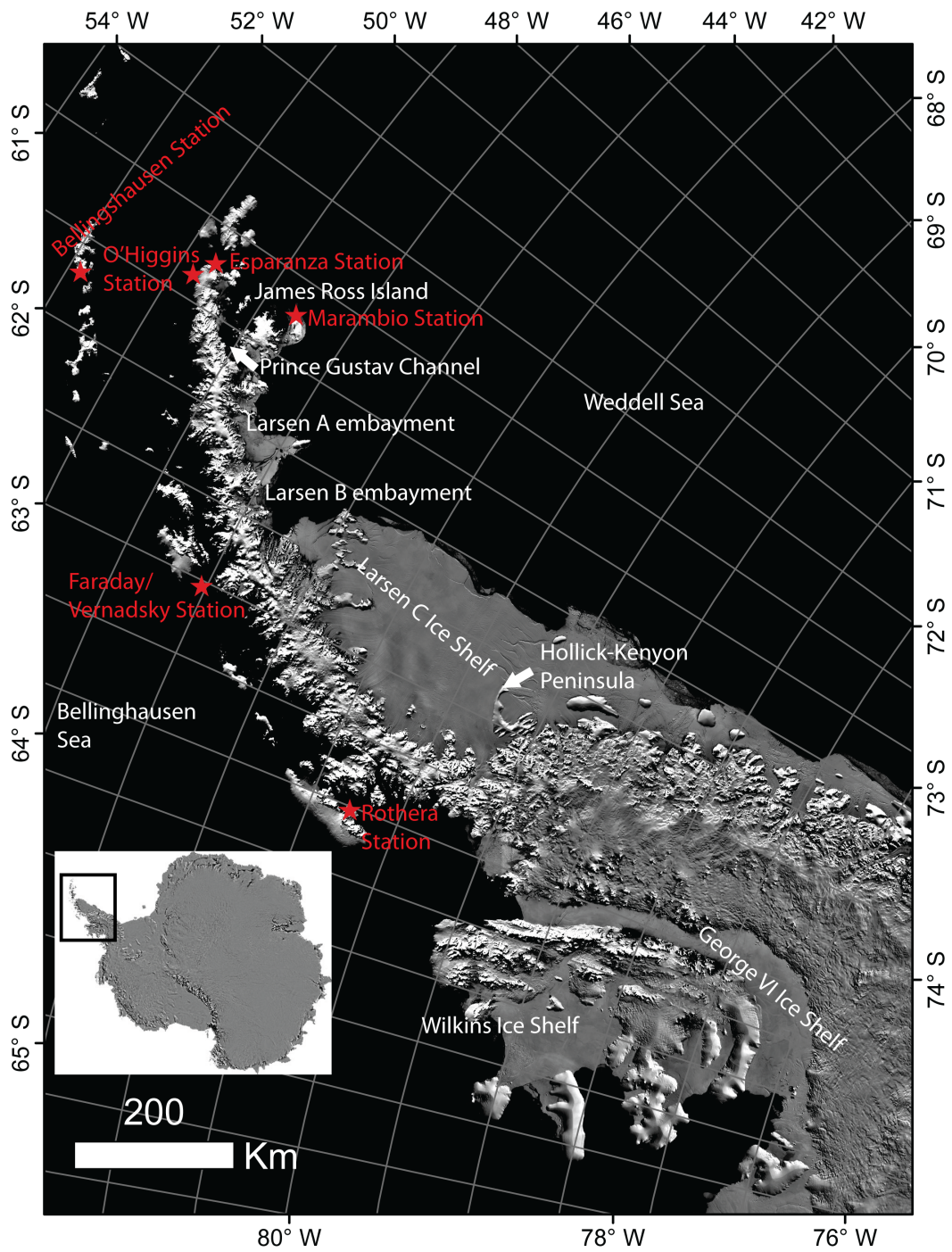


Figure 1.1. MODIS Mosaic of Antarctica (MOA; Haran et al., 2005) of the Antarctic Peninsula with prominent geographic features and research stations labeled. Inset: Location of the Antarctic Peninsula on the continent.

(Figure 1.1; *Mulvaney et al.*, 2012). Further south, the Larsen A Ice Shelf was largely stable throughout the Holocene, except for a period of instability from 3,800 to 1,400 years ago, prior to its collapse in 1995 (*Mulvaney et al.*, 2012). Lastly, the Larsen B Ice Shelf persisted throughout the entire Holocene prior to its collapse in 2002 (*Domack et al.*, 2005). Together, the synchronous collapse of these ice shelves in the past two decades is compelling evidence of the anomalous warming of the past half-century in comparison to the rest of the Holocene (*Hodgson*, 2011).

1.1.2 – Large-scale Atmospheric and Oceanic Circulation in the Southern Hemisphere

The modern day climate of Antarctica is defined by three major characteristics: i) isolation from warm air and water masses of lower latitudes by the strong zonal flow around the continent, ii) strong seasonality in the energy balance, and iii) a highly reflective snow and ice covered surface. The net transfer of energy from the equator to the poles occurs through a series of large cells of rising and falling air masses, called the Hadley, Ferrell and Polar cells. Most importantly for Antarctica is the strong pressure gradient between the sub tropics and higher latitudes (60-65°), that gives rise to the mid-latitude westerlies and the eastward flowing Antarctic Circumpolar Current (ACC), which primarily transports Circumpolar Deep Water (CDW). The ACC completely encircles the globe and transports $\sim 140 \times 10^6 \text{ m}^3 \text{ s}^{-1}$ (140 Sverdrups), making it the largest ocean current in the world (*SCAR*, 2009). This current, combined with the atmospheric westerlies, cause significant thermal isolation of the continent. Likewise, the pressure gradient between the high pressure over the continent and the low pressure at 60-65°

drives the strong easterly winds that flow close to the continent edge, resulting in the westward directed Antarctic Coastal Current near the continent edge. The easterlies are supported by the cold surface winds flowing off the continent, known as katabatics, which arise due to the strong cooling of air over the ice sheet interior that subsequently flows downslope and is deflected to the left due to the Coriolis force (*King and Turner, 1997*).

While Antarctica is largely buffered from air and water masses from the lower latitudes, the formation of Antarctic Bottom Water (AABW) at the edge of continent has a major influence throughout the globe. Strong katabatic winds flowing off the continent cool the surrounding oceans and lead to the formation of sea ice. Freezing rejects salt from the crystalline structure, yielding cold and saline water, which sinks to form AABW (*King and Turner, 1997*). AABW is the densest and one of the most widespread water masses in the world's oceans (*Colling, 2001*).

The surface energy balance of Antarctica differs substantially from most other regions of the world due to the strong seasonality of incoming shortwave radiation and the highly reflective snow and ice surface. On average, the mean annual surface energy balance (SEB) of the AIS is negative, leading to a cooling of surface and lower atmosphere and the subsequent development of strong katabatic circulation (*King and Turner, 1997; van den Broeke et al., 2006*). The negative SEB is primarily driven by: i) a highly reflective snow surface with an average albedo of 0.8-0.9, which limits the absorption of shortwave radiation at the surface and ii) a high surface emissivity coupled with a cold and dry

atmosphere (typically low cloud extent), which leads to a consistently negative net longwave balance. The strong seasonality in shortwave radiation drives a similar cycle in the net SEB, with the SEB being most negative during the winter months and typically slightly positive during the summer months.

1.1.3 - Observed Changes since 1950

Over the observational period, surface temperature trends over the interior of the ice sheet have warmed slightly, while the AP has warmed substantially in all seasons but most dramatically during the winter (*Turner et al., 2005; Steig et al., 2009; Muto et al., 2011*).

At Faraday/Vernadsky station on the peninsula, the mean annual temperature has increased at a rate of $0.56 \text{ }^{\circ}\text{C decade}^{-1}$ while winter temperatures have increased at $1.09 \text{ }^{\circ}\text{C decade}^{-1}$ (*Turner et al., 2005; Vaughan, 2006*). The sparse spatial coverage and large interannual variability of *in situ* measurements over the interior of the ice sheet make it difficult to establish statistically significant trends, especially since the trends are highly sensitive to the period of study (*Comiso, 2000; Monaghan et al., 2008*).

Monaghan et al. (2008) find statistically insignificant positive trends across most regions from 1960-2005, weakly negative trends from 1970-2005 and slightly positive trends again from 1992-2005. *Steig et al. (2009)*, using a spatially coherent interpolation based on automatic weather stations, found positive mean surface temperature trends from 1957-2006 across both the West ($0.17 \pm 0.06 \text{ }^{\circ}\text{C decade}^{-1}$) and East ($0.10 \pm 0.07 \text{ }^{\circ}\text{C decade}^{-1}$) Antarctic Ice Sheets, suggesting the region of warming has extended far beyond the peninsula. This is supported by *Vaughan et al. (2003)* who find that Siple Station, well to the south of the peninsula proper, has warmed by $1.1 \pm 0.55 \text{ }^{\circ}\text{C decade}^{-1}$.

The Southern Annular Mode (SAM) index describes the predominant pattern of atmospheric variability in the Southern Hemisphere and is manifested as a zonally symmetric shift in atmospheric mass between high and mid latitudes (*Kwok and Comiso, 2002; Marshall, 2003*). It is responsible for driving changes in the strength and location of the circumpolar vortex. The SAM index is measured by the difference in zonal mean sea level pressure (MSLP) at 40° and 65° S, with the positive polarity of the SAM index indicating a decrease in pressure over the Antarctic continent and increase in pressure at lower latitudes (*Gong and Wang, 1999; Marshall, 2003*). There has been a consistent trend towards the positive polarity of the SAM since the mid-1960s (Figure 1.2) and as such,

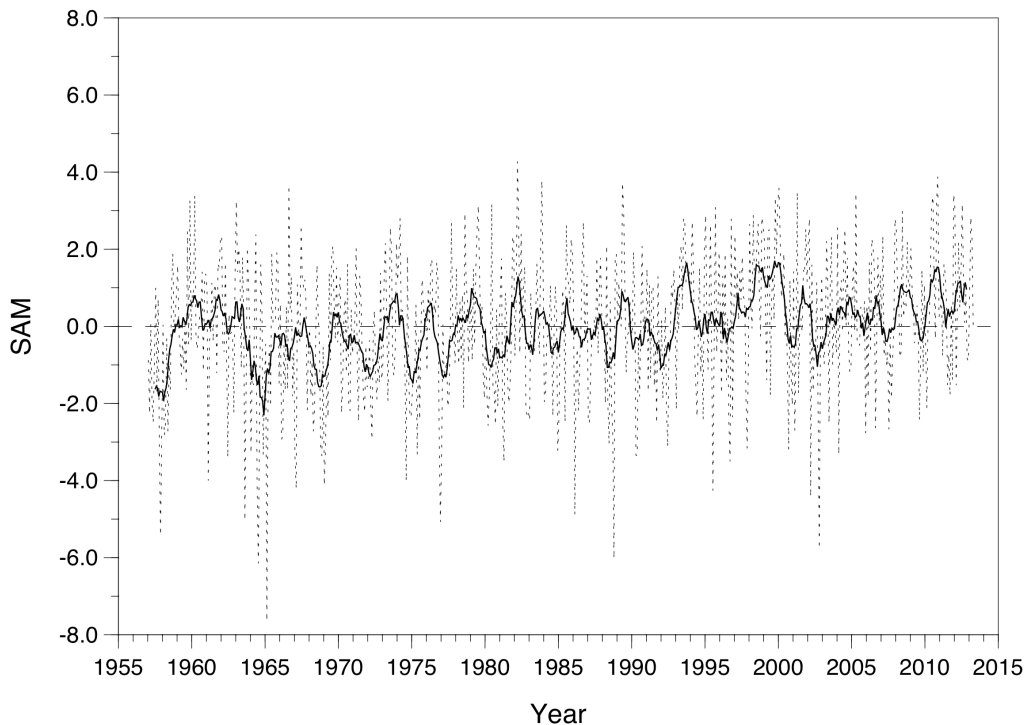


Figure 1.2. Monthly and 12 month running mean (dark) values of the Southern Annular Mode. From Marshall, 2003; updated from <http://www.nerc-bas.ac.uk/icd/gjma/sam.html>.

the focus of the following discussion is focused on the impacts associated with the observed positive polarity of the SAM index (*Marshall, 2003*).

Increased positive polarity of the SAM index enhances the strength of the circumpolar vortex (*Marshall, 2002*) by increasing the pressure difference between mid (increased MSLP) and high (decreased MSLP) latitudes (*van den Broeke and van Lipzig, 2004*).

The strengthened vortex drives significant cooling over most of East Antarctica, with substantial warming of the peninsula, due to the advection of warm, maritime air from higher latitudes (*Kwok and Comiso, 2002; van den Broeke and van Lipzig, 2004; Orr et al., 2004, 2008*). Increased air flow incident upon the peninsula has two results: i) low-level air circulation is blocked, leading to strong northerlies transporting warm air southwards along the western side of peninsula and ii) increased zonal wind velocities allow upper-level air masses to cross over the peninsula, driving both orographic precipitation on the windward side and warming on the lee side, due to the difference between the saturated and dry adiabatic lapse rates (i.e. föhn winds) (*Orr et al., 2004, 2008*).

An important aspect of the SAM reinforced atmospheric circulation pattern has been increased wind stress at the continental shelf edge, which has increased inflow of CDW onto the Amundsen-Bellinghousen Sea (ABS) continental shelf (*Thoma et al., 2008; Steig et al., 2012*). The high thermal forcing of CDW drives correspondingly high (i.e. greater than balance) basal melt rates of floating ice shelves, leading to high thinning rates (*Pritchard et al., 2012*). In particular, these rates are highest for those ice shelves

with a deep ice draft due to the predominance of CDW below 200 m and in the vicinity of deep troughs that route the CDW onto the shelf (*Bentley et al., 2009; Pritchard et al., 2012*). Oceanographic observations within the Pine Island Ice Shelf cavity confirm the presence of CDW and point to two important feedbacks: i) the thinning ice shelf, and growing cavity, allow more water flow and heat content into contact with the ice and ii) grounding line retreat on a retrograde slope exposes previously grounded ice to the ocean's heat and to water deeper in the water column, which in this case, also tends to be warmer (*Jenkins et al., 2010*).

The cause of the observed shift in the SAM index is uncertain, although numerous studies have pointed to increased stratospheric ozone depletion and subsequent stratospheric cooling as the primary cause with secondary reinforcement from increased concentrations of greenhouse gases (*Thompson and Solomon, 2002; Arblaster and Meehl, 2006*).

Although ozone recovery is expected to occur throughout the first half of the 21st century, increasing levels of greenhouse gases are expected to sustain and perhaps continue to drive the SAM index towards a more positive state (*Arblaster and Meehl, 2006*).

Increasingly, evidence suggests a strong tie between tropical Pacific sea surface temperature variability and the recent warming in West Antarctica, particularly during the austral winter and spring when the SAM trends are weakest (*Ding et al., 2011*).

Anomalous sea surface temperatures in the central tropical Pacific lead to an atmospheric Rossby wave pattern that subsequently modifies circulation patterns in the Amundsen Sea, leading to the delivery of warm air from lower latitudes towards this sector of

Antarctica (*Ding et al.*, 2011). It appears that decadal scale tropical climate variability has played an important climatic role in this region over the past two millennia (*Steig et al.*, 2013).

In stark contrast to the increasingly negative sea ice trends in the Arctic Ocean, sea ice extent has increased around Antarctica during the satellite record, although there are distinct, opposing spatial patterns (*Parkinson and Cavalieri*, 2012). Overall, sea ice extent has increased by $+17,100 \pm 2,300 \text{ km}^2 \text{ yr}^{-1}$ (or $1.5 \pm 0.4 \%$ decade⁻¹) between 1979-2010, with the largest gains occurring in the autumn and the smallest in the summer (*Parkinson and Cavalieri*, 2012). This overall trend masks competing regional patterns of $+13,700 \pm 1,500 \text{ km}^2 \text{ yr}^{-1}$ in the Ross Sea and $-8,200 \pm 1,200 \text{ km}^2 \text{ yr}^{-1}$ in the ABS sector (*Parkinson and Cavalieri*, 2012). Both of these changes are congruent with a deepening of the Amundsen Sea Low, which strengthens the southerly flow of cold air off the Ross Ice Shelf and brings warm, maritime air on northerly flow towards the western AP.

1.1.4 - Antarctic Peninsula

The Antarctic Peninsula extends for more than 1500 km from Ellsworth Land in the south to the tip of Trinity Peninsula, at nearly 63° S. The narrow mountainous spine of the peninsula extends, nearly contiguously, above 2000 m along its entire length, creating a barrier to atmospheric and oceanic circulation around the continent (*King and Turner*, 1997). This sector of Antarctica is dominated by two climatological low-pressure systems, one situated in the ABS sector and one in the Weddell Sea, which contributes to the significantly different climatic regimes on either side of the peninsula (*Morris and*

Vaughan, 2003). The ABS low advects warm, maritime air from lower latitudes to the western side of the peninsula, while the Weddell Sea low brings cold, dry air from the interior of the ice sheet to the eastern side of the peninsula. The result is a mean air temperature that is $\sim 2\text{-}5$ °C cooler on the eastern side (*Morris and Vaughan, 2003*). On a synoptic scale, the peninsula slows the eastward progress of low-pressure depressions in the circumpolar trough, which drives strong orographic precipitation on the western side of the peninsula, which can reach $1\text{-}2$ m w.eq. yr^{-1} at upper elevations (*Turner et al., 2005*). However, as this is the dominant source of moisture, a typical mountain ‘rain-shadow’ exists, resulting in a strong east-west gradient in precipitation. However, despite the lower precipitation on the eastern side, the cooler atmospheric temperatures result in a positive net surface mass balance even down to sea level. This likely contributed to the formation of the Larsen Ice Shelf as a whole and helps sustain Larsen C today.

Mean annual air temperatures on the AP have increased by 2 to 3 °C over the second half of the 20th century, a change much greater than the global average over this period and the cause of significant glaciological and ecological change (*Vaughan et al., 2001; King and Comiso, 2003; Vaughan et al., 2003; Turner et al., 2005*). The cause of observed warming appears to be the result of three primary mechanisms: i) increased northwesterly atmospheric flow transporting warm maritime air onto the peninsula, ii) increased ventilation of warm CDW onto the continental shelf, and iii) a regional sea ice-atmospheric feedback, where decreased ice extent has increased the sensible heat flux to the atmosphere (*Vaughan et al., 2001*). The spatial and temporal patterns of change on the peninsula show the fingerprint of each of these mechanisms individually at times,

however, the magnitude and spatial extent of the observed changes suggest a forcing that is likely the combination of and interaction between these mechanisms.

The increased mean zonal wind speed around the continent and the deepening of the ABS low are consistent with the increased positive polarity of the SAM index since the mid-1960s (*Marshall, 2002; Marshall et al., 2006*). Together, these changes have increased northwesterly flow along the west coast of the peninsula, bringing warm, maritime air into the region, and in certain cases, helping it breach the peninsula (*Orr et al., 2004, 2008*). At first glance this mechanism appears to be the most likely and while it is positively correlated with surface temperatures (*Kwok and Comiso, 2002*), there is a disparity in the seasonal forcing: SAM trends are strongest in the summer and autumn and the observed warming is greatest in the winter on the west coast of the AP (*Turner et al., 2005*). There is some evidence, however, based on the trends at Esperanza that atmospheric warming is greatest on the east coast during summer, suggesting that the föhn flow is significantly contributing to the observed warming there (*SCAR, 2009; Orr et al., 2008*). Recent evidence suggests that the warming on the peninsula may have begun in the 1930s and was almost certainly underway by the 1950s, well before changes in the SAM index were first observed (*Vaughan et al., 2001; Mulvaney et al., 2012*). This raises the question as to whether the forcings associated with the positive polarity of the SAM index have been the primary driver of the observed warming or whether they have operated in concert with an alternative mechanism over the past half-century, thus acting to amplify the response.

An additional cause of warming and environmental change on the AP is the increased ventilation of CDW on the continental shelf. Variability in the strength and location of the polar atmospheric vortex can drive changes in the ACC, which has shifted southward in recent decades, bringing warmer waters in closer proximity to the continental margin (*Gille, 2002; Jacobs, 2006*). *Meredith and King (2005)* demonstrate that the summer surface temperatures in the ABS have increased by more than 1 °C since 1950, while *Robertson et al. (2002)* show a warming of 0.3 °C of the Weddell Sea Deep Water since the 1970s, which they suggest could be the result of greater CDW entrainment in the Weddell Sea Gyre as the southern boundary of the ACC has shifted southwards. There is some evidence that the increased velocity of the westerlies (*Marshall, 2002*) may also have slightly strengthened the ACC, thus driving greater Ekman transport and inducing enhanced upwelling of warm CDW near the continental margin to balance the northward flow of surface waters. However, substantial uncertainty remains in the tie between the intensification of the westerlies and the strengthening of the ACC (*SCAR, 2009*).

Regardless of the exact mechanism, it is increasingly clear that changes in atmospheric circulation modulate the amount of CDW that upwells onto the continental shelf (*Thoma et al., 2008*) and that the intrusion of this water increases ice shelf basal melt rates (*Bindschadler et al., 2011a*) and reduces sea ice formation (*Turner et al., 2009*).

Trends in sea ice extent in the ABS and northwestern Weddell Sea stand in stark contrast to all other regions of Antarctica, as ice extent in these regions has decreased by more than 6% decade⁻¹ since the late 1970s (*Zwally et al., 2002a; Turner et al., 2009*). It is difficult to discern a causal relationship between sea ice extent and either atmospheric

and/or oceanic warming, since observations of changes in all parameters are nearly coincident. However, the feedback between reduced sea ice extent and increased oceanic / atmospheric temperatures is well established and has most certainly amplified the warming, particularly in the winter when sea ice trends are most strongly negative and the sensible heat difference between ocean and atmosphere is greatest (*Kwok and Comiso, 2002; Turner et al., 2009*).

As a whole, there is evidence that changes in atmospheric and oceanic circulation, in conjunction with a regional sea-ice feedback, have contributed to the observed warming of the AP (*Turner et al., 2005*). At this time, the relative roles and seasonality of each mechanism needs to be better constrained in order to make useful predictions of how the AP climatic regime will evolve over the next century, with important glaciological and ecological implications.

1.1.5 – Recent cooler conditions on the Northern Antarctic Peninsula

Published in *Bulletin in the American Meteorological Society*, **93**(7), S154-155.

Atmospheric warming over the Antarctic Peninsula (AP) during the second half of the twentieth century was remarkable, with local trends exceeding $0.5\text{ }^{\circ}\text{C decade}^{-1}$ (*Vaughan et al., 2003; Turner et al., 2005*). The complexity of atmospheric and oceanic circulation around the AP precludes clear attribution of this warming, although modified circulation patterns, largely driven by changes in latitudinal pressure gradients measured by the SAM index, likely played an important role (*Vaughan et al., 2001; Thompson and*

Soloman, 2002; Marshall, 2003, 2007; van den Broeke and van Lipzig, 2004). There has been increased advection of warm, maritime air towards the AP, coupled with increased upwelling of CDW onto the continental shelf of the ABS (*Orr et al., 2008; Jacobs et al., 2011; Martinson, 2011*). Dramatic reductions in sea ice extent (-6.6% decade⁻¹) in the ABS likely contributed to this warming as well, possibly as a driver and certainly as a positive feedback (*Meredith and King, 2005; Turner et al., 2009; Stammerjohn et al., 2012*).

This warming has had important glaciological impacts, including widespread glacier front retreat and acceleration along the western margin of the AP and the collapse of the Larsen A and B ice shelves on the eastern edge, the latter being unprecedented during the Holocene (Figure 1.1; *Pritchard and Vaughan, 2007; Scambos et al., 2003; Cook and Vaughan, 2010; Domack et al., 2005*). A key mechanism in the final collapse of these ice shelves has been the propagation of surface meltwater-filled crevasses through the entire ice thickness, rendering it into a series of narrow, elongated icebergs (*Scambos et al., 2003*). This process is dependent on having sufficient surface meltwater and thus, is directly tied to the intensity and duration of surface melting on the ice shelf.

Increased surface melting on the Larsen B Ice Shelf, just prior to its collapse, resulted from strong northeasterly and westerly winds, the latter associated with strong föhn flow over the Peninsula, bringing dry, adiabatically warmed air over the ice shelf (*van den Broeke, 2005*). The increased wind speed of the circumpolar westerlies associated with

the positive polarity of the SAM index has resulted in more air passing over rather than being blocked by the orography of the Peninsula (*Orr et al.*, 2004, 2008; *Marshall*, 2003).

In contrast to the strong warming trends observed during the previous half-century, between 2000 and 2011, AP stations have shown much greater variability, with many stations showing a slight cooling trend (Figure 1.3, Table 1.1). The mean annual temperature trend at Marambio station switched from a warming of $+0.65 \pm 0.47$ °C decade⁻¹ between 1971 and 2000 to a cooling of -1.57 ± 2.4 °C decade⁻¹ between 2000 and 2011. The cooling has been strongest at other northern AP stations (Bellingshausen, O'Higgins, Esperanza), with a cooling trend of about -0.7 °C decade⁻¹ over the last 15 years, following a tendency that started with the end of the 1998 El Niño. However, marked cooling is also evident on the Larsen C Ice Shelf, the largest remaining ice shelf on the AP, located on its eastern edge. This site has cooled by -1.11 ± 2.4 °C decade⁻¹ between 2000 and 2011, although interannual variability is large. It is important to note that none of the reported trends over the past decade are statistically significant, and cooling of a similar magnitude previously occurred over short time periods earlier in the record (Figure 1.3a). However, with the observed variability over the past decade, there is no longer a statistically significant ($p < 0.05$) warming trend for the northern AP over the past 30 years.

The observed warming from 1950-2000, in addition to the recent temperature variability, cannot solely be attributed to processes associated with the positive trend in the SAM index over this period (Figure 1.3b). These processes no doubt influence AP

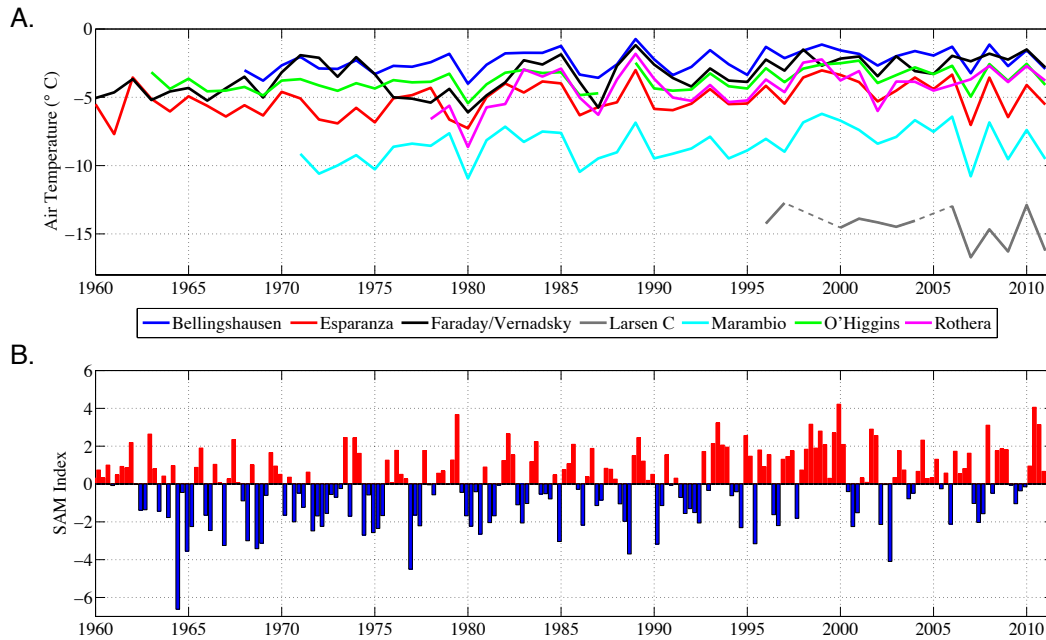


Figure 1.3. a) Mean annual air temperature records ($^{\circ}\text{C}$) for selected station on the Antarctic Peninsula. Dashed line for Larsen C indicates incomplete temperature record, precluding calculation of mean annual temperature. b) Seasonal SAM index calculated from station data (updated from Marshall, 2003).

climatology and likely contributed to summertime warming of the eastern side, through increased föhn flow over the peninsula (Marshall, 2003; Orr *et al.*, 2008). However, a significant portion of the regional warming, especially in winter, can be attributed to warming of the central tropical Pacific Ocean, and subsequent atmospheric Rossby wave trains directed towards West Antarctica (Ding *et al.*, 2011). This likely contributes to increased upwelling of CDW in the Amundsen Sea sector, driving high basal melt rates for glaciers in this region (Steig *et al.*, 2012). The strong negative anomaly in sea ice metrics for the ABS region also has a strong influence on the regional climate (Massom

et al., 2008; *Stammerjohn et al.*, 2012). However, the difficulty in untangling the attribution of this anomaly, whose forcings range from anomalous meridional winds driving earlier spring retreat (*Massam et al.*, 2008) to a positive feedback of increased shortwave absorption, further delaying fall sea ice advance (*Stammerjohn et al.*, 2012) and further perpetuating reduced ice duration, both highlights the complexity of the profound changes occurring on the AP and attests to the need for continued research to make accurate predictions for the future.

Station Name	Location (°S, °W)	Station Record	Mean Annual Temperature (°C)	Trends to 2000 (°C dec ⁻¹)	Trends 2000-2011 (°C dec ⁻¹)
Bellingshausen	-65.4, -64.4	1968-2011	-2.3 ± 0.8	+0.35 ± 0.28	-0.45 ± 1.3
Esparanza	-67.5, -68.1	1945-2011	-5.3 ± 1.3	+0.40 ± 0.19	-1.35 ± 2.2
Faraday/ Vernadsky	-62.2, -58.9	1950-2011	-3.7 ± 1.6	+0.59 ± 0.26	+0.37 ± 1.2
Larsen C	-66.9, -60.9	1995-2011	-14.4 ± 1.3	-	-1.11 ± 2.4
Marambio	-63.4, -57.0	1971-2011	-8.5 ± 1.3	+0.65 ± 0.47	-1.57 ± 2.4
O'Higgins	-63.3, -57.9	1963-2011	-3.7 ± 0.8	+0.23 ± 0.21	-0.71 ± 1.5
Rothera	-64.2, -56.7	1978-2011	-4.3 ± 1.4	+1.15 ± 0.94	+0.86 ± 1.6

Table 1.1. Mean annual air temperature and trends with 95% confidence intervals calculated by standard least-squares linear regression over specific time intervals.

1.2 - Ice Sheet Mass Balance

1.2.1 - Antarctic Mass Balance

The mass balance of an ice sheet is the net sum of all mass inputs to the ice sheet minus all mass losses from the ice sheet, which, for the case of Antarctica, is primarily the difference between the addition of mass from snowfall accumulation across the vast interior and loss at the ice sheet margin through both iceberg calving and basal melting. Unlike Greenland, surface meltwater production and subsequent runoff are a relatively minor component of the Antarctic mass balance budget. Three primary methods have been utilized to estimate the balance of these terms over the vast spatial scales of the ice sheets: i) flux balance based on ice discharge and accumulation (i.e. InSAR and SMB models), ii) gravitational measurements (i.e. GRACE) and iii) surface elevation monitoring (i.e. ICESat, CryoSat-2).

The mean rate of mass loss from Antarctica between 1992-2011 was $-71 \pm 53 \text{ Gt yr}^{-1}$, with an increase from $-48 \pm 65 \text{ Gt yr}^{-1}$ between 1992-2000 to $-87 \pm 43 \text{ Gt yr}^{-1}$ between 2000-2011 (Figure 1.4; *Shepherd et al.*, 2012). These mean rates are the sum of the individual changes from the AP, West Antarctic Ice Sheet (WAIS) and East Antarctic Ice Sheet (EAIS), which experienced rates of -20 ± 14 , $+14 \pm 43$ and $-53 \pm 65 \text{ Gt yr}^{-1}$ between 1992-2011, respectively (*Shepherd et al.*, 2012). These values are the reconciled estimates from the three methodologies previously mentioned.

As examples of results from these individual methods, *Rignot et al.* (2008) using the flux balance method, found that mass loss increased from $-112 \pm 91 \text{ Gt}$ in 1996 to $-196 \pm$

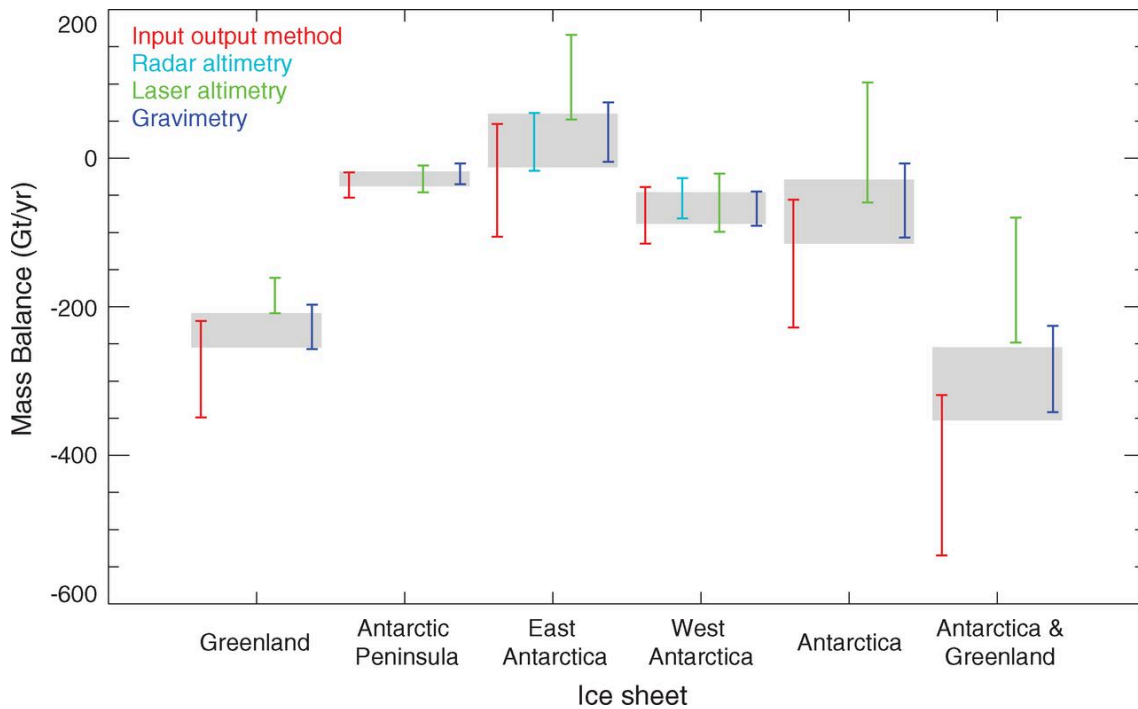


Figure 1.4. *Intercomparison of mass balance estimates derived from the four independent geodetic techniques over the period of 2003 to 2008. Also shown is the reconciled result (gray). From Shepherd et al., 2012.*

92 Gt in 2006, largely driven by the widespread losses along the ABS sector and along the Antarctic Peninsula. In particular, ice flow of the Pine Island Glacier (PIG) accelerated by 34% between 1996-2006, while the Smith increased by 75%, the Pope by 20% and the Haynes by 27%, yielding a total loss of $-90 \pm 27 \text{ Gt yr}^{-1}$ in 2006 for this sector alone (Rignot et al., 2008). Coincident to these accelerations was a dynamic thinning of 6 m yr^{-1} for PIG, 9 m yr^{-1} at Smith and 4 m yr^{-1} at Thwaites between 2003-07 (Pritchard et al., 2009). GRACE results show comparable continental-wide estimates of $-190 \pm 77 \text{ Gt yr}^{-1}$ from 2002-2009, of which $-132 \pm 26 \text{ Gt yr}^{-1}$ was lost from WAIS and, in contrast to the previous methodology, $-57 \pm 52 \text{ Gt yr}^{-1}$ from EAIS (Chen et al., 2009). Velicogna (2009) suggest that Antarctic mass loss is accelerating, increasing from -104

Gt yr⁻¹ between 2002-2006 to -246 Gt yr⁻¹ between 2006-2009, a 140% increase in mass loss between these periods. However, the GRACE methodology is sensitive to how changes in isostatic rebound are incorporated, since modest changes of dense mantle rocks can introduce large uncertainty in the gravity fields and *in situ* observations of these changes are poorly constrained (*Velicogna, 2009*). Measurements of surface elevation change from repeat altimetry can be converted to estimates of mass change through density assumptions and corrections for thinning due to firn compaction, although this correction is sensitive to variations in temperature and accumulation (*Zwally et al., 2005*). *Zwally et al. (2005)* find that the WAIS is losing -47 ± 4 Gt yr⁻¹, while the EAIS shows a slight gain of $+16 \pm 11$ Gt yr⁻¹ between 1992-2001. However, due to the configuration of past satellite altimeters, the highest uncertainty existed in regions with steep surface slopes, which typically coincides with the regions of greatest change along the margins of the ice sheets. Next generation altimeters (i.e. CryoSat-2, ICESat-2) promise to bring improved resolution/accuracy in these regions through modified configurations.

1.2.2 - Antarctic Peninsula Mass Balance

In contrast to the Antarctic-wide ice sheet mass balance, meltwater production and surface runoff are important components of the mass balance of the AP, primarily due to its warmer, maritime influenced climate and relatively low elevation (one third of its area is below 200 m asl; *Vaughan, 2006; Pritchard and Vaughan, 2007*). Further, the observed atmospheric warming is particularly important on the AP because summer temperatures are close to the melting point and thus, even a small increase can cross this threshold, resulting in large non-linear changes in both melt season duration and intensity

(*Fahnestock et al.*, 2002; *Vaughn*, 2006). *Vaughan* (2006) demonstrated a significant rise in positive degree-days (PDD) along the peninsula from 1950 to 2003, with rates ranging from 1.4 ± 0.7 PDD yr^{-1} at Faraday/Vernadsky, 1.8 ± 1.7 PDD yr^{-1} at Rothera and 2.7 ± 1.3 PDD yr^{-1} at Bellingshausen. Below average summer temperatures over the most recent seven years have reduced the rate, and the significance, of these trends (*Barrand et al.*, 2013). The updated trends through 2010 are 1.38 ± 0.54 PDD yr^{-1} at Faraday/Vernadsky, 0.95 ± 1.27 PDD yr^{-1} at Rothera and 1.9 ± 1.10 PDD yr^{-1} at Bellingshausen. This change over the past decade highlights the climate variability of this region that was discussed in Section 1.1.5.

While the increase in surface temperatures and subsequent meltwater runoff over the past half-century are significant, the acceleration of outlet glaciers has likely had a larger impact on the overall mass balance of the AP (*Rignot et al.*, 2004; *Pritchard and Vaughan*, 2007). Over 80% of the nearly 400 steep mountain glaciers flowing west off the spine of the peninsula have accelerated and retreated substantially, largely driven by reduced back stress at the tidewater terminus rather than by increased basal sliding associated with an inefficient basal hydrologic system (*Cook et al.*, 2005; *Pritchard and Vaughan*, 2007). Thinning at the tidewater terminus reduces the effective stress at the bed, allowing faster flow and leading to longitudinal thinning until the tongue becomes buoyant, at which point, calving is largely controlled by the slope and depth of the fjord (*Pritchard and Vaughan*, 2007). These changes have significantly contributed to the estimated mass loss of between -28.6 and -32 ± 6 Gt yr^{-1} since 2002 (*Ivins et al.*, 2011; *Chen et al.*, 2009).

The dynamic response of the outlet glaciers following the collapse of floating ice shelves has been an important component of the observed mass loss on the AP. Following the breakup of the Larsen B Ice Shelf, the outlet glaciers responded to the new force balance by accelerating two to six times their background velocity, while subsequently thinning by 20-40 m yr⁻¹ near the calving front (*Scambos et al.*, 2004; *Berthier et al.*, 2012). Thinning has propagated inland over the past decade, sustaining the total mass imbalance at rates of ~8.9 Gt yr⁻¹ (*Berthier et al.*, 2012).

1.3 - Ice Shelves: Processes and Properties

Ice shelves are typically composed of deep inflows of meteoric ice from ice streams or outlet glaciers bounded by bands of relatively thin ice downstream of promontories, which is typically composed of a mélange of marine ice, sea ice and *in situ* snowfall (*Glasser et al.*, 2009). Ice shelves can also form when snowfall accumulates on sea ice, as is the case for parts of the Wilkins Ice Shelf, though this is less frequently observed. Regardless of their formation mechanism, ice shelves typically appear flat and featureless, thus masking their heterogeneous composition. Ice shelves also form the interface between the atmosphere and ocean, thus their characteristics and processes are uniquely different from those of grounded ice. Understanding ice shelf structure and processes is fundamental to future predictions of sea level rise as nearly 75% of the ice flux from the Antarctic Ice Sheet passes through these gates (*Bindschadler et al.*, 2011b).

Most ice shelves consist of four mechanically distinct ice types: i) cold and stiff meteoric ice flowing off the surrounding landscape, ii) derivations of this meteoric ice with

previously or currently modified temperature, density or ice fabrics, which tends to make it softer, iii) marine ice formed from refrozen meltwater or sea water saturated firn and iv) locally accumulated snow and firn (*Glasser et al.*, 2009). One of the most important features of ice shelves, especially those composed of numerous inflows, is the suture zone contact between neighboring meteoric inflows (*Glasser et al.*, 2009; *Holland et al.*, 2009). Plumes of cold seawater freshened by basal melt rise and supercool due to reduced pressure at shallow depths, leading to the formation of frazil ice crystals. These crystals subsequently accrete in ice draft minima, typically found downstream of promontories or ice rises (*Robin*, 1979; *Holland et al.*, 2009). Marine ice initially has a temperature close to the freezing point, which results in a lower viscosity than the colder meteoric ice that comprise the major inflows to the ice shelf. This likely contributes to its ability to deform viscously without fracturing (*van der Veen*, 1998a; *Larour et al.*, 2004; *Holland et al.*, 2009). The importance of this can be seen in the consistent termination of rifts at the lateral edges of suture zones (*Rignot and MacAyeal*, 1998; *Fahnestock et al.*, 2000; *Larour et al.*, 2004; *Bassis et al.*, 2007; *Glasser et al.*, 2009; *Hulbe et al.*, 2010; *Jansen et al.*, 2010). A good example are the numerous large rifts located downstream of the Kenyon Peninsula in the southeastern sector of Larsen C that propagate perpendicular to ice flow but all coherently terminate at the edge of a smoothed flow band (Figure 1.1; *Glasser et al.*, 2009). Over the past fifteen years of satellite observations the length of the rifts has not changed, suggesting that this suture zone, which likely contains marine ice, is responsible for rift termination (*Glasser et al.*, 2009; *Holland et al.*, 2009). Future changes in either ocean circulation or temperature that increase the incursion of warm

water beneath the Larsen C Ice Shelf could reduce basal marine ice accretion and its stabilizing influence (*Holland et al.*, 2009).

The primary source for the accreted marine ice is meltwater produced through basal melt at the grounding line of deep outlet glaciers. Here, the oceanic thermal forcing is greatest due to the depression of the melting point of ice at elevated pressures and often times, the presence of warm, CDW at these depths, particularly in the ABS sector of Antarctica (*Rignot and Jacobs*, 2002; *Pritchard et al.*, 2012). Net basal melting beneath all floating ice shelves in Antarctica is estimated at 40 cm yr^{-1} (*Rignot and Jacobs*, 2002). However, this value masks spatial variability on both the individual ice shelf scale, which can reach up to 40 m yr^{-1} at deep grounding lines, and at the continental scale, largely related to the distribution of CDW (*Rignot and Jacobs*, 2002; *Pritchard et al.*, 2012). As a whole, thick ice shelves along the ABS coastline experience the highest basal melt rates although, between 2003-2009, these shelves were also observed to thin substantially (up to 6.8 m yr^{-1}), likely due to increased basal melt (*Pritchard et al.*, 2012). Increased basal melt is likely tied to the enhanced flux of warm CDW into the cavities beneath these ice shelves, related to the previously discussed intensification of the atmospheric westerlies and poleward shift of the ACC (*Pritchard et al.*, 2012). Recent observations of large and rapid change emphasize the importance in understanding the atmospheric and ocean circulation patterns that transport this water into contact with the ice (*Thoma et al.*, 2008; *Pritchard et al.*, 2012).

Three ice shelves have significantly retreated and four have completely disintegrated on the AP, yielding a total loss of over 28,000 km² of floating ice over the past five decades (*Cook and Vaughan, 2010*). The subsequent acceleration of the outlet glaciers that previously fed these ice shelves has increased ice discharge to the ocean, a process that has been sustained for decades (*Rignot et al., 2004; Scambos et al., 2004; Pritchard et al., 2009; Berthier et al., 2012*). Our current understanding of ice shelf retreat and collapse is based primarily on observations, and at this time, there is no broad theory that is applicable in all cases. This gap in predictive capability is primarily due to the uniqueness of individual ice shelves, a uniqueness that exists in composition, geometry, stress fields and environmental forcings.

Despite this variety, certain patterns have emerged that capture the features and processes that influence ice shelf stability, and ultimately, may lead to ice shelf collapse. Prior to collapse, nearly all ice shelves undergo a period of pre-conditioning consisting of i) thinning, either from a surface atmospheric forcing, leading to a decreased surface mass balance and/or firn densification, or a basal oceanic forcing, in which warm ocean waters erode the ice shelf from beneath (*Fricke and Padman, 2012; Pritchard et al., 2012*), ii) frontal retreat, which may eliminate the ‘compressive arch’ (*Doake et al., 1998*), iii) increased ice velocity or lateral velocity variations (*Vieli et al., 2007*) and iv) increased fracture/rifting (*Glasser and Scambos, 2008; MacGregor et al., 2012*). These processes are often inter-connected: thinning can reduce lateral shear stresses and/or weaken connections between the ice and pinning points near the ice front, driving an increase in surface velocities and extensional strain and subsequently increasing rifting. This

evolution was observed in the two decades leading up to the breakup of Larsen B (*Glasser and Scambos, 2008*). An additional key process, driven by regional atmospheric warming and the resulting increase in positive degree-days across the peninsula, has been the increased production of surface meltwater and subsequent firn densification and meltwater ponding (*van den Broeke, 2005; Vaughan, 2006*). Most catastrophic breakups have occurred during or just following a melt season of increased intensity and duration, as evidenced by extensive meltwater ponding on the shelf surface, which suggests that this is key to the final disintegration (*Scambos et al., 2000, 2003; van den Broeke, 2005*). The mechanism by which surface meltwater leads to collapse is as follows: meltwater can drain into surface crevasses, which, if they fill to ~90% of their volume will continue to propagate downwards, as the stress intensity at the crevasse tip exceeds the fracture toughness of the ice (*Weertman, 1973; Scambos et al., 2000, 2003; van der Veen, 2007*). Fractures that propagate through the entire ice thickness render the ice shelf into a series of narrow, unstable blocks, which, if disturbed, will begin to topple, releasing their potential energy in a manner that can cause mass disintegration (*MacAyeal et al., 2003; Guttenberg et al., 2011*).

A notable anomaly to the mechanism described above is the George IV Ice Shelf, connecting Alexander Island with the peninsula on the west coast, which has survived for decades with widespread seasonal surface meltwater ponding (*Cook and Vaughan, 2010*). A key difference, however, is that George IV is in uniaxial compression, which precludes the development or persistence of surface crevasses and subsequently results in meltwater abandonment on the surface where it is unable to drive hydrofracture (*Cook and Vaughan,*

2010). An additional anomaly was the breakup of the Wilkins Ice Shelf on the west coast of Alexander Island, which occurred during the autumn/winter when no surface meltwater was present. However, it is believed that full-thickness rifts had developed during previous melt seasons through the hydrofracture mechanism, yet the shelf had remained intact (*Scambos et al.*, 2009). The final breakup was, at least partially, induced by bending stresses at the ice front, resulting in a series of calving events that released narrow, elongated blocks parallel to the ice front (*Scambos et al.*, 2009).

The observed retreat and disintegration of ice shelves has closely followed the $-9\text{ }^{\circ}\text{C}$ mean annual isotherm, leading *Vaughan and Doake* (1996) to suggest that this might represent the ‘limit of viability’ for ice shelves. This simple concept has been surprisingly accurate in predicting the timing of each ice shelf collapse, although, it has become clear that while atmospheric warming is undoubtedly important, it is only one of many processes that have a significant influence on the stability of ice shelves. Increasingly, the role of ice shelf structure, basal processes, ice front geometry and changes to the stress field are being recognized for helping control the ‘limit of viability’ for ice shelves.

1.4 - Thesis Impetus

Atmospheric warming of $\sim 2.5\text{ }^{\circ}\text{C}$ over the last half-century (*Turner et al.*, 2005) and concurrent environmental changes, including a dramatic decline in sea ice extent, widespread tidewater glacier retreat, and acceleration and the disintegration of numerous ice shelves totaling over $28,000\text{ km}^2$ has made the AP one of the fastest changing locations on the planet (*Parkinson and Cavalieri*, 2012; *Pritchard and Vaughan*, 2007;

Cook and Vaughan, 2010). The subsequent and sustained acceleration and dynamical thinning of the outlet glaciers following the collapse of ice shelves has increased the AP's contribution to observed sea level rise (*Scambos et al., 2004; Pritchard et al., 2011; Berthier et al., 2012*). As nearly 75% of the ice flux from the Antarctic Ice Sheet occurs through ice shelves ringing the continent, these observations amplify the importance of understanding ice shelf stability in order to make meaningful predictions of future sea level rise (*Bindschadler et al., 2011b*).

This thesis seeks to contribute to the understanding of ice shelf stability by investigating two key structural components of ice shelves, namely basal crevasses and suture zones. These features are ubiquitous on ice shelves around Antarctica, and likely affect, both as a hindrance to and reinforcement of, the stability of ice shelves in a warming climate. An improved understanding of ice shelf structure, and the interaction between structure and climate, will lead to a more predictive framework for understanding ice shelf stability, and subsequently, future sea level rise.

Chapter 2

Basal crevasses and associated surface crevassing on the Larsen C Ice Shelf,

Antarctica and their role in ice shelf instability

Published in the *Annals of Glaciology*, 58(60), 10-18, doi: 10.3189/2012AoG60A005, 2012.

Abstract

We identify a series of basal crevasses along a 31 km transect across the northern sector of the Larsen C Ice Shelf using *in situ* ground penetrating radar. The basal crevasses propagate from a region of multiple, shallow basal fractures to form widely spaced (0.5 to 2.0 km) but deeply incised (70 to 134 m) features. Surface troughs, observed in visible imagery, exist above the basal crevasses as the ice vertically shears to reach hydrostatic equilibrium, while widespread surface crevassing occurs along the crests and on the flanks of the undulations, primarily aligned with the topography. We suggest, based on the location of the surface crevasses and the along-flow evolution of the basal crevasses, that the former are induced by a bending stress created by gradients in hydrostatic forces. Using a linear elastic fracture mechanics model, we investigate the sensitivity of basal crevasse propagation to observed trends of ice shelf thinning and acceleration. Basal crevasses are large-scale structural weaknesses that can both control meltwater ponding and can induce surface crevassing. Together, these features may represent an important mechanism in both past and future ice shelf disintegration events on the Antarctic Peninsula.

2.1 - Introduction

Over 28,000 km² of floating ice shelves have disintegrated along the Antarctic Peninsula (AP) over the past three decades, punctuated by the catastrophic breakup of Larsen A in 1995 and Larsen B in 2002 (*Cook and Vaughan, 2010*). The final collapse of these ice shelves appears to be directly tied to increased meltwater production and surface crevasse hydrofracture, rendering the ice shelf into a series of unstable narrow blocks, capable of rapid disintegration (*Scambos et al., 2000, 2003; MacAyeal et al., 2003*). However, the rapid collapse masks the slow pre-conditioning of the shelves in the preceding years, processes that make them increasingly susceptible to this style of collapse. The pre-conditioning has been primarily driven by a 2.5 °C atmospheric warming along the AP since 1950, which has, at least partially, been driven by changes in the Southern Annular Mode index. The result has been increased advection of warm, maritime air from lower latitudes towards the AP (*Vaughan et al., 2003; Orr et al., 2004*). Strengthening of the westerly winds increases the passage of this air mass over the peninsula, where it is further warmed by the föhn effect and certainly contributed to the increased surface melt on Larsen B prior to its breakup (*Orr et al., 2004; van den Broeke, 2005; Orr et al., 2008*). Increased surface melt has driven firn densification and the formation of ice layers, eventually allowing melt ponds to be supported on the shelf surface (*Scambos et al., 2000, 2003; Fahnestock et al., 2002; van den Broeke, 2005; Vaughan, 2006; Holland et al., 2011*).

Increased basal melting has been shown to be a key pre-conditioning process for ice shelf disintegration as well, primarily by thinning the ice shelf and subsequently reducing the

resistive stresses at lateral shear margins and ice rises (*Glasser and Scambos, 2008*). However, unlike the Amundsen-Bellingshausen Sea sector, where the incursion of warm, Circumpolar Deep Water onto the continental shelf has been well documented and has been shown to drive the high basal melt rates beneath Pine Island Glacier, the ice shelves in the Weddell Sea sector are protected from this water mass (*Jacobs et al., 2011*). Weddell Deep Water has shown substantial decadal variability in temperature and salinity properties, yet no sustained long-term trends have been observed (*Robertson et al., 2002; Fahrbach et al., 2004*). Basal melting (and refreezing) is still believed to substantially modify the ice shelves in the Weddell Sea sector, although limited oceanographic measurements prevent a complete understanding of the extent and magnitude of these processes (*Shepherd et al., 2003; Nicholls et al., 2004; Glasser and Scambos, 2008; Holland et al., 2009; Khazendar et al., 2011*).

Crevasse hydrofracture, the process by which water filled surface crevasses propagate downwards, possibly through the entire ice thickness, has been shown to be a key mechanism in polar glaciology (*Weertman, 1973; van der Veen, 1998b; Zwally et al., 2002b; Das et al., 2008*). On ice shelves, surface crevasses often form near the ice shelf grounding line, along shear margins, or at the ice shelf front due to bending stresses (*Scambos et al., 2003; Scambos et al., 2009*). Crevasses formed in upstream areas are commonly advected into the floating portion of the ice shelf as well. The filling of surface crevasses with meltwater increases the stress intensity at the crevasse tip, which, if it exceeds the fracture toughness of ice, allows the crevasse to propagate further downwards (*van der Veen, 1998b*). Continued crevasse propagation is dependent on

having sufficient meltwater volume to maintain a high level in the crevasse as it propagates downward. Thus, the ability of an ice shelf to support surface melt ponds is one harbinger of collapse (*Scambos et al.*, 2003), although low confining stress (longitudinal or transverse) is also necessary, in order to permit crevasse deepening by hydrofracture (*Cook and Vaughan*, 2010).

While the role of surface crevasse propagation has received significant attention, the role of basal crevasses, which form at the shelf bottom and extend upwards into the ice, has received less attention. Airborne radar surveys have identified large hyperbolic radar returns, interpreted as basal crevasses, within the Ross (*Jezek et al.*, 1979), Larsen (*Swithinbank*, 1977), and the Riiser-Larsenisen ice shelves (*Orheim*, 1982). *Weertman* (1973, 1980) suggested that the height of a single basal crevasse, h , on a free-floating ice shelf of thickness H is:

$$h = \frac{\pi H}{4}$$

Equation 2.1

Both surface and basal crevasses are rarely found individually, and the presence of multiple crevasses in close proximity reduces the overall stress field. This likely limits the penetration height to one-half the ice thickness (*Weertman*, 1980). Still, field measurements of basal crevasse heights were found to be significantly smaller than predicted by Eq. (2.1). *Jezek* (1984) hypothesized that the embayed walls and ice rises constraining the ice shelf resulted in a compressive back stress that resisted both ice flow and crevasse propagation. *Rist* (1996), *Rist et al.* (1996, 2002) and *van der Veen* (1998a) extended the theoretical analysis of basal crevasse propagation by utilizing a linear elastic fracture mechanics (LEFM) approach. By integrating the stresses along the length of the

crevasse, they calculate the stress intensity factor at the crevasse tip (K_I), which is compared to a critical value, K_{IC} , the fracture toughness of the ice, to determine the height to which a crevasse will propagate (*Rist et al.*, 2002).

We present *in situ* ground based radar observations of basal crevasses along a 31 km transect across the northern section of the Larsen C Ice Shelf, Antarctica. We describe the basal crevasse properties and how they evolve as they are advected towards the calving front. We present high-resolution satellite imagery detailing the development of surface crevassing primarily aligned with the crests of the surface undulations. We model the theoretical penetration height of a basal crevasse at its point of formation, based on the LEFM model of *van der Veen* (1998a) and investigate the sensitivity of penetration height to observed changes. We conclude with a discussion of the possible contribution of these features to ice shelf instability in light of observations of change in this sector of the Larsen C Ice Shelf.

2.2 - Study Site

Larsen C is the largest remaining ice shelf on the AP, consisting of over 50,000 km² of floating ice, which is fed from 12 major outlet glaciers flowing off the mountainous spine of the AP (Figure 2.1a; *Cook and Vaughan*, 2010; *Glasser et al.*, 2009). The ice shelf thickness exceeds 700 m at the grounding line but thins to 150 m at the ice front, with a typical range of 250-400 m. Along the 31 km radar transect, ice thickness decreases from 300 to 280 m towards the calving front of the ice shelf (*Griggs and Bamber*, 2009).

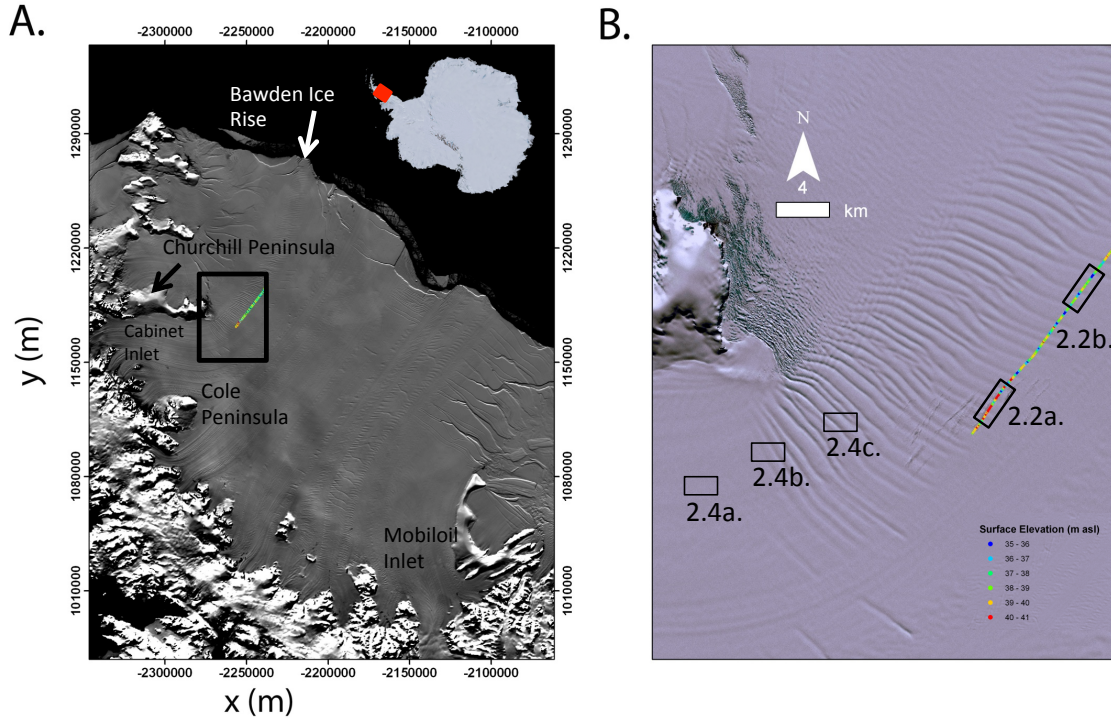


Figure 2.1. a) Subsection of MODIS MOA mosaic detailing the Larsen C Ice Shelf with prominent geographic features labeled (Haran et al., 2005). Radar transect is shown as colored line corresponding to surface elevations from kinematic GPS. Black box indicates location of Figure 2.1b. Inset: Location of MODIS image on the Antarctic Peninsula. Coordinates are polar stereographic (at 71° S secant plane, 0° meridian, WGS84 ellipsoid) where x is easting and y is northing. b) Landsat Image Mosaic of Antarctica (LIMA) image of the edge of Churchill Peninsula with the surface undulations visible. Black boxes indicate location of radar profiles shown in Figure 2.2 and high-resolution imagery shown in Figure 2.4.

Larsen C displays the characteristic velocity field of an embayed ice shelf, in which velocities increase with distance from the grounding line, reaching a maximum in the

middle of the calving front, furthest from resistive stresses (*Khazendar et al.*, 2011). Along this transect, ice velocity increases from 328 to 355 m a⁻¹ (*Khazendar et al.*, 2011).

The extent and geometry of Larsen C has been largely stable over the last five decades, although it has been observed to be both thinning and accelerating over the past two decades (*Shepherd et al.*, 2003; *Cook and Vaughan*, 2010; *Khazendar et al.*, 2011). Radar altimetry between 1992-2001 found that the Larsen C surface elevation has lowered, on average by -0.08 m a⁻¹, although one northerly location decreased by -0.27 m a⁻¹, which has been partially attributed to increased basal melting (*Shepherd et al.*, 2003). Limited oceanographic measurements suggest low basal melt rates beneath the ice shelf, with little evidence that unaltered Weddell Deep Water reaches the cavity (*Nicholls et al.*, 2004; *Holland et al.*, 2009). More recently, it has been suggested that the surface lowering observed by *Shepherd et al.* (2003) may be largely attributed to atmospheric driven firn densification (*Holland et al.*, 2011). *Khazendar et al.* (2011) found that the northern sector of the ice shelf accelerated by 80 m a⁻¹ or 15% between 2000 and 2006 and a further 6-8% between 2006-2008 in Cabinet Inlet, possibly due to a reduction in back stress from the Bawden Ice Rise and / or the erosion of marine ice formerly suturing neighboring flow bands together.

2.3 - Methods

2.3.1 - Data Acquisition and Processing

Radar surveys were conducted with a Mala Geosciences ground based pulse radar system (CU-II control unit) with a 25 MHz (~6.8 m wavelength in ice) antenna pulled behind a

snowmobile traveling at an average of 4.5 m s^{-1} . We recorded at 1024 16-bit samples per trace and each trace lasted $\sim 4000 \text{ ns}$. A 16-fold stack was applied during recording. To improve the signal to noise ratio of the radar data the mean waveform was removed from all profiles and a de-wow filter was applied to remove DC bias and low frequency drift. The measured two-way travel time was converted to depth assuming a mean radar velocity of 0.173 m ns^{-1} , which incorporates a linear decrease from 0.190 m ns^{-1} at the surface (in the firn) to 0.168 m ns^{-1} at the depth of the firn-ice transition. This depth was determined from the RACMO2 regional climate model (M. van den Broeke, pers. comm., 2011). Radargrams are presented as un-migrated to emphasize the reflection hyperbolas within the ice column.

Kinematic GPS data were collected simultaneously using a Trimble GeoXT unit mounted to the radar sledge with a $\pm 1.03 \text{ m}$ horizontal precision and $\pm 1.86 \text{ m}$ vertical precision. Position data were collected relative to the World Geodetic System 1984 (WGS84) ellipsoid and were corrected to heights above mean sea level (msl) using the EIGEN-GL04C geoid, which combines GRACE satellite data and surface gravity data from altimetry and gravimetry (Forste *et al.*, 2008). Surface elevations (Figure 2.2b) were then corrected for variations in the tidal amplitude ($\pm 1 \text{ m}$) using the Circum-Antarctic Tidal Simulation version 2008a (CATS2008a), updated from Padman *et al.* (2002).

The ice shelf-ocean interface reflection was manually delineated along each profile by following the maximum amplitude in the radar waveform near the approximate interface. This was only done where the interface reflection was strong and easily determined. The

ice thickness, H , was then calculated by taking the difference between the surface height, z , and the identified ice-ocean interface.

2.3.2 - Basal Crevasse Propagation Model

Based on a linear elastic fracture mechanics approach, an individual basal crevasse should penetrate to a given height where the stress concentration near the crevasse tip equals the fracture toughness of the ice, K_{IC} (*Rist*, 1996; *Rist et al.*, 1996; *van der Veen*, 1998a). The stress intensity factor, K_I , is estimated by integrating the stress along the length of the fracture, while the fracture toughness of non-porous ice, measured by *Rist et al.* (2002) on an ice core from the Ronne Ice Shelf, is $0.155 \text{ MPa m}^{1/2}$. There is some historical evidence that in the presence of salt water, the fracture toughness may be reduced by a factor of up to 3 (*Johnston and Parker*, 1957).

According to *van der Veen* (1998a), the stress intensity factor at the crevasse tip may be described as:

$$K_I = \int_0^h \frac{2\sigma_n(z)}{\sqrt{\pi h}} * G(\gamma, \lambda) dz \quad \text{Equation 2.2}$$

where h is the crevasse height, σ_n is the net longitudinal stress, H is the ice thickness, z is the height within the ice column ($z=0$ at base) and G is a function of $\lambda=h/H$ and $\gamma=z/h$.

The net longitudinal stress, σ_n , is the integral of the lithostatic stress, acting to close the crevasse, whereas seawater pressure in the basal crevasse and the tensile spreading stress, R_{xx} , act to further open the crevasse (*van der Veen*, 1998a). We extract longitudinal strain rates from InSAR derived surface velocities along the transect (*Khazendar et al.*, 2011; *E. Rignot*, pers. comm., 2011). The tensile spreading stress is related to the stretching rate

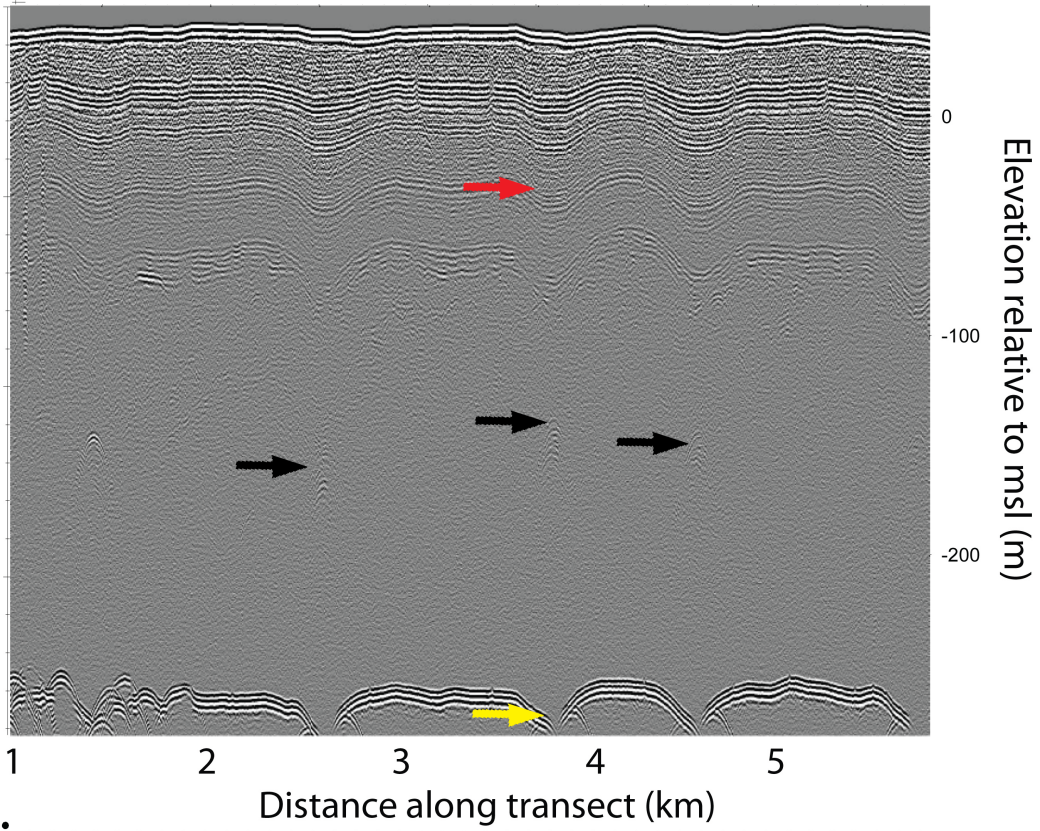
through the flow rate factor, B , which has a strong dependence on temperature (*van der Veen and Whillans, 1989*). We calculate a parabolic temperature profile within the ice column assuming basal melting, with the surface constrained by *in situ* automatic weather station mean annual temperature ($-12\text{ }^{\circ}\text{C}$) and an assumed basal temperature at the approximate freezing point of sea water ($-2\text{ }^{\circ}\text{C}$; *Sandhäger et al., 2005*). Given the observed geometry of the basal crevasses (i.e. spacing \gg height), we model the basal crevasses as individual features. For a more complete discussion of this model see *van der Veen (1998a, 1998b)*.

2.4 - Results

2.4.1 - Radar Survey

Twenty-seven basal crevasses, with an average spacing of 1.2 km, are identified along a 31 km transect aligned with the flow direction of the ice shelf downstream of Cabinet Inlet. Basal crevasses are identified by strong hyperbolic reflections within the ice column (Figure 2.2; black arrows) and two, nearly symmetric hyperbolas at the bottom corners of the crevasse (Figure 2.2; yellow arrows). The underside of the ice shelf is highly fractured in the initial 2 km of the transect, however, a smooth basal surface exists along the remainder of the transect (Figure 2.2). Crevasse spacing ranges from 0.5 to 2.0 km and does not systematically vary along the length of the transect. Penetration height of the basal crevasses is greatest near the origin, where they extend 120-134 m into the ice column (Figure 2.3). Height subsequently decreases along the length of the profile, decreasing by ~ 40 m in the first 15 km while remaining nearly constant over the remaining ~ 15 km (Figure 2.3). In addition to a decrease in absolute height, the relative

A.



B.

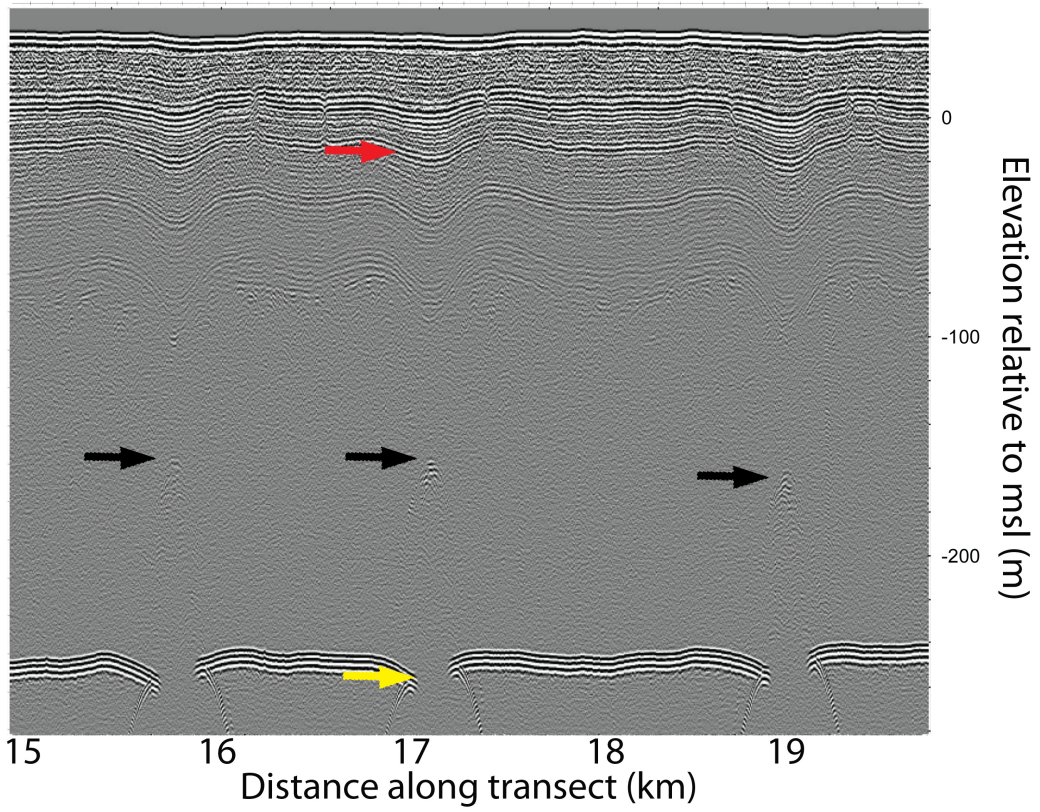


Figure 2.2. *25 MHz radar profiles from two sections of the 31 km transect. a) Basal crevasses (black arrows) emerge from a region of highly fractured basal ice. Hyperbolas from the bottom corners overlap (yellow arrow) preventing crevasse width from being known in this section. Firn layers slump above the basal crevasses in response to hydrostatic equilibrium (red arrow). b) Arrows the same as A. Both absolute crevasse height and height as a percentage of ice thickness are smaller in this section of the profile.*

penetration height (as a function of ice thickness) also decreases from ~40% to 25%. Initially, the bottom width of the basal crevasses is quite narrow (20-70 m) and at times, difficult to determine due to the overlap of the two hyperbolas that originate from the bottom corners of the crevasse (Figure 2.2a, yellow arrow). The opening width of the basal crevasses increases along the length of the transect, opening ~100 m in the first 15 km, while ranging between 150-240 m over the remaining ~15 km (Figure 2.3; black line). The surface undulations have an amplitude of 3-4 m, although the amplitude of these features are likely much larger proximal to Churchill Peninsula, as the radar transect was conducted near the edge of the features. Internal layering within the firn shows significant downwarping of 11-18 m above the basal crevasses, with deeper layers showing greater downwarping (Figure 2.2, red arrows).

2.4.2 - Satellite Imagery

Surface undulations on the ice shelf are easily identified in both MODerate-Resolution Imaging Spectroradiometer (MODIS; 250 m) and Landsat (15 m) imagery as a series of parallel alternating dark and light bands (Figure 2.1). In total, 102 undulations, with the

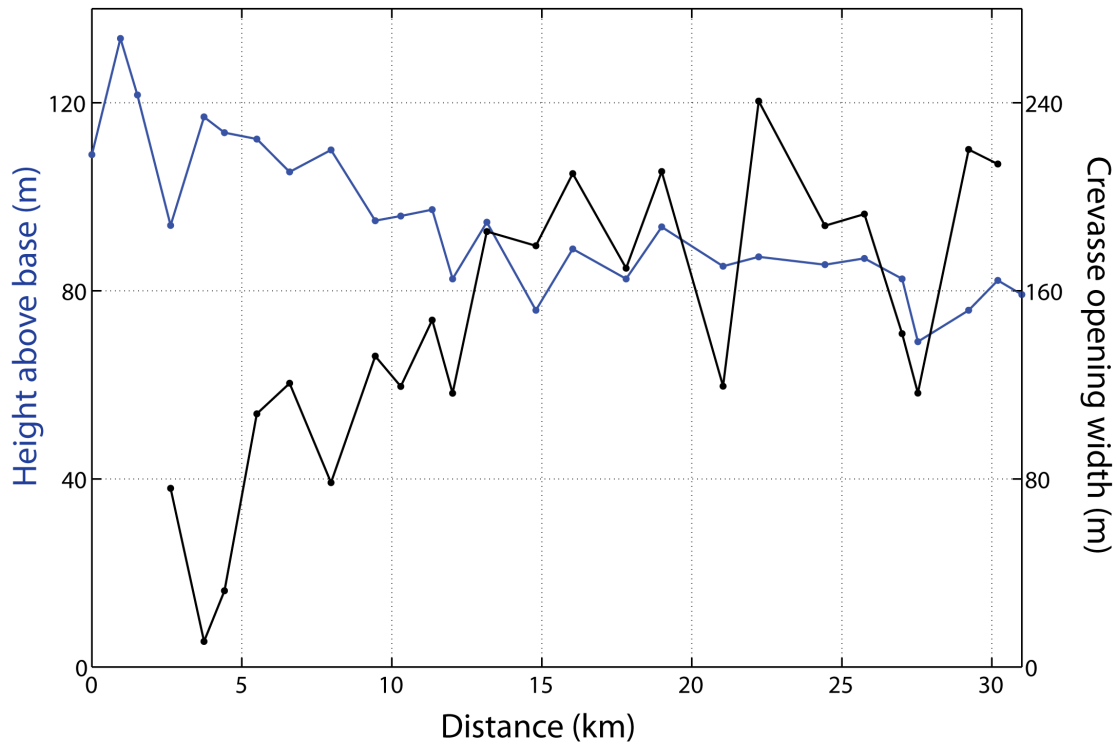


Figure 2.3. Observed crevasse penetration height (blue; left y axis) and crevasse opening width (black; right y axis) along radar transect.

troughs aligned with the basal crevasses, are observed along a 155 km flow line transect. High-resolution commercial visible imagery (GeoEye; 1.65 m resolution) clearly shows a lack of surface crevassing upstream of the origin of the basal crevasses (Figure 2.4a). Surface crevassing, first observed as narrow (1-5 m) bridged features, is apparent where the first surface undulations are observed (Figure 2.4b). The surface crevasses become increasingly abundant and well defined in the along flow direction, reaching widths of 8-24 m, while remaining primarily aligned with the crests of the surface undulations (Figure 2.4c).

2.4.3 - Model

We apply the model to examine basal crevasse propagation at the point of formation and do not intend to model propagation of pre-existing crevasses / undulations to changing conditions. Using reasonable parameters at the origin of the basal crevasses (ice thickness (H)=300m; surface temperature (T_s) = -12 °C; stretching rate (ϵ_{xx}) = 0.002 a⁻¹), the model predicts that if an initial basal fracture or flaw of ~2 m is present, the basal crevasse will propagate to a height of 128 m (Figure 2.5). This agrees well with radar observations of basal crevasse heights of 120 to 134 m near the beginning of the radar transect. The primary parameters that affect crevasse propagation are the stretching rate, ice thickness and surface temperature and hence we explore the sensitivity of basal crevasse propagation considering possible future changes affecting these parameters (*van der Veen*, 1998a). An increase in the stretching rate results in the largest increase in crevasse propagation height, as an increase from 0.002 to 0.003 or 0.004 a⁻¹, increases propagation height to ~166 m and ~205 m (Figure 2.5). For the subsequent three configurations, the stretching rate is held constant at 0.002 a⁻¹. The flow rate factor, which relates deviatoric stress and strain rate in Glen's flow law is temperature dependent, and hence if the mean surface temperature warms to -9 °C, basal crevasse height decreases to 106 m (Figure 2.5). If the ice shelf thins to 270 m, due to either increased basal or surface melting with subsequent runoff, basal crevasses will be able to propagate to a height of ~133 m, due to a reduction in the overlying lithostatic stress (Figure 2.5).

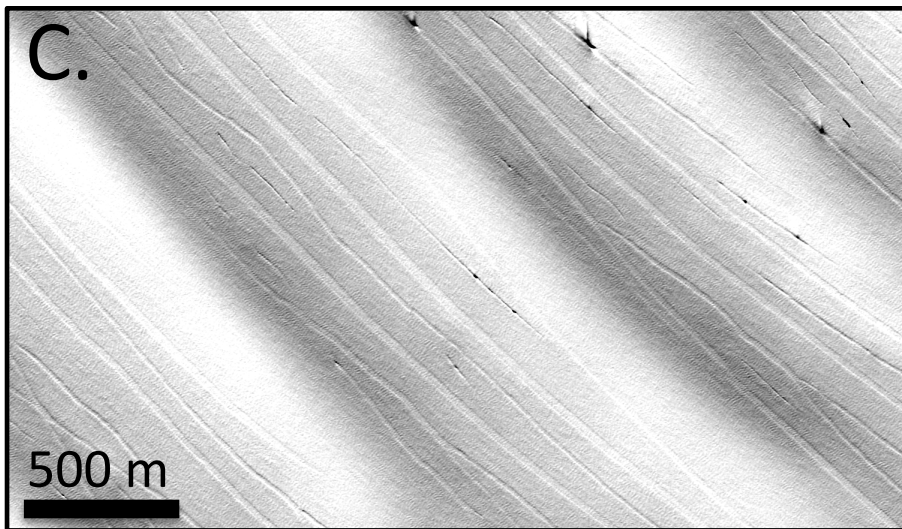
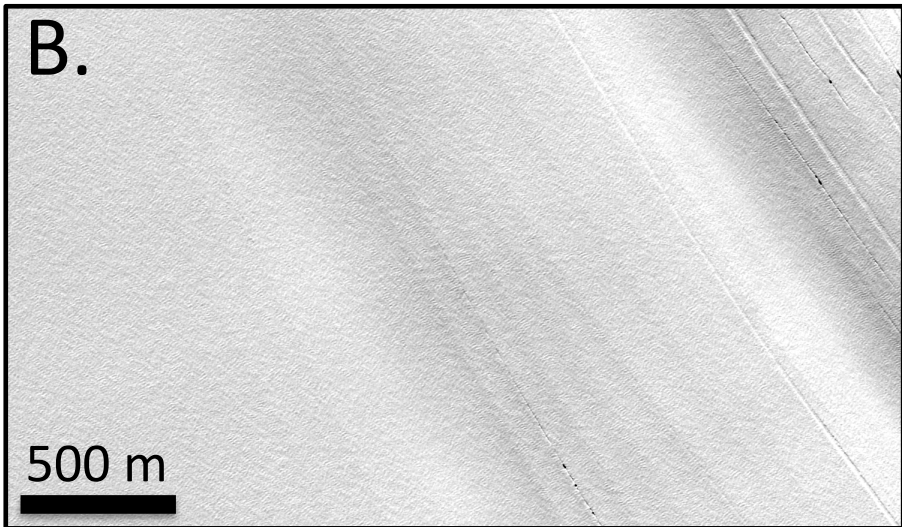
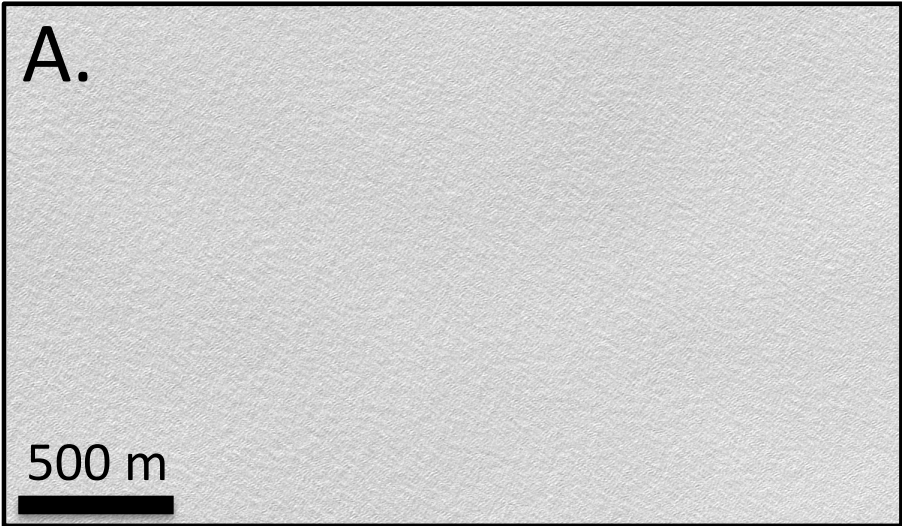


Figure 2.4. *GeoEye high-resolution (1.65 m) visible imagery of a) smooth ice shelf surface upstream of surface crevasses, b) initial surface undulations and development of surface crevasses and c) fully developed surface crevasses aligned with surface crests. Image locations are shown in Figure 2.1b. Copyright GeoEye Inc., 2011, provided by the NGA Commercial Satellite Imagery Program.*

2.5 - Discussion

We observe a series of basal crevasses, perpendicular to flow, in the northern sector of the Larsen C Ice Shelf. It is likely that these crevasses form as the outflow from Cabinet Inlet rounds Cape Alexander on Churchill Peninsula and subsequently accelerates and thins as it joins the main body of the ice shelf. Elevated stress in this region drives the formation and propagation of basal crevasses, which are subsequently advected towards the calving front, resulting in the series of surface undulations visible to the calving front (Figure 2.1a). Assuming that this is indeed the location and mechanism by which the basal crevasses form, this process has occurred for a minimum of ~400 years (based on the 155 km length of surface undulations and current surface velocity). The initial section of the radar transect shows numerous shallow and overlapping hyperbolas, indicative of a large number of small fractures (Figure 2.2). It is unclear how the evenly spaced, but not annually formed (i.e. spacing > annual velocity) basal crevasses observed along the length of the transect emerge from this highly fractured underside, and in particular, why certain fractures preferentially propagate. Regardless, this region of highly fractured basal ice certainly provides the necessary minimum flaw size (~2 m) for crevasse propagation (Figure 2.5; *van der Veen*, 1998a).

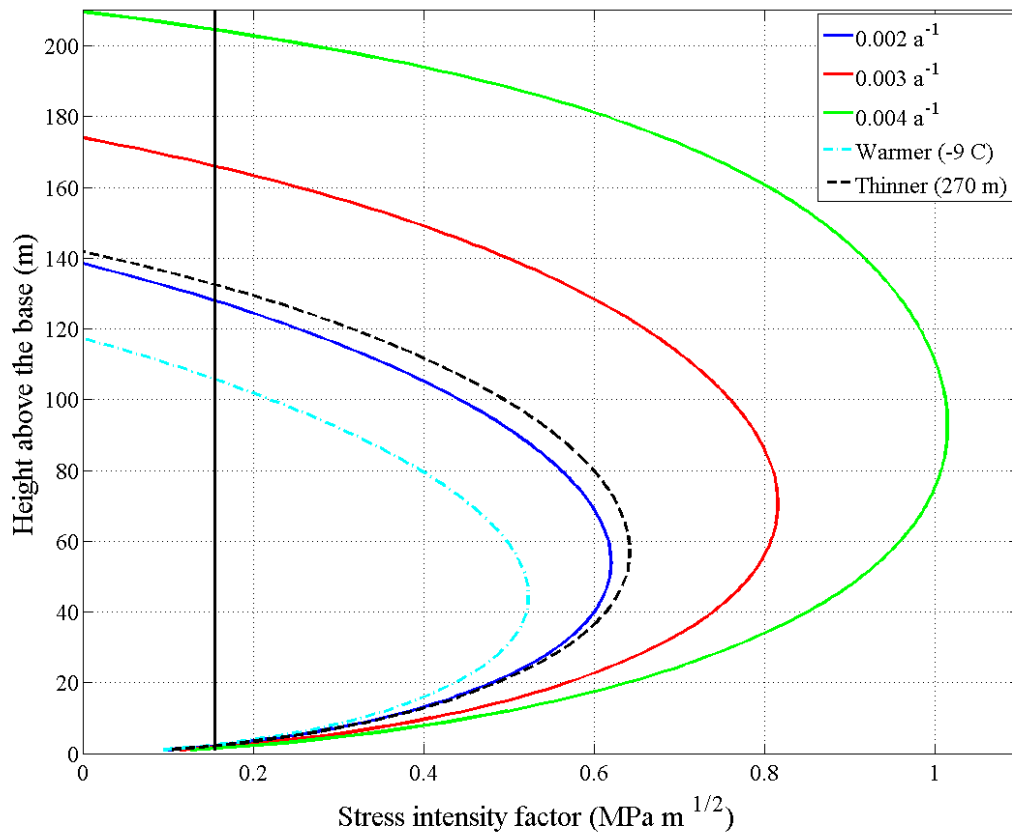


Figure 2.5. Stress intensity factor (K_I) as a function of height above the ice shelf base. Initial flaws that exceed the fracture toughness of the ice, defined as the critical stress intensity factor ($K_{IC}=0.155 \text{ MPa m}^{1/2}$; black vertical line) will propagate to the height where K_I equals K_{IC} . Using present-day ice shelf parameters ($H=300 \text{ m}$; $T_S=-12 \text{ }^\circ\text{C}$; $\varepsilon_{xx}=0.002 \text{ a}^{-1}$) an initial flaw of 2 m will propagate to a height of 128 m (blue line). Increasing the longitudinal stretching rate to 0.003 a^{-1} (red solid line) or 0.004 a^{-1} (green solid line) increases the height of penetration. A warmer surface temperature ($T_S=-9 \text{ }^\circ\text{C}$) reduces the height, due to the temperature dependent flow rate factor (cyan dot-dash line), while thinning the ice shelf ($H=270 \text{ m}$) increases crevasse propagation (black dash line).

Luckman et al. (2012) find a series of basal crevasses, similar in nature to these observed near Churchill Peninsula, but in a more southerly sector of Larsen C. These crevasses show the same quasi-periodic nature, with an average spacing of ~ 1 km, and form near the grounding line of Trail Inlet and similarly persist to the calving front. Observations of comparable crevasse heights and subsequently formed surface troughs give credence to the idea that basal crevasses are an abundant feature of the Larsen C Ice Shelf and not isolated to our study region. Thus, understanding their evolution is key to understanding the mechanical structure and stability of Larsen C.

Two distinct patterns emerge in the basal crevasse geometries along the transect that provide insight into the processes affecting their evolution (Figure 2.3). Penetration height of the basal crevasses decreases rapidly over the first 15 km, while crevasse-opening width increases substantially over this length (Figure 2.3). Both parameters show large variability but no net change over the final ~ 15 km of the transect. We suggest that the observed evolution towards wider and shallower features is likely the result of bending stresses, possibly in conjunction with marine ice accretion along the upper walls and apex of the basal crevasses. Another possibility for this evolution includes a melt-driven convective cycle within the basal crevasse, with basal melting along the lower walls and marine ice accretion at the top (*Khazendar and Jenkins, 2003*). We suggest, for multiple reasons, that bending stresses, expressed as an alternating pattern of compression and extension, are the dominant mechanism for the observed evolution in basal crevasse geometry.

In the simplest sense, if the ice shelf is thought of as an unconfined slab, floating in equilibrium within the ocean, the freeboard height is equivalent to the balance between the downward pointing lithostatic force of the ice column and the upward pointing buoyancy force. If the slab is perturbed by the addition of basal crevasses, there will be reduced buoyancy above these features, which, can be thought of as a downward negative force acting on the ice shelf surface aligned with these features. Thus, following the formation of a basal crevasse near Churchill Peninsula, the firn and ice above the crevasse vertically shears in an attempt to reach hydrostatic equilibrium, as seen by the downwarped firn layers above the basal crevasses in the radargrams (Figure 2.2). However, this ice is not an isolated column and is therefore partially supported by beam stresses from the neighboring ice of greater thickness (and hence greater buoyancy). Thus, the vertical shear above two neighboring basal crevasses induces a bending stress across the surface crest that separates the basal crevasses and results in the abundant surface crevassing observed in Figure 2.4c. This process is repeated for every basal crevasse and surface crest pair, creating alternating regions of compression in the surface troughs and extension over the surface crests, with the inverse of these forces on the underside of the shelf. This in turn explains the expansion of the basal crevasse opening width in the along flow direction (Figure 2.3).

Bending stresses have been observed in other contexts on floating ice shelves as well. *Casassa and Whillans* (1994) model the decay of surface topography on the Ross Ice Shelf and find that sinking regions of the ice shelf have compression at the ice surface and extension at the ice shelf base, while the opposite stress pattern is present in

neighboring regions. Similarly, *Jenkins et al.* (2006) hypothesize, based on measured strain rates, that vertical shear stresses exist within the ice shelf soon after flotation at the grounding line, to balance the gravitational forces as the ice shelf attempts to reach its equilibrium level. These stresses induce compression at the ice shelf surface and extension at the shelf bottom, in agreement with *Casassa and Whillans* (1994). Further, an outward bending stress exists at the calving front of ice shelves, as the hydrostatic pressure increases more rapidly with depth than the lithostatic stress in the ice column (*Scambos et al.*, 2009). This extensional stress drives surface crevasse formation (at a distance of ~ 0.7 * ice thickness from ice front), and may have played an important role in the breakup of the Wilkins Ice Shelf (*Scambos et al.*, 2009; *Braun et al.*, 2009).

The evolution of surface crevassing in the along flow direction provides direct visual support for this mechanism. Upstream of the basal crevasses, no surface crevasses are observed (Figure 2.4a) but following the initial formation of the basal crevasses, numerous, but narrow surface crevasses are observed at the crests of the low amplitude surface undulations (Figure 2.4b). These crevasses first form due to the extensional bending stresses at the crest surface invoked by vertical shear forces as the ice shelf attempts to reach hydrostatic equilibrium. Further along flow, surface crevassing is well defined, abundant and wide (8-24 m in width; Figure 2.4c) and found along the crests and upper flanks of the large amplitude surface undulations. Thus, the increased number and size of the surface crevasses correspond to a similar increase in undulation amplitude, indicative of an increase in vertical shear and extensional bending stresses. Once the ice shelf reaches approximate hydrostatic equilibrium, no further development of either

surface crevasses nor undulation amplitude occurs, suggesting that both the vertical shear and extensional bending stresses are substantially reduced. This is supported by the relative stability of basal crevasse height and opening width along the final 15 km of the radar transect, following rapid changes in both parameters over the first 15 km (Figure 2.3).

Luckman et al. (2012) find near-surface hyperbolic radar returns, indicative of surface crevasses along their radar transects, although they rarely observe them at the ice surface. Similarly, along our transect we also observe near-surface hyperbolic returns, although no surface crevasses were visually observed while conducting our radar surveys. We surmise that the surface crevasses are narrow in width and likely bridged by snow at the surface, in contrast to the large, exposed crevasses observed proximal to Churchill Peninsula. Regardless, these observations provide evidence of widespread surface crevassing on the Larsen C Ice Shelf, although they may often be bridged at the surface and thus, undetectable in both ground surveys and high-resolution (50 cm) satellite imagery.

Marine ice is believed to be an important component of the Larsen C Ice Shelf, particularly downstream of large promontories, where it likely sutures together neighboring flow bands while being advected to the calving front (*Holland et al.*, 2009; *Jansen et al.*, 2010). *Holland et al.* (2009) suggest that the greatest rate of marine ice accumulation occurs in the wake of Churchill Peninsula, as the large-scale geostrophic driven meltwater plume is forced out of the main Larsen C sub ice shelf cavity. Thus, this

plume represents a large source of meltwater, which, due to its buoyant nature, may enter a basal crevasse, becoming supercooled as it rises in the water column before accreting as marine ice along the upper walls and at the apex of the crevasse (*Khazendar and Jenkins, 2003*). However, the return in the radar from the apex of the crevasse does not systematically differ along the length of the profile, which might be expected if the apices were becoming filled with marine ice (Figure 2.2). However, it is unclear whether accreting marine ice would completely heal the crack, thereby removing the sharp corner reflector and preventing a radar return from this point. Further, some studies suggest that even if the apex were filled with marine ice, the radar return would still originate at the meteoric-marine ice interface due to the strong absorptive properties of the marine ice (*Lambrecht et al., 2007; Holland et al., 2009*). Therefore the radargrams are inconclusive as to whether marine ice is being deposited within the basal crevasses, although considering the overall evolution in crevasse geometry along the transect, this process is likely.

An alternative process that could lead to a similar evolution in basal crevasse shape is a melt-driven convective cycle within the crevasse, as modeled by *Khazendar and Jenkins (2003)*, that results in a widening of the base while depositing tens of meters of marine ice at the apex and along the upper walls. However, in this scenario, melting of the basal crevasse edges would lead to a rounding off of the bottom corners and a gradual fading of the radar hyperbolas that originate from these once sharp corners. Thus, as the bottom hyperbolas remain strong along the length of the profile, we do not believe that basal melting is occurring in earnest. Further, this melt-driven convective cycle does not

explain the formation of surface crevasses on the crests and thus, we suggest that the combination of bending stresses and possibly marine ice deposition, from a primarily distant meltwater source, is the more likely explanation for the observed evolution in basal crevasse geometry and surface crevasse formation.

Basal crevasses are inherently large-scale structural weaknesses within the ice shelf, that are further compounded by the fact that the ice shelf surface lowers above these features to maintain hydrostatic equilibrium (Figure 2.2; Figure 2.4c). Surface depressions are likely locations for meltwater to accumulate, as observed in the Crane Glacier domain of the Larsen B Ice Shelf prior to its breakup (*Glasser and Scambos, 2008*). Larsen C does not currently support widespread surface melt ponds, despite extensive surface melt during the summer months. Shallow firn cores (~7 m) in the vicinity of the radar profile contain thick, refrozen meltwater layers, suggesting that the shelf surface is evolving towards the point where it will be able to support melt ponds in the future. *Holland et al. (2011)* suggest 2-8 m of air content remains in the firn column along this transect, in contrast to ~20 m in the more southerly sectors of Larsen C. Thus, if the observed warming and subsequent increase in meltwater production continues along the AP, the northern sectors of Larsen C will likely support melt ponds in the near future. The hydrostatically adjusted surface troughs above the basal crevasses are likely locations for meltwater to pond, essentially creating small-scale catchment basins forming the requisite reservoirs needed for crevasse hydrofracture. This mechanism overcomes the necessity of very high ablation rates in order to produce enough meltwater to maintain surface crevasses at the critical threshold as they propagate further into the ice.

Surface crevasses, aligned along the crests and flanks of the surface undulations, are the result of an extensional bending stress induced by the presence of the basal crevasses and have important implications for ice shelf stability. First, without surface crevasses, meltwater is stranded on the ice shelf surface, with no means to propagate downwards. This is most clearly observed on George VI Ice Shelf, which undergoes extensive surface melt and ponding each summer, but is in compression between the peninsula and Alexander Island, and therefore lacks surface crevasses. This ice shelf has remained stable despite the abundant meltwater on the surface (*Cook and Vaughan, 2010*). In contrast, if the northern sector of Larsen C begins to support widespread melt ponds in the future, an extensive and well-developed surface crevasse network already exists to drain this meltwater. Second, if meltwater driven hydrofracture does occur in the future, Larsen C would be much more likely to undergo a disintegration style collapse, similar to Larsen A and B, than if the basal crevasses, with no surface crevassing, were to define future rifts. In this latter case, the dimensions of the subsequent icebergs would be stable (i.e. length (1200 m) >> height (300 m)). However, the presence of surface crevasses would likely render the ice shelf into narrow elongate blocks, which are gravitationally unstable and would quickly overturn, further contributing to the disintegration event (*MacAyeal et al., 2003*).

Despite the simplified geometry of the model, it accurately predicts the height to which the basal crevasses will propagate using current-day parameters for Larsen C. Current observations of ice shelf thinning and acceleration suggest that changes currently occurring on Larsen C will increase the overall stress intensity factor allowing new basal

crevasses to propagate further into the ice shelf. Warming atmospheric temperatures will oppose this increase, although there will be a substantial temporal lag for this forcing to equilibrate with the entire ice column. Thus, if the observed thinning and accelerating trends continue in the northern sector of Larsen C, it can be expected that new basal crevasses will propagate higher within the ice shelf.

2.6 - Conclusion

We identify twenty-seven basal crevasses along a 31 km transect on the northern sector of the Larsen C Ice Shelf. Widely spaced crevasses emerge from a region of multiple, shallow basal fractures and are found to initially penetrate to heights of ~130 m into the ice, the equivalent of ~40% of the ice thickness. The crevasses evolve along the length of the transect to become both shallower and broader features, most likely as a result of bending stresses and marine ice accretion in the crevasse apex. Application of the LEFM model accurately predicts the height to which the basal crevasses currently penetrate. Sensitivity studies of model parameters suggests that if the Larson C Ice Shelf continues to accelerate and thin, basal crevasses that subsequently form will penetrate higher within the ice shelf. Basal crevasses will control the distribution of meltwater on the ice shelf surface, resulting in ponds aligned with surface troughs. This creates the necessary reservoir for meltwater driven crevasse hydrofracture and provides the initial surface crevasses, increasing the risk that full-thickness rifts will form where surface and basal crevasses intersect. This points to the need to understand better ice shelf structure and the evolution of these features in a warming climate in order to understand and predict ice shelf disintegration.

Acknowledgments

This work is funded by NSF OPP research grant 0732946. The British Antarctic Survey provided exceptional field support, without which this work would not have been possible. M. van den Broeke provided the firm correction and E. Rignot provide InSAR derived surface velocities. Geospatial support for this work was supported by the Polar Geospatial Center under NSF OPP agreement ANT-1043681. We thank three anonymous reviewers and the scientific editor who provided constructive feedback that substantially improved this paper.

Chapter 3

Basal crevasses on the Larsen C Ice Shelf, Antarctica: Implications for meltwater ponding and hydrofracture

Published in *Geophysical Research Letters*, **39**, L16504, doi:10.1029/2012GL052413, 2012.

Abstract

A key mechanism for the rapid collapse of both the Larsen A and B Ice Shelves was meltwater-driven crevasse propagation. Basal crevasses, large-scale structural features within ice shelves, may have contributed to this mechanism in three important ways: i) the shelf surface deforms due to modified buoyancy and gravitational forces above the basal crevasse, creating >10 m deep compressional surface depressions where meltwater can collect, ii) bending stresses from the modified shape drive surface crevassing, with crevasses reaching 40 m in width, on the flanks of the basal-crevasse-induced trough and iii) the ice thickness is substantially reduced, thereby minimizing the propagation distance before a full-thickness rift is created. We examine a basal crevasse (4.5 km in length, ~230 m in height), and the corresponding surface features, in the Cabinet Inlet sector of the Larsen C Ice Shelf using a combination of high-resolution (0.5 m) satellite imagery, kinematic GPS and *in situ* ground penetrating radar. We discuss how basal crevasses may have contributed to the breakup of the Larsen B Ice Shelf by directly controlling the location of meltwater ponding and highlight the presence of similar features on the Amery and Getz Ice Shelves with high-resolution imagery.

3.1 - Introduction

A key mechanism for the rapid and catastrophic collapse of both the Larsen A and B Ice Shelves was meltwater-driven crevasse propagation (*Rott et al.*, 1996; *Scambos et al.*, 2000, 2003, 2009). This mechanism contends that when sufficient ponded meltwater drains into a surface crevasse, the crevasse will propagate through the entire ice shelf thickness (due to the density difference between water and ice), fracturing the ice shelf into numerous elongate icebergs (*van der Veen*, 1998b, 2007; *Scambos et al.*, 2003, 2009). The narrow along-flow width and elongated across-flow length of these icebergs distinguishes them from tabular icebergs, and likely facilitates a positive feedback during the disintegration process, as elongate icebergs overturn and initiate further ice shelf calving (*MacAyeal et al.*, 2003; *Guttenberg et al.*, 2011; *Burton et al.*, 2012).

Dramatic atmospheric warming over the past five decades has increased surface meltwater production along the Antarctic Peninsula (AP; *Vaughan et al.*, 2003; *van den Broeke*, 2005; *Vaughan*, 2006). As the summer air temperature of large portions of the AP hovers near 0 °C, the AP is sensitive to even a modest warming, unlike the interior regions of Antarctica (*Vaughan*, 2006). While the final disintegration of Larsen A and B has been attributed to meltwater-driven crevasse propagation, numerous processes pre-condition an ice shelf for rapid collapse (*Doake et al.*, 1998; *Vieli et al.*, 2007; *Khazendar et al.*, 2007; *Glasser and Scambos*, 2008). Firn densification and melt layer formation allow surface melt ponds to form on the shelf surface, a process that can take multiple melt seasons to accomplish (*Scambos et al.*, 2000, 2003). Concurrently, increased basal submarine melting or reduced marine ice accretion can thin an ice shelf and reduce the cohesion between parallel flow

bands and / or shear margins (*Glasser and Scambos, 2008; Jansen et al., 2010*). This may lead to ice flow acceleration, with increased crevassing and rifting due to elevated strain rates, as observed on Larsen B prior to its collapse (*Rignot et al., 2004*). Increased calving and subsequent frontal retreat is also a clear harbinger of ice shelf disintegration, particularly if the ice front retreats past a critical compressive arch in the strain field, at which point substantial retreat will occur before reaching a new stable configuration (*Doake et al., 1998*).

Larsen C is the largest remaining ice shelf on the AP, consisting of over 50,000 km² of floating ice, which is fed from 12 major outlet glaciers (Figure 3.1a; *Glasser et al., 2009; Cook and Vaughan, 2010*). The extent of Larsen C has been relatively stable over the last five decades, outside of calving events in 1986 and 2004/05 where the ice shelf lost ~7700 km² and ~1500 km², respectively (*Glasser et al., 2009; Cook and Vaughan, 2010*). Despite limited changes in extent, the surface elevation of Larsen C has lowered at a rate of between 0.06 and 0.09 m a⁻¹ during the 1978-2008 period, with the greatest lowering occurring in the northern sector (*Fricke and Padman, 2012*). This surface lowering is likely dominated by firn densification driven by warmer air temperatures and increased meltwater production / refreezing (*Holland et al., 2011; Fricke and Padman, 2012*) rather than increased basal melting driven by an ocean forcing (*Shepherd et al., 2003*). Oceanographic observations suggest that the primary water mass in the Larsen C cavity is Modified Weddell Deep Water, which has been cooled to the surface freezing point and therefore unlikely to drive high basal melt rates (*Nicholls et al., 2004*). *Khazendar et al. (2011)* found that the northern sector of the ice shelf accelerated by 80 m a⁻¹ or 15% between 2000 and 2006, and a further 6-8% between 2006-2008 in the vicinity of Cabinet Inlet, possibly due to a reduction in back stress

from the Bawden Ice Rise and/or the erosion of marine ice formerly suturing parallel flow bands together.

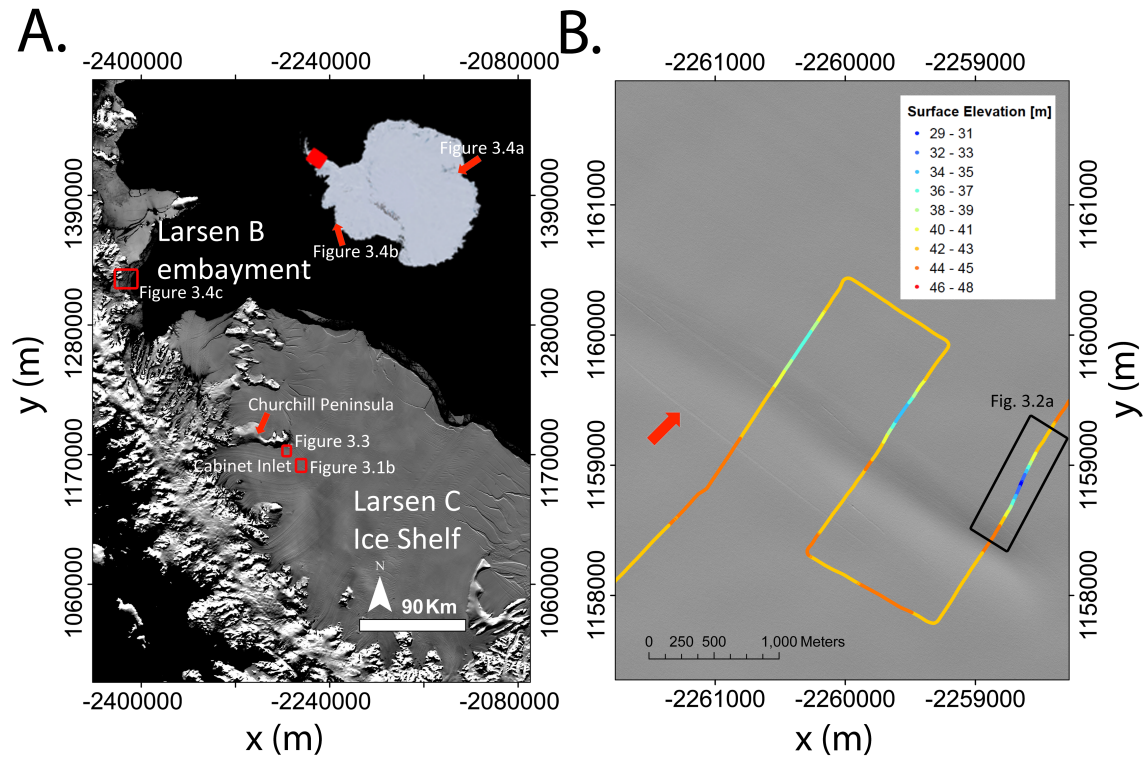


Figure 3.1. a) Subsection of MODIS MOA mosaic detailing the Larsen C Ice Shelf (Haran et al., 2006). White boxes indicate location of Figure 3.1b and red arrows on inset indicate location of Figure 3.4. Coordinates are polar stereographic (at 71° S secant plane, 0° meridian) where x is easting and y is northing.

b) High-resolution (0.5 m) visible imagery of surface depressions and surface crevasses, located on flanks of the depressions. Surface elevations from kinematic GPS are shown as colored transect. Black box indicates location of radar profile shown in Figure 3.2a. Red arrow is aligned with flow direction and identifies bridged surface crevasses. Note spatial offset between depression in kinematic GPS data and visual imagery due to temporal offset between image and GPS collection. Imagery Copyright GeoEye Inc., 2011.

Airborne radar surveys, beginning in the late 1970s, identified large hyperbolic radar returns, interpreted as basal crevasses, within the Ross (*Jezeq et al.*, 1979; *Shabtaie and Bentley*, 1982), Larsen (*Swithinbank*, 1977), and the Riiser-Larsen Ice Shelves (*Orheim*, 1982). Despite the magnitude and abundance of these features, they have received relatively little attention, especially in light of recent ice shelf disintegrations. Recent work by *Bindschadler et al.* (2011a), *Humbert and Steinhage* (2011), *Luckman et al.* (2012), and *McGrath et al.* (2012) has identified numerous basal crevasses, and their corresponding surface expressions, on the Pine Island Glacier, Fimbul and Larsen C Ice Shelves. Basal crevasses in two different regions on Larsen C penetrate between 69 and 217 m into the overlying ice shelf, representing between ~ 24 and 66% of the ice thickness and likely have basal opening widths ranging from tens to hundreds of meters (*Luckman et al.*, 2012; *McGrath et al.*, 2012). In addition to representing structural weaknesses in the ice shelf, basal crevasses also modulate the exchange of mass and energy between the ice shelf and ocean by increasing both the ice-ocean interface area (*Luckman et al.*, 2012) and the basal surface roughness. It is difficult to speculate the net basal melting or accretion due to the presence of basal crevasses, as these processes are dependent on unknown ocean properties and circulation in close proximity to the basal crevasses.

3.2 - Methods

Analysis of the surface depressions and crevasses was conducted using a subset of the MODIS Mosaic of Antarctica (*Haran et al.*, 2006; 125 m resolution), Landsat 7 ETM+ imagery (Band 8; 15 m resolution; collected 15 December 2001), a GeoEye-1 panchromatic image (0.5 m resolution; collected 25 February 2010) and WorldView-1 panchromatic

imagery (0.5 m; collected 24 November 2008 and 18 October 2009). Radar surveys (Figure 3.2a, 3.3b) were conducted with a Malå Geosciences ground based pulse radar system with a 25 MHz antenna towed behind a snowmobile. The *in situ* data, including kinematic GPS, were collected in November 2011, and therefore a temporal (and hence spatial) offset exists between the *in situ* data and the imagery (Figures 3.1b, 3.3a). Following previous studies (Luckman *et al.*, 2012; McGrath *et al.*, 2012), the measured two-way travel time was converted to depth assuming a mean radar velocity of 0.173 m ns^{-1} . The ice shelf-ocean interface reflection was manually delineated along the profile by following the maximum echo amplitude in the radar waveform. Uncertainty in the derived ice thickness is assumed to be $\pm 5\%$ due to uncertainty in radar velocity and resolution of radar wavelength.

Simultaneous position data were collected with a dual-frequency GPS and corrected to the Eigen GL04C ellipsoid (Förste *et al.*, 2008) and further corrected for tidal amplitude using Circum-Antarctic Tidal Simulation version 2008a (CATS2008a), updated from Padman *et al.* (2002).

3.3 - Results and Discussion

Visible imagery details a series of isolated surface depressions in the main outflow of Cabinet Inlet, extending seaward to the calving front (Figure 3.1a). We focus our observations on one of these features (Figure 3.1b). The surface depression has a maximum depth of 13.0 m and extends for 4.5 km, as measured from kinematic GPS and imagery, respectively (Figure 3.1b). A large hyperbolic reflection within the ice column is aligned with the surface depression, which we interpret as the apex of a basal crevasse (Figure 3.2a). It extends $233 \pm 11 \text{ m}$ in height from the base of the ice shelf, penetrating through over 66%

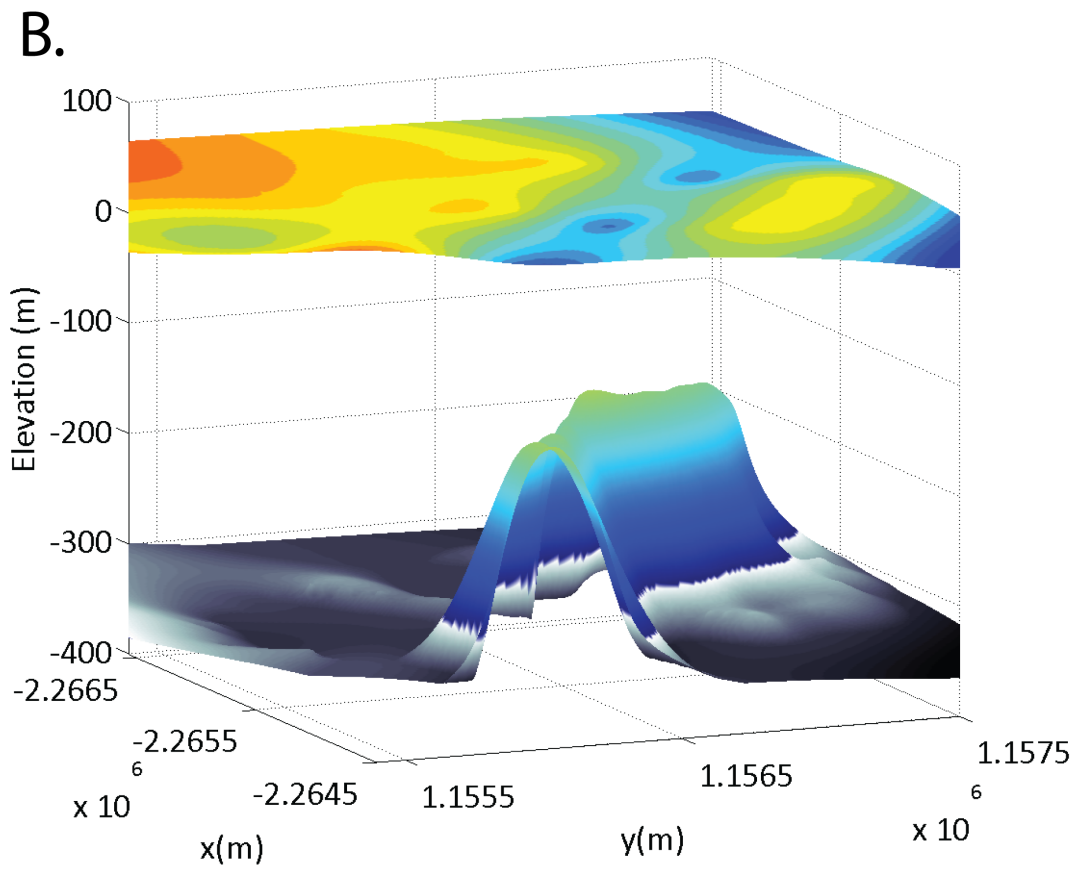
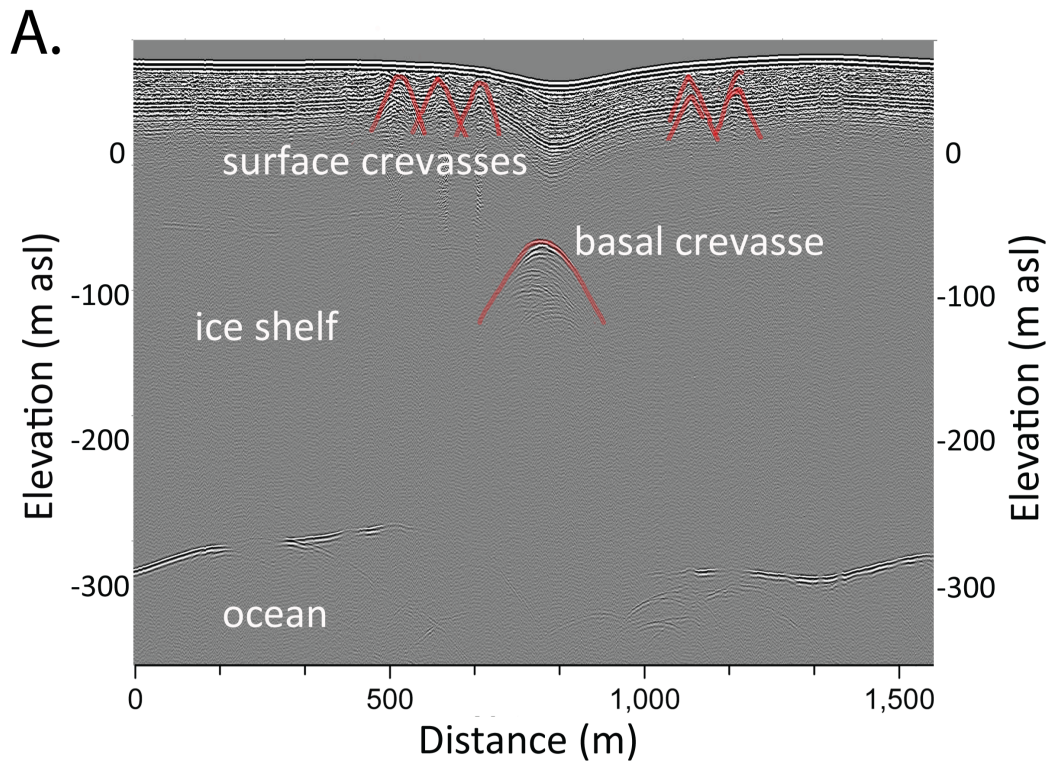


Figure 3.2. *a) 25 MHz radar profile across basal and surface crevasses. Surface elevations have been corrected to reflect ice shelf topography. Note down warping of firn above basal crevasse and hyperbolas on the flanks, highlighted in red, interpreted as surface crevasses. b) Three-dimensional view of the basal crevasse penetrating into the ice shelf. Surface and basal interface interpolated from GPS and GPR profiles, respectively.*

of the mean local ice thickness and is 470 m in width (Figure 3.2a and b). The size of the basal crevasse increases the local ice-ocean interface by ~30% relative to a flat-bottomed ice shelf. Above the hyperbolic reflection, the firn and upper ice layers down warp by 15-20 m (Figure 3.2a). Numerous snow-bridged surface crevasses, with widths between 20-25 m, are aligned parallel to the basal crevasse but on the down sloping flanks of the surface depression, as observed in both the visible imagery (Figure 3.1b; shadowed features indicated by red arrow) and in the hyperbolic reflections in the upper 10 m of the radargram (Figure 3.2a; highlighted in red).

We attribute the formation of the surface crevasses to bending stresses induced as the ice shelf surface deforms in order to reach a modified hydrostatic equilibrium (McGrath *et al.*, 2012). We offer the following observations here to support this hypothesis. We observe two nascent basal crevasses, which are located upstream from the series that extend seaward from Churchill Peninsula, which have propagated to a similar height but have limited surface deformation (1-4 m) and no apparent surface crevassing (Figure 3.3). Further along flow (i.e. with increased temporal evolution), the basal crevasses have clearly defined surface depressions, down warped firn and ice layers above the basal crevasse and numerous surface

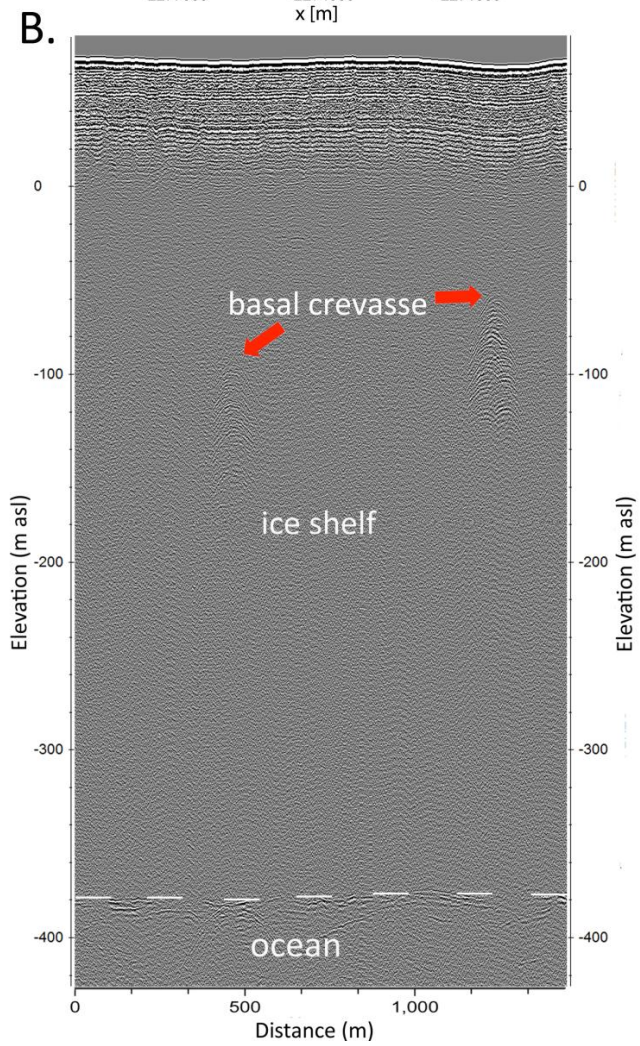
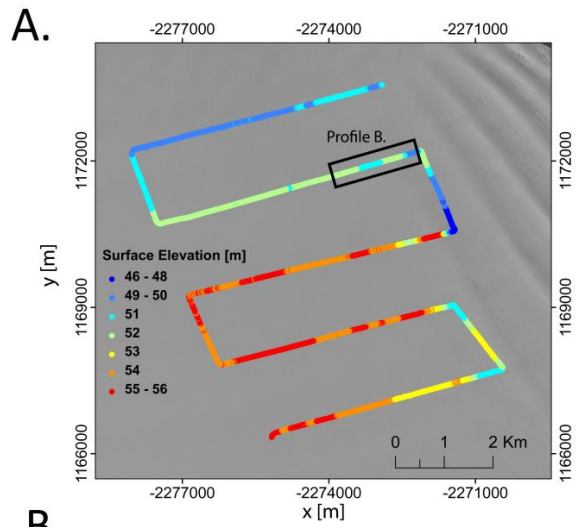


Figure 3.3. *a) Surface elevations along radar transect (shown in part b). Note spatial offset between depression in kinematic GPS data and visual imagery due to temporal offset between image and GPS collection. b) 25 MHz radar profile across basal crevasses (apices indicated by red arrows). Surface elevations have been corrected to reflect ice shelf topography. Note reduced surface deformation and lack of surface crevassing.*

crevasses adjacent to the basal crevasse (McGrath *et al.*, 2012). Together, these observations suggest that the basal crevasse forms first, subsequently followed by surface deformation, the visco-elastic response to the reduced ice thickness above the basal crevasse. However, as this thinner section is partially supported by the full thickness ice to either side, the resulting geometry induces bending stresses, with tension across the crests and down the flanks, sufficient to induce surface crevassing, and compression in the surface depressions, which are free of surface crevasses (Figure 3.1b).

We now highlight similar surface features, using a combination of Worldview-1 and Landsat imagery, which we interpret, based on their similarity to Larsen C, as the surface expressions of basal crevasses on the Amery, Getz and former Larsen B Ice Shelves. The stress environment causing the basal crevasses to form is different for each ice shelf, yet they all support the notion that basal crevasses can induce surface crevassing and create a surface depression, thereby controlling the location of meltwater ponding. In the eastern section of the Amery Ice Shelf, a series of surface depressions originate in the vicinity of the Gillock Island and extend across-flow by ~40 km (Figure 3.4a). Numerous surface crevasses (~4-8 per crest; 10-40 m in width) are located on the topographic crests between depressions and

aligned parallel with them, whereas the depressions themselves are free of surface crevasses (Figure 3.4a). Likewise, a series of front parallel, but slightly sinuous surface depressions extend over 20 km near the calving front of the Getz Ice Shelf in the Amundsen Sea sector (Figure 3.4b). Similarly, ~4-8 surface crevasses, 10-40 m in width are aligned with the basal crevasses, although some extend slightly oblique to the main orientation of the surface depression, which we interpret as being due to a more complex stress environment. Prior to the disintegration of the Larsen B Ice Shelf, the floating outflow of the Hektor-Green-Evans glacier system had numerous surface crevasses, which had formed *parallel* to flow direction and termed ‘splaying crevasses’ (Figure 3.4c; *Glasser and Scambos, 2008*). The surface crevasses were most abundant on the topographic crests, and were separated by large-scale (10-15 km) linear surface depressions, likely underlain by basal crevasses (Figure 3.4c). Prior to breakup, discrete meltwater ponds were abundant in the surface depressions, highlighting how such structural features can control meltwater ponding on the shelf surface. Subsequent pond drainage prior to the breakup of Larsen B indicates that a connection was made to the ocean, likely through meltwater-driven crevasse propagation (*Scambos et al., 2003*). Both the proximity of this meltwater to widespread surface crevassing and the subsequent iceberg dimensions, which largely overturned during the disintegration event, suggest that crevasse propagation did occur and that the fracture spacing in this sector was likely governed by the surface crevasse spacing (*Scambos et al., 2003*).

3.4 - Implications

Meltwater-driven hydrofracture, the process by which water filled surface crevasses fracture downwards, has been suggested to be an important mechanism in the final breakup of several

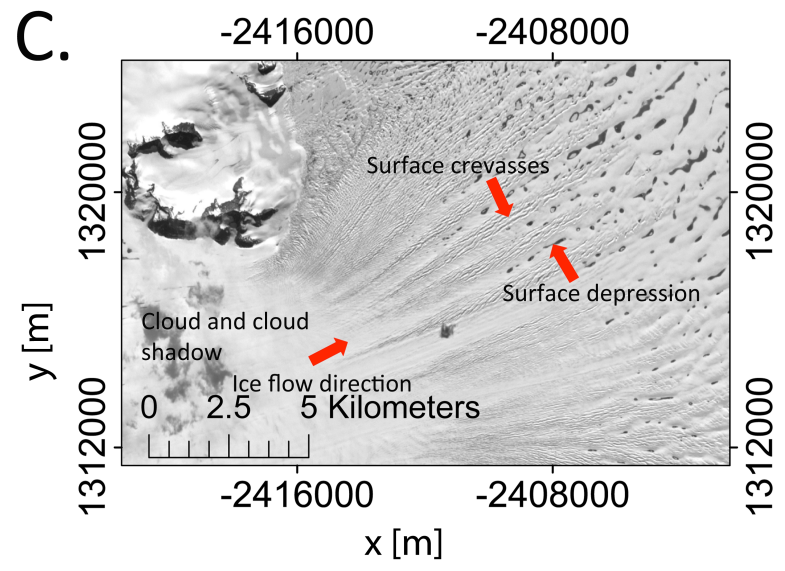
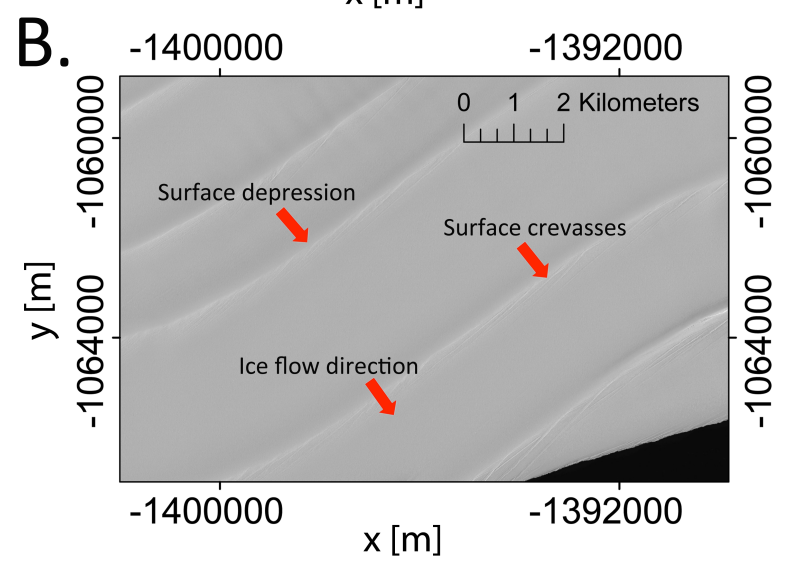
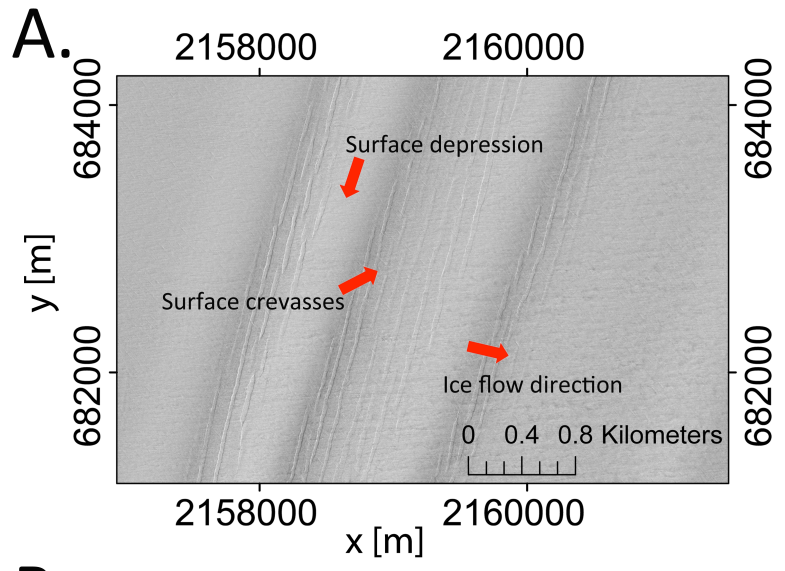


Figure 3.4. *Visible imagery detailing surface depressions, believed to be underlain by basal crevasses, and surface crevassing on the a) Amery, b) Getz and c) former Larsen B Ice Shelves. Locations are indicated in Figure 3.1a. Imagery (a,b) Copyright Digital Globe Inc., 2012.*

ice shelves (Weertman, 1973; van der Veen, 1998b, 2007; Scambos *et al.*, 2000, 2003). We have shown that basal crevasses, beyond introducing large-scale ice shelf weaknesses, can create both surface depressions and surface crevasses. The most apparent implication of meltwater ponding in the surface depression is if the meltwater were to intersect a flanking surface crevasse, and subsequently establish a channel by which the pond could drain, thereby providing the necessary water volume for continued fracture. Perhaps less obvious, however, is that the increased load in the trough will increase extensional stresses along the flanks and in the vicinity of the basal crevasse apex, potentially leading to further propagation and the possibility for a shear fracture to connect these features (Bassis and Walker, 2012). This structural weakness could be further exploited if hydrofracture originates from the base of the surface trough, where the hydrostatic pressure is the greatest, and where, despite the large-scale compressional environment, incipient surface cracks / fractures are still likely to be present (Fountain *et al.*, 2005). The presence of the basal crevasse greatly reduces the ice thickness in the vicinity, thereby minimizing the distance through which these small fractures have to propagate prior to creating a full-thickness rift. While the surface crevasses certainly weaken the ice shelf, this latter case highlights the possibility that it is the presence of the basal crevasse that is more important for ice shelf stability. Basal crevasses are an order of magnitude larger in width and depth than the surface crevasses they create,

and by concentrating meltwater ponding directly above them, they can control fracture location, and therefore, ice shelf disintegration.

In addition to the observations of melt pond drainage on Larsen B, sediment cores retrieved from beneath both the former Larsen A and Prince Gustav Ice Shelves, record spatially discrete sediment pulses interpreted as the drainage of supraglacial lakes and/or crevasses prior to the ice shelf disintegration event (*Gilbert and Domack, 2003*). Together, these observations provide clear evidence that fractures do propagate through the ice shelves, although the location where the hydrofracture originated is unclear (i.e. whether it was a proximal surface crevasse or incipient flaw beneath the pond). A corollary can be drawn to supraglacial lake drainage on the Greenland Ice Sheet, where fractures, and later moulins, develop within the lake boundary (*Das et al., 2008*). Thus, if hydrofracture does originate from within the pond boundary, the presence of the basal crevasse should make the formation of a full-thickness rift exceedingly efficient.

Previous studies have concluded that the Larsen C Ice Shelf is largely stable and unlikely to experience a catastrophic collapse at present, despite observations of thinning and flow acceleration in the northerly sector (*Jansen et al., 2010; Khazendar et al., 2011*). Basal crevasses have likely been present on the ice shelf for at least the last ~400 years (*McGrath et al., 2012*) and thus, are not likely a reflection of the recent changes in ice shelf thickness or speed, nor suggest that Larsen C is becoming unstable (*Khazendar et al., 2011*). In order for basal crevasses to affect the stability of Larsen C, both meltwater production and meltwater ponding would need to increase significantly. At present, only a limited number of melt

ponds form each summer, most commonly near the Cabinet Inlet grounding line, likely in response to föhn airflow over the peninsula (*van den Broeke, 2005*). While melting ponding is spatially limited at present, it is likely that firn densification has significantly contributed to the observed surface lowering over the past three decades (*Holland et al., 2011; Fricker and Padman, 2012*). If the long-term temperature trends on the AP continue (*Vaughan et al., 2003*), increased meltwater production and firn densification is likely, in which case, basal crevasses and their surface expressions, including both depressions and crevasses, could have a significant role in future ice shelf disintegration events.

Acknowledgments

This work is funded by NSF OPP research grant 0732946. The British Antarctic Survey and field assistant, Tom Weston, provided exceptional field support, without which this work would not have been possible. Geospatial support for this work was supported by the Polar Geospatial Center under NSF OPP agreement ANT-1043681. Careful reviews by Jeremy Bassis and two anonymous reviewers significantly improved the manuscript.

3.5 - Elastic Beam Model

To illustrate the nature of bending stresses induced by basal crevasses, we take an elastic bending beam approach, using a relatively low effective elastic modulus for ice to account for the viscoplastic response over the long time scales associated with the basal crevasse loading (*Sinha, 1978*). Although simplified, this approach illustrates that the ice shelf surface deforms vertically in response to the addition of a basal crevasse, and that the bending stresses invoked during this process are sufficient to result in surface crevassing. The 1D model domain is a section of ice shelf 1000 m long in the along flow direction and 370 m thick in the vertical. The domain is perturbed by a single basal crevasse ~500 m in width and ~230 m in height (based on field observations). We assume force equilibrium across this reach of ice shelf, with local negative loading at the basal crevasse location due to reduced buoyancy and a small positive loading elsewhere. We implement boundary conditions of zero deflection (y) and zero surface slope at the lateral edges of the domain (i.e. at $x=0$ and $x=1000$). The zero deflection boundary condition merely sets the elevation of the ice shelf far away from the basal crevasses, and deflections are with respect to this reference elevation. The problem is statically indeterminate and thus, we numerically solve the Euler-Bernoulli equation for the deflection at each position x :

$$\frac{d^2}{dx^2} \left(EI \frac{d^2 y}{dx^2} \right) = p(x), \quad \text{Equation 3.1}$$

where E is the effective elastic modulus (5.5 MPa), I is the area moment of inertia and p is the loading. The bending moment, M , is calculated at each node as:

$$M = -EI \frac{d^2 y}{dx^2}. \quad \text{Equation 3.2}$$

The bending stress (σ) can be solved for as:

$$\sigma = \frac{M(\zeta)}{I}, \quad \text{Equation 3.3}$$

where ζ is the distance from the neutral axis. Positive stresses are compressive and negative stresses are extensional.

We choose an effective elastic modulus of 5.5 MPa to match the magnitude of the modeled deflection to that of the observed deflection (Figure 3.5a). This value is significantly lower than laboratory measurements, which typically range between 3-10 GPa, and those inferred by applying an elastic beam model to match field observations at tidal frequencies (0.88 GPa) (*Vaughan, 1995*; references therein). The inherent relation between stress and strain in a viscoplastic material, in this case ice, is that the deformation is time-dependent, and hence the effective elastic modulus decreases non-linearly with increased time of loading (*Sinha, 1978*). By relaxing the value of E to obtain the observed deflection, thereby approximating the viscoplastic response of ice over years to decades, we can assess the relative geometry of the deflected surface and the stress distribution within the beam. The modeled stress fields have extensional stress at the lateral edges of the beam surface and compression on the surface in the center (Figure 3.5b). The opposite stress pattern is apparent at the beam bottom. This stress distribution is in agreement with previous modeling work by *Casassa and Whillans (1994)* and *Jenkins et al. (2006)*. Modeled extensional stresses exceed the fracture toughness of ice ($\sim 150 \text{ kPa m}^{1/2}$; *Rist et al., 2002*) along the flanks of the depression, suggesting that surface fracture propagation is likely. This suggests that surface crevasses are induced by the bending stresses related to the ice shelf surface down warping over basal crevasses. High extensional stresses are also present at the basal crevasse tip, although, it is unclear

whether continued propagation occurs in the field. Two possible explanations which would limit continued propagation in the field include the loss of a distinct fracture tip at the apex of the basal crevasses at which to concentrate the stresses and the presence of adjacent blocks, (in this case separated by neighboring basal crevasses) which would oppose one another, thereby reducing modeled stresses.

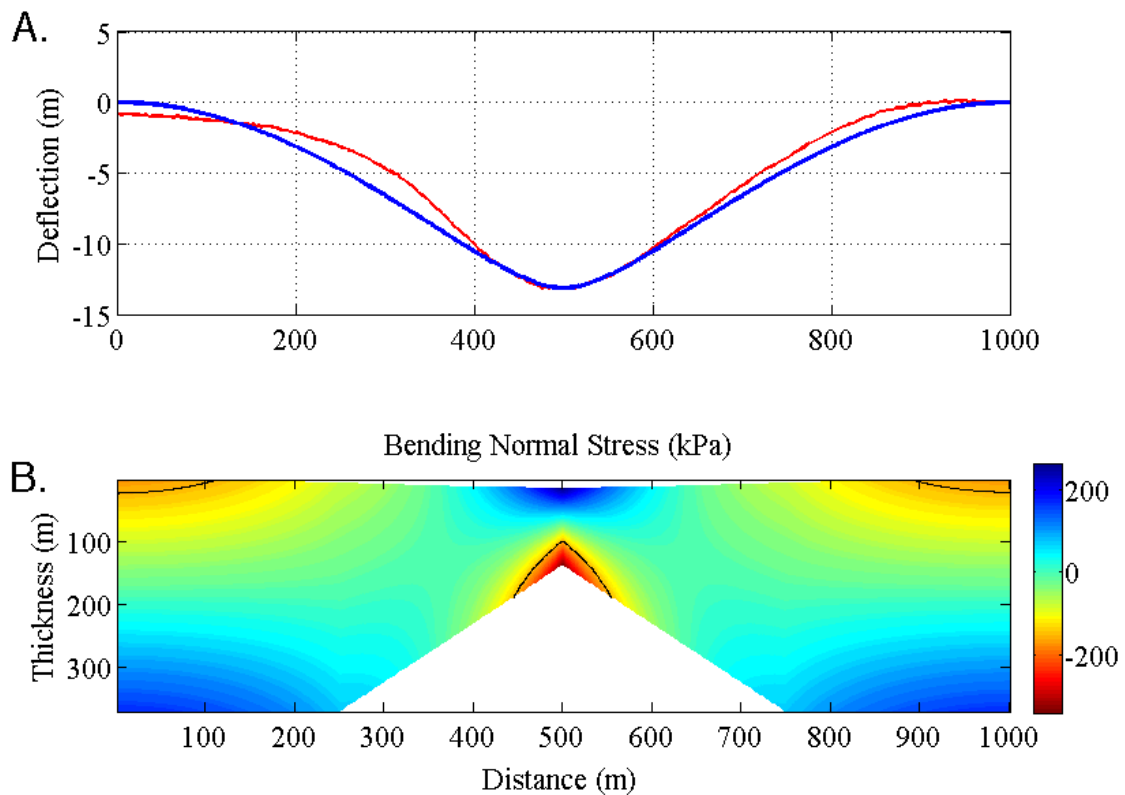


Figure 3.5. a) Downward deflection of beam surface in response to negative loading corresponding to the addition of the basal crevasse (blue) relative to observed surface elevation (normalized to zero; red).

b) Normal bending stresses in beam. Compressive stresses are positive and extensional are negative. Contour of extensional stress of -150 kPa (fracture toughness of ice) is shown in black.

Chapter 4

The structure and effect of suture zones in the Larsen C Ice Shelf, Antarctica

To be submitted to *Journal of Geophysical Research-Earth Surface*.

Abstract

Ice-shelf fractures frequently terminate where they encounter suture zones, regions of material heterogeneity that form between meteoric inflows in ice shelves. This heterogeneity can consist of marine ice, meteoric ice with modified rheological properties due to past shear, or the presence of fracture. Here we use radar observations on the Larsen C Ice Shelf, Antarctica to investigate i) the termination of a 25 km-long rift in the Churchill Peninsula suture zone, which was found to contain ~60 m of accreted marine ice, and ii) the along-flow evolution of a suture zone originating at Cole Peninsula. We determine a steady-state field of basal melting/freezing rates and apply it to a flowline model to delineate the along-flow evolution of layers within the ice shelf. The thickening surface wedge of locally accumulated meteoric ice, which likely has limited lateral variation in its mechanical properties, accounts for ~60% of the total ice thickness near the calving front. Thus, we infer that the lower ~40% of the ice column, and the material heterogeneities present there, are responsible for resisting fracture propagation and thereby delaying tabular calving events, as demonstrated in the >40 year time series leading up to the 2004/05 calving event for Larsen C. This likely represents a highly sensitive aspect of ice-shelf stability, as changes in the oceanic forcing may lead to the loss of this heterogeneity.

4.1 - Introduction

Early surveys of the Larsen Ice Shelf by *Mason* (1950) and *Fleet* (1965) described the complex surface, including large-scale rifts and “lenticular holes,” later termed dolines. The first comprehensive airborne radar echo soundings of Larsen C helped elucidate the composite nature of the ice shelf, in that a number of glaciers had a “pronounced effect on the ice thickness” (*Smith*, 1972). *Smith* (1972) suggested that the large seaward protrusion in the southeasterly sector of the ice shelf (which subsequently calved off in 1986) might be related to the high flux of grounded meteoric ice from Mobiloil Inlet (Figure 4.1). However, between these major inflows of meteoric ice are large peninsulas that limit the flux of meteoric ice across the grounding line into these domains, resulting in surface depressions, and hence, thickness anomalies (*Ridley et al.*, 1989).

From these early observations, a more complete picture of ice shelf structure has emerged. Ice shelves typically form within an embayment, where the lateral walls and often the presence of ice rises/nunataks produce lateral and longitudinal back stresses that resist ice flow. As a distinction from ice tongues, ice shelves are typically composed of numerous inflows of meteoric land ice, derived from snowfall on the continent, which are separated by bands of relatively thin ice that form in the downstream wake of peninsulas and are termed suture zones. These zones are often comprised of an ice mélange, largely believed to be composed of marine ice either accreted from supercooled rising meltwater or from seawater flooding firm proximal to rifts, sea ice (frozen from above), fallen meteoric blocks, and in situ snowfall (*Glasser et al.*, 2009), which gets laterally squeezed by the

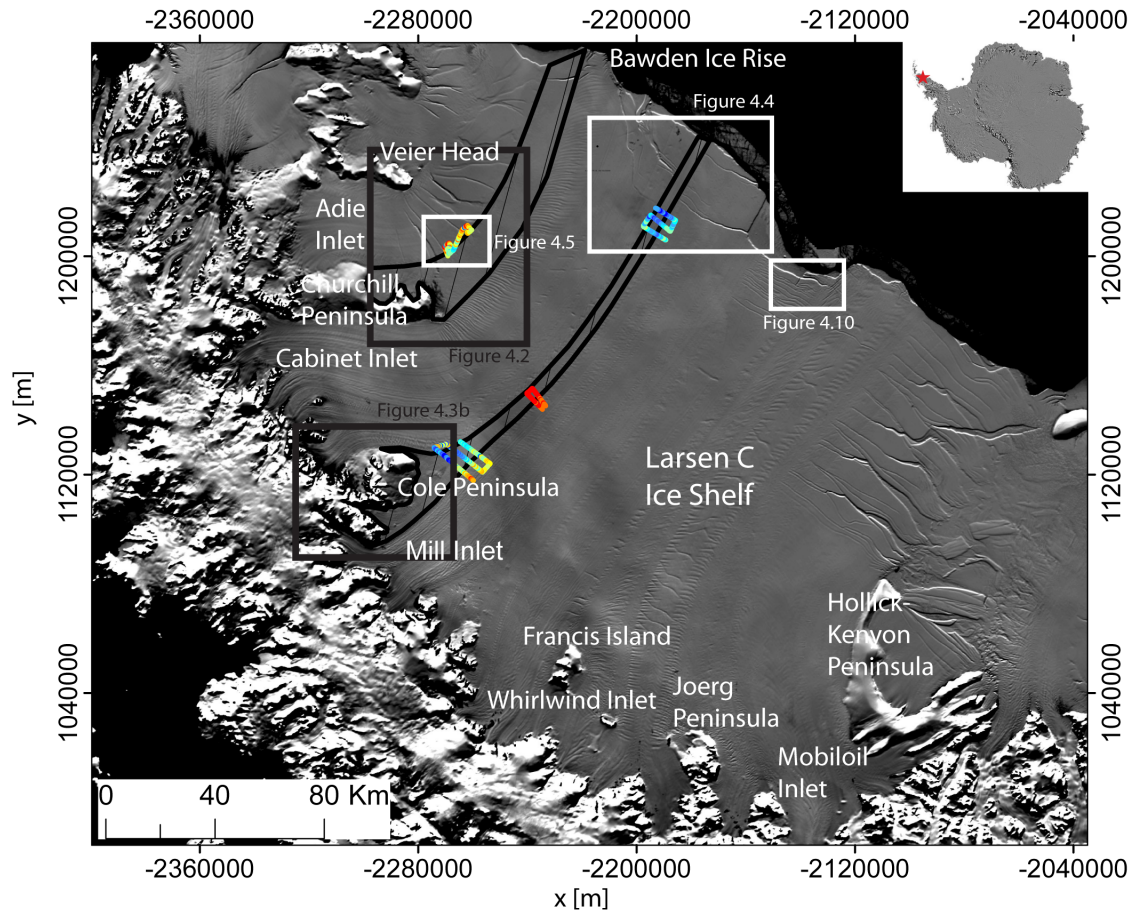


Figure 4.1. MODIS Mosaic of Antarctica (MOA; Haran et al., 2005) of the Larsen C Ice Shelf with prominent geographic features labeled. Labeled boxes outline figure locations. Inset: Location of the Larsen C Ice Shelf on the Antarctic Peninsula. Coordinates are polar stereographic (at 71° S secant plane, 0° meridian, WGS84 ellipsoid) where x is easting and y is northing.

divergent spreading flow of thicker meteoric inflows on either side. As suture zones are typically thinner, more fractured, and lack the coherent structure found in meteoric inflows, they are typically seen as weak points in ice shelves.

A key component of the suture zone mélange is marine ice, which forms when plumes of buoyant ice-shelf meltwater rise and then supercool due to the reduction in pressure (*Robin, 1979*). Beneath Larsen C, a likely source of such meltwater is basal melting of the deep meteoric inflows closest to the grounding line (*Holland et al., 2009*), where the thermal forcing is greatest due to the depression of the melting point of ice at elevated pressures. The rising meltwater plumes that result refreeze to the ice shelf at shallower depths, most commonly in ice draft minima found downstream of peninsulas (*Holland et al., 2009*). Other possible sources of meltwater occur where rapid tidal currents induce high basal melt rates, often near the calving front and along certain peninsulas / ice rises (*Mueller et al., 2012*).

Two additional processes may contribute to the formation of marine ice as well, although both likely operate on smaller spatial scales than the process previously described. Basal melting may occur at the edge of individual rifts, which can drive a similar, but more localized convective circulation pattern, resulting in marine ice accretion at the top of the rift (*Khazendar and Jenkins, 2003*). Marine ice can also form where seawater laterally infiltrates firn prior to pore close-off (*Smith and Evans, 1972*), a process that likely occurs along the edges of rifts. Initially, basally accreted marine ice is likely permeable and slushy in appearance, but subsequently consolidates due to the subsequent accretion of new layers below and through conductive heat flux towards the ice shelf surface (*Craven et al., 2009*). Marine ice infills thin and potentially weak locations within ice shelves and provides a stabilizing cohesion between neighboring meteoric inputs to the ice shelf (*Holland et al., 2009; Glasser et al., 2009*).

Large-scale ice shelf fractures consist of rifts, which penetrate through the entire ice thickness and basal crevasses, which propagate upwards into the ice column from the ice-ocean interface but only reach heights of 30-60% of the total ice thickness (McGrath *et al.*, 2012). These fractures are frequently observed to terminate at suture zones, leading to much discussion about the mechanical properties of these zones (Rignot and MacAyeal, 1998; Fahnestock *et al.*, 2000; Larour *et al.*, 2004; Bassis *et al.*, 2007; Hulbe *et al.*, 2010). Prominent examples are the series of rifts (~25 km in length) that extend across Adie Inlet from Veier Head on Jason Peninsula to the suture zone originating from Churchill Peninsula (Figure 4.2). Both these rifts and the basal crevasses immediately to the south of the suture zone show no significant change in length between 1963 and present day

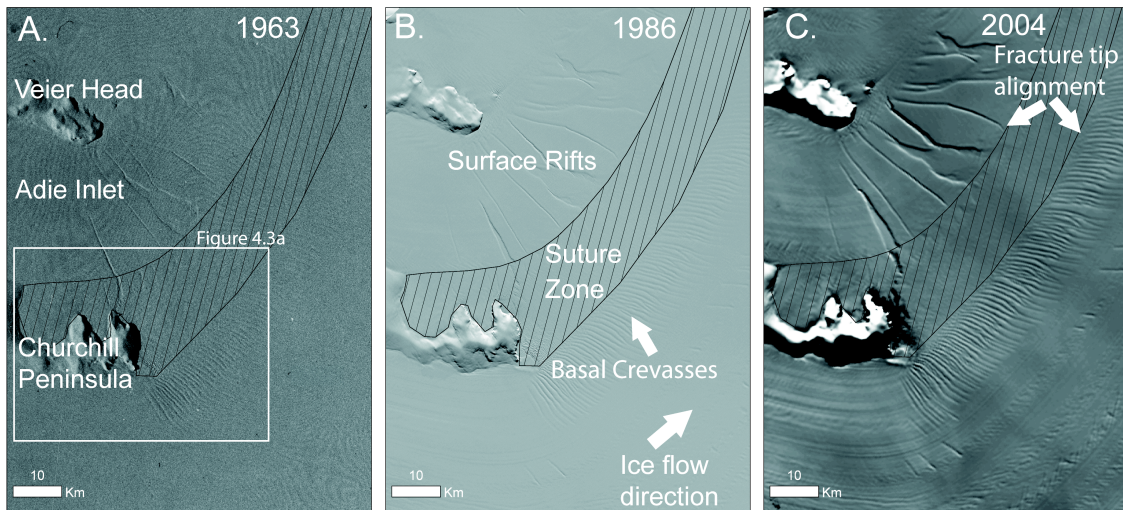


Figure 4.2. a) 1963 Declassified Intelligence Satellite Argon Photographic (DISP) image of Adie Inlet (Kim *et al.*, 2007). b) 1986 Landsat image of same region showing coherent and stable termination of fractures on suture zone downstream of Churchill Peninsula. c) 2003/04 MODIS MOA image showing continued stable fracture tip alignment.

(Figure 4.2). Similar behavior is exhibited by the rifts which propagate downstream of the Hollick-Kenyon Peninsula in the southern sector of Larsen C (*Glasser et al.*, 2009). Importantly, if they did not encounter the lateral heterogeneity of a suture zone, rifts would likely continue to propagate, potentially contributing to the formation of an iceberg (*Hulbe et al.*, 2010). This observation places considerable importance on understanding both this process and the material heterogeneity of these suture zones, which are consistently referred to in the literature as “softer” in reference to a lower inferred stiffness or flow law parameter (*Fahnestock et al.*, 2000; *Khazendar et al.*, 2007; 2011). The flow law parameter relates stress and strain in Glen’s flow law and is dependent on ice temperature, fabric, impurities and water content (*Cuffey and Patterson*, 2010), all of which are likely to differ in significant ways within suture zones.

Likely causes of the modified material properties in suture zones include the presence of: i) marine ice, which tends to be warmer (close to the freezing temperature of sea water) than meteoric ice that has been advected from the higher-elevation (and hence, colder) interior, ii) extensive crevassing/fracture, which can act to diffuse the stress intensity at the propagating fracture tip, iii) altered crystal fabric at the lateral edges of the meteoric ice (that form the bounds of the suture zones) due to past shear and iv) impurities. In contrast to previous work, recent laboratory deformation experiments of marine ice from the Nansen Ice Shelf, conducted in unconfined uniaxial compression, found that the samples were consistently “harder” than meteoric ice (*Dierckx and Tison*, 2013). This finding suggests that the temperature anomaly of marine ice may be the dominant factor in the modified material properties, rather than an inherent material difference.

Future predictions of sea-level rise are dependent on an improved understanding of ice shelf structure and processes, as nearly 75% of the ice flux from the Antarctic Ice Sheet occurs through ice shelves (*Bindschadler et al.*, 2011b). The rapid and catastrophic collapse of the Larsen A and B ice shelves led to extensive glacier front thinning and retreat (*Cook and Vaughan*, 2010; *Pritchard et al.*, 2009). Subsequent, and sustained, acceleration and thinning of outlet glaciers following the collapse of ice shelves has significantly increased ice discharge to the ocean and contributed to observed sea level rise (*Rignot et al.*, 2004; *Scambos et al.*, 2004; *Pritchard et al.*, 2009; *Berthier et al.*, 2012).

Larsen C is the largest ice shelf on the AP, consisting of over 50,000 km² of floating ice, which is fed from 12 major outlet glaciers flowing off the mountainous spine of the AP (Figure 4.1; *Cook and Vaughan*, 2010; *Glasser et al.*, 2009). The ice shelf thickness field is dominated by these major meteoric inflows, which exceed 1000 m at the grounding line but thin to ~200 m by the ice front, with a typical mid-shelf thickness between 250-400 m (*Griggs and Bamber*, 2009). Numerous promontories, such as Churchill and Cole Peninsulas, separate these meteoric inflows and extend 20-30 km into the ice shelf domain (Figure 4.3a,b). In some places, the ice-covered sections of the peninsula slope gradually towards the ice shelf, creating a smooth transition from grounded to floating ice (Figure 4.3c). Elsewhere, the transition is abrupt and the ice-shelf surface just downstream can be heavily fractured, although these fractures are not apparently open to

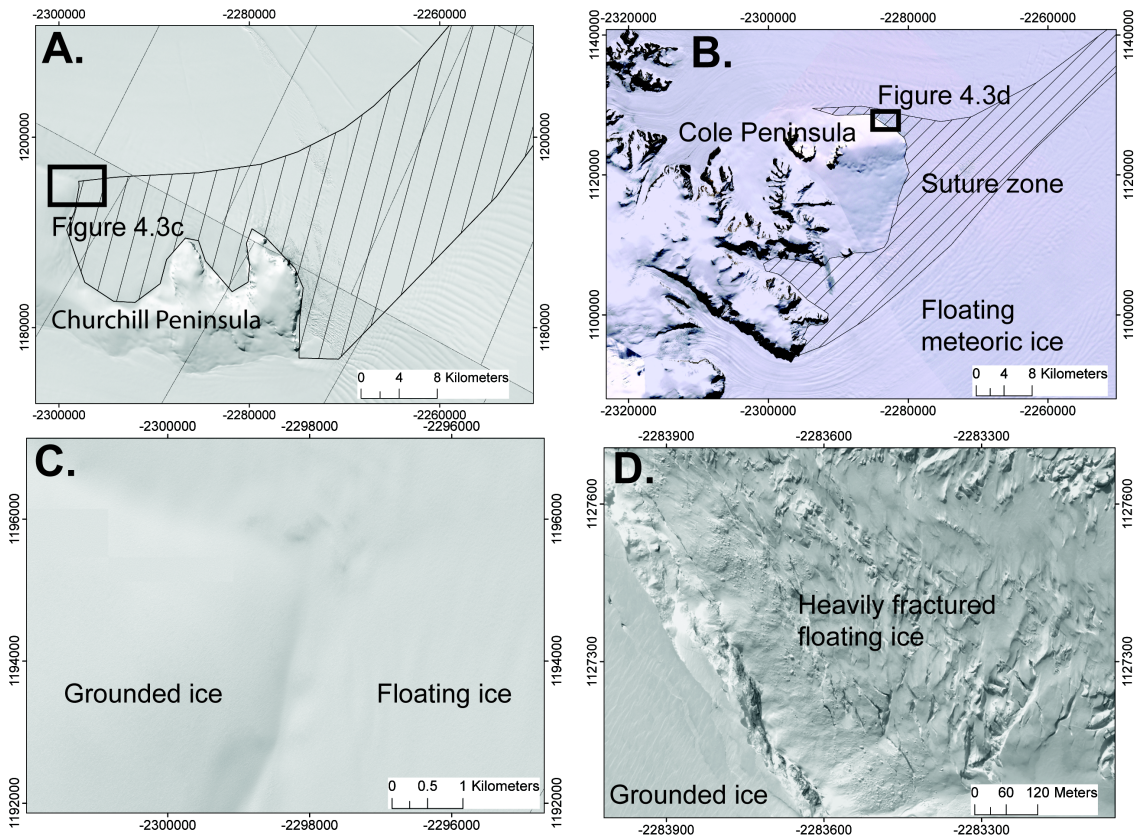


Figure 4.3. a) High-resolution (50 cm) visible imagery mosaic of Churchill Peninsula and suture zone. Location of Figure 4.3c is indicated by black box. b) Subset of the Landsat Imagery Mosaic of Antarctica (<http://lima.usgs.gov/>) detailing the suture zone downstream of Cole Peninsula. Location of Figure 4.3d is indicated by black box. c) A smooth transition from grounded to floating ice for a section of Churchill Peninsula (imagery from Oct. 2011). d) Abrupt transition from grounded ice on Cole Peninsula to heavily fractured floating ice (imagery Feb. 2012). Images in a,c,d are copyright Digital Globe, Inc., 2012.

sea level (Figure 4.3d). Numerous blocks ~10 m in dimensions and believed to be of meteoric origin are present in this proximal zone.

The extent of Larsen C has been relatively stable over the last five decades with the exception of calving events in 1986 and 2004/05 where the ice shelf lost $\sim 7700 \text{ km}^2$ and $\sim 1500 \text{ km}^2$, respectively (*Glasser et al.*, 2009; *Cook and Vaughan*, 2010). The latter calving event occurred after a rift propagated through the suture zone that can be traced downstream from Cole Peninsula (Figure 4.4). Numerous, large ($>20 \text{ km}$) rifts, originating at the calving front, were observed to terminate at the approximate lateral edges of this suture zone prior to the 2004-2005 calving event (Figure 4.4). Despite limited changes in extent, the surface elevation of Larsen C has lowered at a rate of between 0.06 ± 0.01 and $0.09 \pm 0.01 \text{ m a}^{-1}$ during the 1978-2008 period, with the greatest lowering occurring in the northern sector (*Shepherd et al.*, 2003; *Fricke and Padman*, 2012; *Pritchard et al.*, 2012). This surface lowering is likely dominated by firn densification driven by warmer air temperatures and increased meltwater production / refreezing (*Holland et al.*, 2011; *Fricke and Padman*, 2012; *Pritchard et al.*, 2012) rather than increased basal melting driven by an oceanic forcing (*Shepherd et al.*, 2003; *Nicholls et al.*, 2012). Oceanographic observations suggest that the primary water mass in the Larsen C cavity is High Salinity Shelf Water (HSSW), which has origins in Modified Weddell Deep Water, but has been cooled to the surface freezing point by wintertime sea ice production (*Nicholls et al.*, 2004; 2012). While HSSW has sufficient thermal forcing to drive weak basal melt, the rates are significantly lower than ice shelves whose cavities are filled with Circumpolar Deep Water (*Pritchard et al.*, 2012). Further, as HSSW is fixed to the surface freezing point, the only manner by which basal melt rates could increase is through the increased production and flux of HSSW through the cavity, which has not been observed (*Nicholls et al.*, 2012).

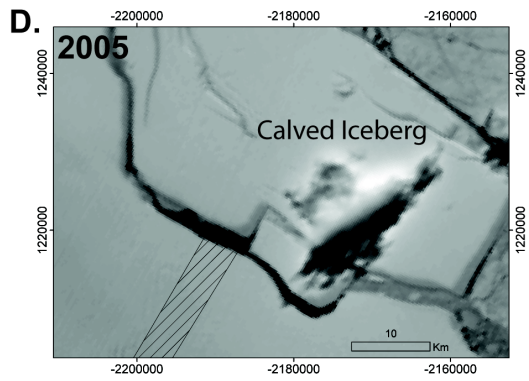
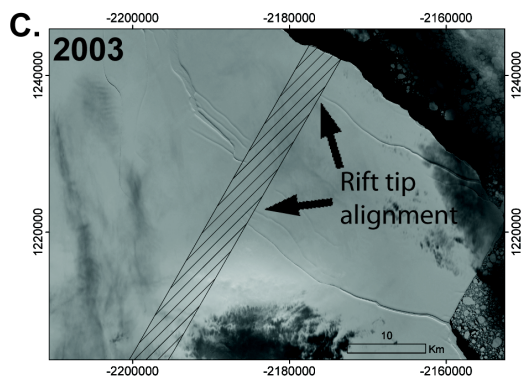
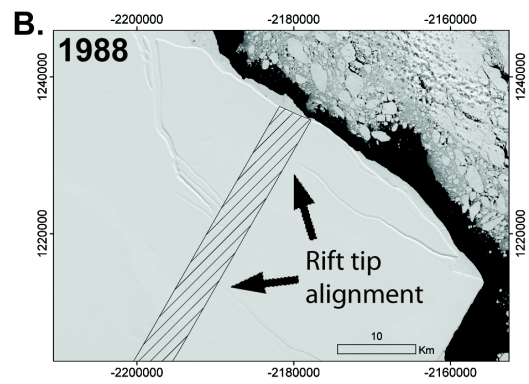
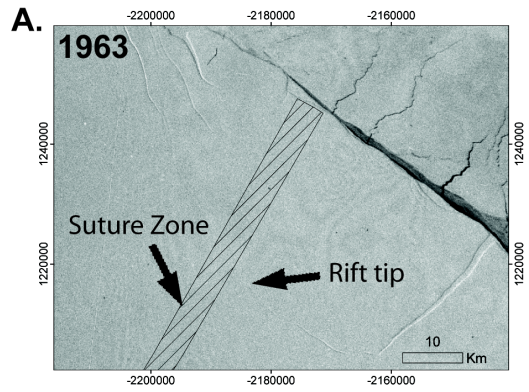


Figure 4.4. *a) DISP, (b-c) Landsat and d) MODIS imagery of Cole Peninsula suture zone at calving front. In 1963, the northerly propagating rift had reached the suture zone, where it remained stable through 2003, shown in panel (c). Numerous other rifts show coherent termination on either side of suture zone, while January 8, 2005 MODIS image shows recently calved ~1,500 km² iceberg.*

4.2 - Radar Survey

4.2.1 - Methods

Radar surveys were conducted with a Malå Geosciences ground based 25 MHz pulse radar system towed behind a snowmobile in November 2011. The radar data were processed by applying a dewow and bandpass filter, custom gain function and corrected for surface topography. The ice shelf-ocean interface reflection was manually delineated along the profiles by following the maximum amplitude in the radar waveform.

Simultaneous position data were collected with a Trimble GeoXH dual-channel GPS, which was post-processed and corrected to mean sea level using the Eigen GL06C geoid (Forste *et al.*, 2008), tidal amplitude using Circum-Antarctic Tidal Simulation version 2008a (CATS2008a), updated from Padman *et al.* (2002), and a dynamic ocean topography correction of 1.07 m (<http://grace.jpl.nasa.gov>; Tapley *et al.*, 2003). We estimate the error for the measured surface elevation to be ± 0.5 m. The measured two-way travel time and surface elevation were combined to derive the total ice-shelf (ice plus air) thickness using the methodology of Holland *et al.* (2011). This methodology produces spatially variable column-averaged densities, which are subsequently used to derive radar velocities, which range between 0.168-0.170 m ns⁻¹.

In areas with no basal reflector, an ‘equivalent meteoric ice thickness’ (H) was calculated based on measured surface elevations and the assumption of hydrostatic equilibrium. A local firm air correction, air , was derived by applying the methodology of *Holland et al.* (2011) to the areas of the relevant radar profile that do have a clear basal reflector. The ice thickness is then derived from:

$$H = \frac{(h-air)*\rho_w}{(\rho_w-\rho_i)} + air, \quad \text{Equation 4.1}$$

where h is the surface elevation above mean sea level, ρ_w is the density of sea water (1028 kg m⁻³), ρ_i is the density of ice (917 kg m⁻³). We estimate the relative error in the calculated ice thickness to be $\pm 14 \%$, which is the sum in quadrature of the individual errors in surface height (± 0.5 m), ice density (± 1 kg m⁻³), ocean water density (± 1 kg m⁻³) and the firm air correction (± 1.5 m).

We identify and delineate suture zones as the regions downstream of peninsulas, whose surface appears comparably smooth in visible satellite imagery (Figure 4.1). The lateral boundaries are defined by tracing surface lineations at the edge of the meteoric inflows to either side. As such, the suture zones, as drawn, are relatively wide features encompassing the entire domain downstream of the peninsulas, while the key material heterogeneities may be narrow, laterally discrete features within these domains.

4.2.2 - Radar observations

In situ radar observations were conducted perpendicular to the southern tip of a large rift in Adie Inlet, crossing both the active rift tip and the ice immediately to the south of rift termination (Figure 4.5). The surface expression of the rift is a concave trough

approximately 300 m wide and 10 m deep and was consistently bridged across the entire width. Radar observations show a strong, smooth basal reflector on either side of the rift, interpreted as the meteoric ice-ocean interface, and a strong, near horizontal reflector aligned with the trough minima and at an approximate depth of 5 m below sea level (Figure 4.5b). Continuous isochrones are observed in the upper 30 meters of the radargram and extend across the rift, consistent with layering within locally accumulated meteoric firn and ice. A second radar transect (Figure 4.5c), also perpendicular to the rift but ~3 km south (which corresponds to the direction of rift propagation) of the previous transect and 1.25 km beyond the last surface expression of the rift, was conducted in the suture zone (indicated by hatched region in Figure 4.5a). In contrast to the previous radar transect, there are no strong reflectors indicative of the ice-ocean interface. Instead, weak and mottled reflectors exist over a range of depths, first appearing in the ice column 140-185 m below the surface and extending for another 70-90 m (Figure 4.5c). The strength of the reflection varies over this thickness and there is no evidence of a distinct basal interface. Continuous isochrones in the upper 40 m are also observed along this transect, consistent with the presence of locally accumulated meteoric ice. The radar survey then exited the suture zone domain downstream of Churchill Peninsula and crossed back into Adie Inlet, which contains ice of meteoric origin. This final profile has a clear, strong basal reflection with no internal reflections below the coherent layering in the upper 40 m of firn (Figure 4.5d).

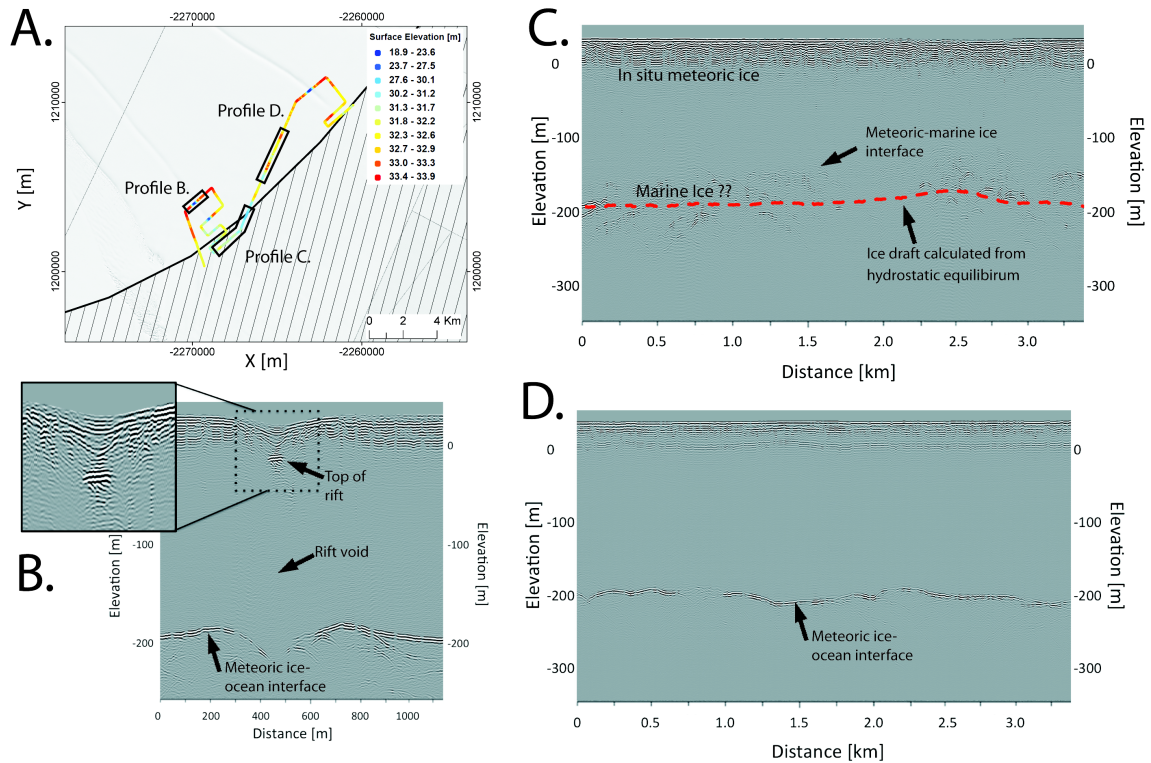


Figure 4.5. a) High-resolution visible imagery (Oct. 2011) of Adie Inlet fractures and Churchill Peninsula suture zone. Surface elevations from ground penetrating radar survey are overlaid. Locations of b-d are indicated by black boxes. b) Radargram crossing rift. c) Radargram in suture zone. d) Radargram showing clear meteoric ice-ocean interface after exiting suture zone domain. Panel a is copyright Digital Globe, Inc., 2012.

The initial interpretation of the radargram is as follows: in the suture zone, the lack of a strong basal return, and the presence of weak and mottled reflectors, which first emerge at ~140 m below the surface, is consistent with the presence of basally accreted marine ice. In the near surface, the strong, coherent layering is consistent with locally accumulated meteoric firn and ice. The emergence of a strong basal return at the end of the profile is consistent with the transect path, which exits the Churchill Peninsula suture

zone and crosses back into the meteoric origin Adie Inlet domain. If we assume the emergence of the weak internal reflectors corresponds to the meteoric-marine ice interface, then ~60 m of marine ice would exist to the depth of the calculated bottom, or ~70-90 m to the deepest of the weak, mottled reflectors.

We also sought to examine the temporal and spatial evolution of suture zone flowbands and thus, conducted a series of perpendicular radar transects at progressive distances along the suture zone originating at Cole Peninsula (Figure 4.6). Cole Peninsula protrudes ~30 km into the ice shelf domain and separates the thick meteoric inputs of Cabinet Inlet to the north and Mill Inlet to the south (Figure 4.3b), and resulting in the apparent ice thickness minima immediately downstream of the peninsula (Figure 4.6a). By tracing surface flow lines in satellite imagery, it is apparent that the significant meteoric land ice entering the shelf domain through both Cabinet and Mill Inlets rapidly compress the suture zone from a width of ~18 km to ~5 km over the first 40 km (Figure 4.6). We present radar transects at progressive distances (18, 52 and 131 km) from the grounding line, with the last profile being within 5 km of the current calving front.

Common features of these radargrams are discrete sections in the across-flow direction in which the basal return is obscured by a series of hyperbolae within the ice column. These hyperbolae, which are characteristic of sharp corner reflectors such as crevasses, scatter the radar energy, thereby precluding a return at greater depth. Outside of these sections, a basal return is observed, which becomes progressively cleaner/stronger in each subsequent profile in the along-flow direction. Importantly, and in contrast to the

Churchill Peninsula profiles, the hyperbolae occur initially at much shallower depths in the ice column but are observed progressively deeper in the along-flow direction.

In the first radar profile, which crosses the suture zone ~18 km from the grounding line, the ice shelf base is heavily fractured and thus, we calculate the total ice thickness using Eq. 4.1 to range between 248 to 275 m, with a mean of 255 ± 35 m. A series of hyperbolae, whose apices are at a depth of 50 to 90 m below the surface (the majority are ~55 m below the surface), obscure the basal return along the central ~1.25 km shown (Figure 4.6b). Outside of this section, a heavily fractured basal return is present.

Continuous or near-continuous isochrones are observed in the upper 40 m of the ice column. The next radar profile is 52 km from the grounding line and has similar characteristics to the first profile, in that there are continuous isochrones which extend for 60 m below the ice surface, and then a series of hyperbolae, whose apices range between 80 and 160 m below the surface, with the majority ~125 m below the surface (Figure 4.6c). The calculated mean ice thickness is 319 ± 45 m, which is 25% thicker than the previous transect. The final transect crosses the suture zone at a distance of 131 km from the grounding line and less than 5 km from the calving front. In this profile, a discrete ~700 m wide zone of internal hyperbolae, whose apices are at depths between 130-155 m, obscure the basal interface (Figure 4.6d). Outside of this zone, the basal interface has regions that are heavily fractured, although to a shallower depth than previous profiles, interspersed by a strong and smooth basal reflection. Outside of the transect shown, a strong and smooth basal reflection is dominant. The total mean ice thickness is 218 ± 31 m, a >30% reduction from the previous transect.

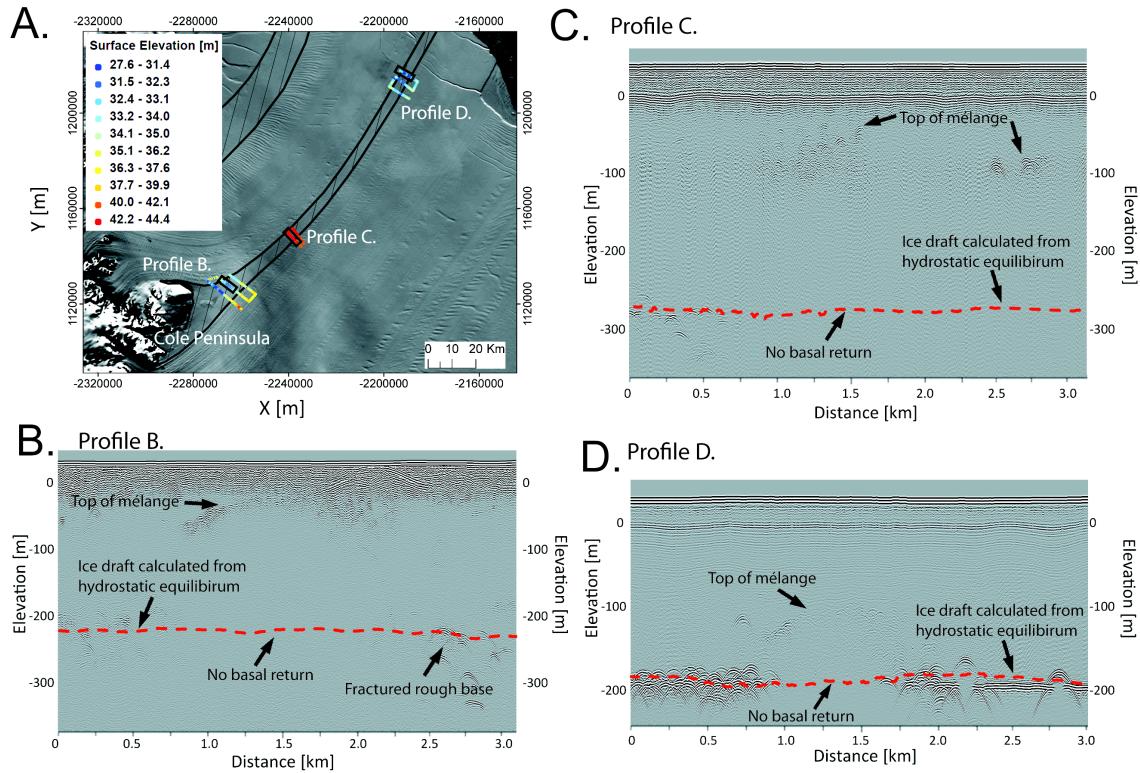


Figure 4.6. a) MOA image of the central Larsen C Ice Shelf and Cole Peninsula suture zone. Surface elevations from ground penetrating radar survey are overlaid. Black hatched regions indicate the Cole and Churchill Peninsula suture zones. Red dashed line in b-d is ice draft calculated from measured surface elevation and assumptions of hydrostatic equilibrium. Radargrams are shown crossing suture zone at b) 18 km, c) 52 km and d) 131 km from grounding line. The top of the mélange is identified by numerous hyperbolae in the radargrams, indicative of sharp, corner reflectors.

An initial interpretation is that the hyperbolae originate from the heavily fractured surface of the ice shelf in the wake of Cole Peninsula (Figure 4.3d), which is then progressively buried by locally accumulated meteoric accumulation while flowing towards the calving front. As the hyperbolae preclude a radar return at greater depth, no further information is

known about this section of the ice column, although the calculated ice thicknesses support the presence of ice beneath these features.

4.3 - Evolution of ice shelf structure

4.3.1 - Basal melting/freezing rates

In order to apply a flowline model to the suture zones studied above, we estimate the basal melting and freezing beneath Larsen C Ice Shelf using a mass flux divergence calculation. Mass conservation can be expressed by:

$$\frac{\partial \rho H}{\partial t} + \nabla \cdot (\rho V H) = \dot{a} - \dot{b}, \quad \text{Equation 4.2}$$

where H and ρ are the thickness and mean density of the ice column, V is the ice surface velocity vector, \dot{a} is the surface net mass accumulation rate and \dot{b} is the basal mass melting/freezing rate (positive is melting). We assume that the surface velocity represents the depth-average for a floating ice shelf (*Cuffey and Paterson, 2010*).

We proceed by assuming the ice-shelf mass is in steady state, $\partial \rho H / \partial t = 0$, which is justified on the basis that the observed surface lowering is likely due to densification, rather than mass removal (*Holland et al., 2011; Fricker and Padman, 2012; Pritchard et al., 2012*). Even if this interpretation of the recent lowering were incorrect, the rapid modern mass imbalance could not have been operating for a significant fraction of the long (~ 400 year) advective timescales of the flowline models used below, so the steady-state assumption is adequate for our purposes. In steady-state, the horizontal divergence of the mass flux is balanced by the sum of both the surface accumulation and basal melting/freezing contribution, and hence is expressed as:

$$\dot{b} = \dot{a} - \nabla \cdot (\rho \mathbf{V}H).$$

Equation 4.3

The datasets used in this analysis include: (i) ice thickness and density calculated from: surface elevations from satellite radar altimetry (*Griggs and Bamber, 2009*), a derived firn-air grid (*Holland et al., 2011*), and the assumption of hydrostatic equilibrium, (ii) InSAR derived ice velocities from the MEaSURES project (*Rignot et al., 2011*), and (iii) surface mass balance from the RACMO2.1/Ant model (*Lenaerts et al., 2012*). All datasets were compiled to a common reference frame with 1-km grid cells in a polar stereographic projection, allowing us to derive the steady-state basal melting/freezing rates from Eq. 4.3 on that grid. We estimate the relative error in basal melting/freezing rates to be $\pm 20\%$, which represents the sum in quadrature of the individual relative errors in ice thickness (± 43 m), ice velocity (± 4 m yr⁻¹), surface mass balance (± 6.7 cm eq. yr⁻¹), and column-averaged density (± 3 kg m⁻³).

The nominal resolution of the source data are considerably coarser than the 1-km grid, and the method uses spatial derivatives, so the resulting melting/freezing field contains a high level of noise, even after smoothing with 9 * 9 km filter (Figure 4.7). For example, the wave-like pattern downstream of Adie Inlet is clearly an artifact due to the advection of large rifts; highly accurate and coincident ice thickness and velocity fields would be needed to realistically calculate the mass divergence in the presence of these topographic features, and their treatment as a continuum is questionable. Nevertheless, the derived field does produce a good agreement with previous studies. The method reproduces a modeled pattern of melting beneath deep grounding lines and refreezing in suture zones

(Holland *et al.*, 2009), with a particularly vigorous refreezing off Churchill Peninsula that Holland *et al.* (2009) propose to be due to a major confluence of meltwater plumes. In addition, the areas of rapid melting near Bawden Ice Rise and along the Hollick-Kenyon Peninsula agree with predictions of strong tidally driven melting in those areas (Mueller *et al.*, 2012). Finally, the calculated rate of $0.9 \pm 0.2 \text{ m yr}^{-1}$ agrees well with a direct observation of $1.3 \pm 0.2 \text{ m yr}^{-1}$ melting in the Hollick-Kenyon peninsula region (Nicholls *et al.*, 2012).

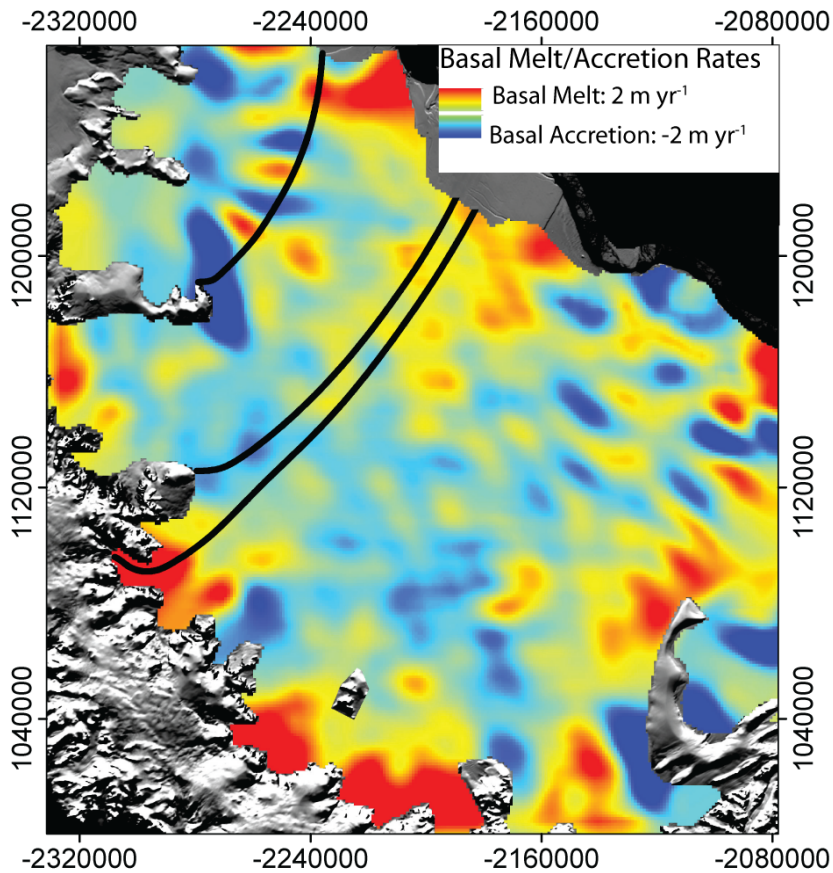


Figure 4.7. Steady-state field of basal melt/accretion rates for the Larsen C Ice Shelf. Basal melting is positive and basal accretion is negative. The flowline cross-sections shown in Figure 4.8 are indicated by black lines. Mass is reported as meters of water equivalent (1000 kg m^{-3}).

4.3.2 - Along-flow evolution

We now consider the evolution of ice structure along flowlines originating at the grounding lines of both Cole and Churchill Peninsula, and Mill Inlet (Figure 4.7). The ice is conceived to be comprised of three layers: a surface ‘locally accumulated meteoric ice’ layer built up by mean surface mass balance rates from the RACMO2.1/Ant model (*Lenaerts et al.*, 2012), a ‘basally accreted marine ice’ layer according to the basal melting/freezing field described above, and an ‘interior ice’ layer occupying the remainder of the ice column, whose origin is discussed later.

Instantaneous mass flux rates are first converted to cumulative thickness, on a node-by-node basis, by multiplying these rates by the time increment for this ice column to pass between nodes. We convert surface accumulation mass to thickness by applying an offset proportional to the firn air volume over this ice thickness (*Holland et al.*, 2011). We convert marine ice mass to thickness assuming an average density of 935 kg m^{-3} , a value higher than meteoric ice due to the presence of seawater in the permeable lower layers of the marine ice (*Craven et al.*, 2009). This cumulative thickness at each node is added to the cumulative thickness of the surface and basal layers that exist on the upstream edge of each node.

However, to apply this technique to the flowline cross-section it is necessary to account for strain thinning. As the surface velocity is constant with depth for a floating ice shelf, we can assume that each of the layers undergo the same rate of thinning per unit depth.

The vertical strain rate ($\dot{\epsilon}_z$), is related to the variation in along-stream and transverse flow, and can be calculated as:

$$\dot{\epsilon}_z = -(\dot{\epsilon}_x + \dot{\epsilon}_y), \quad \text{Equation 4.4}$$

where $\dot{\epsilon}_x$ is the along-flow strain rate and $\dot{\epsilon}_y$ is the transverse strain rate. The along-flow and transverse strain rates are calculated from the InSAR surface velocities (*Rignot et al., 2011*). Applying the formulation of *Craven et al. (2009)*, we calculate the thickness of both the surface accumulation and basally accreted marine ice layer at the downstream edge of the node (Z_2) compared to its thickness at the upstream edge (Z_1) as:

$$Z_2 = Z_1 * e^{\dot{\epsilon}_z \cdot t} + \frac{\dot{a}}{\dot{\epsilon}_z} (e^{\dot{\epsilon}_z \cdot t} - 1), \quad \text{Equation 4.5}$$

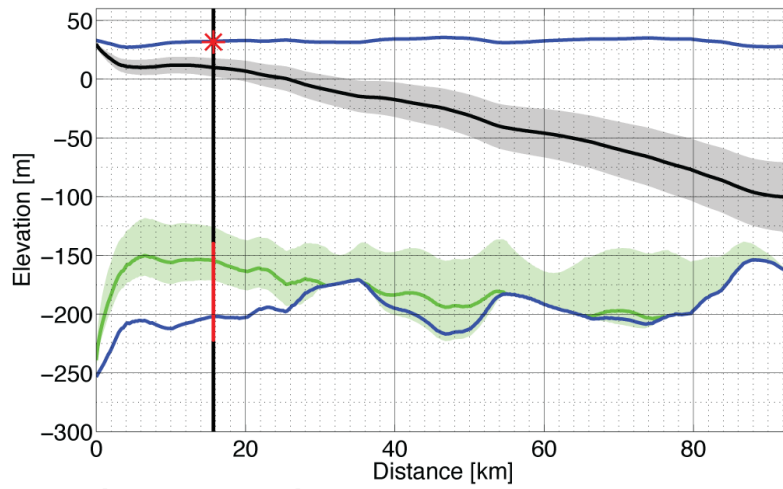
where t is the time taken to advect between nodes and \dot{a} , is representative of the instantaneous rate of mass flux, either at the surface or base of the ice shelf. We assess the sensitivity of the flowline model to a range of key parameters, including surface velocity (manifested as time to advect between nodes), the vertical strain rate and both surface and basal melting/freezing rates. The shaded bounds (Figure 4.8) represent the cumulative sensitivity of the locally accumulated meteoric ice and basally accreted marine ice layers to $\pm 20\%$ surface velocity, $\pm 20\%$ vertical strain rate and $\pm 20\%$ for surface/basal mass flux rates.

The flowline cross sections shown in Figure 4.8 delineate the along flow evolution of the internal structure of the Larsen C Ice Shelf. Surface accumulation forms the upper wedge of the ice shelf and comes to constitute $68 \pm 16\%$, $49 \pm 14\%$, $64 \pm 24\%$ of the total thickness near the calving front along the Churchill, Cole and Mill flowlines, respectively (Figure 4.8). Basally accreted marine ice is present along both the Churchill and Cole

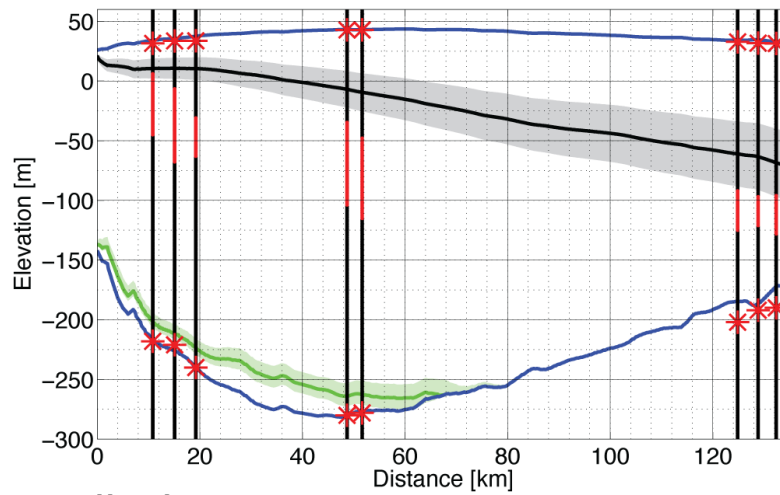
Peninsulas, but not along the meteoric inflow dominated Mill Inlet, which instead experiences high basal melt rates. Importantly, the basally accreted marine ice layers, which reach maximum thicknesses of 56 ± 25 and 26 ± 9 m for Churchill and Cole, respectively, are subsequently melted away and do not persist to the calving front along either profile (Figure 4.8). However, it is important to realize that this model only represents marine ice accretion that occurs on a scale large enough to affect the coarse ice-thickness and velocity fields and cannot capture the small-scale processes discussed previously, such as the local production of marine ice in rifts or flooding of firm (*Khazendar and Jenkins, 2003*). Thus, the model likely underestimates the actual thickness of marine ice. It is also important to note the caveats associated with the basal melting/freezing field, particularly with respect to Churchill Peninsula (see above).

Thin vertical black lines in Figure 4.8 correspond to the along-flow distances of the radar transects, over which are laid red stars corresponding to observed surface elevations and either observed/calculated ice drafts. The red vertical lines correspond to the observed depths of the specific features discussed previously and shown in Figures 4.5 and 4.6. *In situ* GPS observations confirm the overall thickness profiles (root-mean-square (RMS) error of 15 m), and in particular, the large-scale thickening that occurs along the Cole Peninsula profile. The thickness of the accumulation wedge (difference between upper blue and black lines) along the modeled Cole Peninsula flowline (Figure 4.8b) agrees with the radar observations of increasing along-flow thickness (RMS error of 29 m), although there is a systematic negative offset. A plausible explanation for this offset is the preferential, above-average accumulation that occurs in surface depressions due to

A. Churchill Peninsula



B. Cole Peninsula



C. Mill Inlet

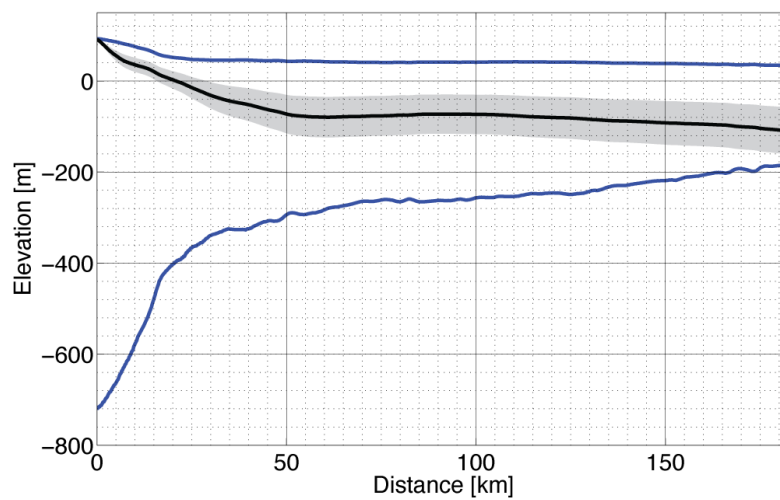


Figure 4.8. *Flowline cross-sections of the Larsen C Ice Shelf along a) Churchill Peninsula, b) Cole Peninsula and c) Mill Inlet. Surface elevation (blue), ice draft (blue), and interfaces between locally accumulated meteoric ice and interior ice (black) and basally accreted marine ice (green) are shown. The shaded bounds represent the cumulative sensitivity of the model to parameters as discussed in the text. Thin vertical black lines correspond to radar transects, while overlaid red vertical lines indicate depths of features discussed in the text and shown in Figure 4.5 and 4.6. Red stars are measured surface elevations and either observed/calculated drafts. Note different elevation and distance scales.*

wind re-deposition (Leonard *et al.*, 2008) but is not represented in the RACMO2.1/Ant model. A second explanation could be that the modeled 1979-2011 mean surface mass balance values underestimate the ~400 year mean values integrated along this flowline, which is consistent with the notion that increased atmospheric flow over the Antarctic Peninsula, associated with the positive polarity of the Southern Annular Mode index, has led to drier, warmer air over Larsen Ice Shelf (Marshall *et al.*, 2006). An additional explanation for this offset could be that the source of the radar return originates from sea level at the grounding line, rather than from the ice shelf surface, since this would uniformly lower the interface by 25-30 m. A sea-level origin would be appropriate if the return were from firn that had been flooded with seawater, or from sea ice and marine ice formed in open rifts.

Along Cole Peninsula, the flowline model agrees with the initial radar interpretation, in that the internal hyperbolae likely originate from the heavily fractured surface of the ice

shelf, or potentially, from sea level, but not from large-scale basally accreted marine ice. In contrast, the Churchill Peninsula model suggests that at a distance of 17-19 km, corresponding to the radar profile shown in Figure 4.5c, ~45 m of basally accreted marine ice exists. This supports the initial radar interpretation that the weak, mottled reflectors, first observed within the ice column at a depth of 140 m below the surface are in fact the meteoric-marine ice interface, and that reflectors below this depth likely originate from within the basally accreted marine ice layer. The interface between the locally accumulated meteoric layer and the interior layer, which dominates the Cole Peninsula profile, is not apparent here. This is likely the result of the smooth grounding line transition that exists for this section of Churchill Peninsula (Figure 4.3c).

4.4 - Discussion

The along-flow evolution of the ice shelf structure, and the importance of the locally accumulated meteoric layer for maintaining the ice shelf thickness, is apparent in all three flowlines. Near the calving front this wedge of ice accounts for ~60 % of the total ice thickness. Importantly, as this ice has accumulated on the ice-shelf surface, it is unlikely that large lateral variations exist in the mechanical properties, regardless of whether it accumulated on a suture zone or meteoric inflow. Thus, if we return to the time series of satellite images leading up to and just after the 2004/05 calving event for Larsen C, it is apparent how significant the remaining ~40 % of the ice column is for ice-shelf stability.

In the 1963 image, three distinct rifts are seen propagating south towards the suture zone, while a front parallel rift is propagating northwards. In all cases, these rifts are present in

ice of meteoric origin, comparable to the flowline model for Mill Inlet (Figure 4.8c). In both the 1988 and 2003 image numerous rifts are observed to have terminated and stabilized at the approximate lateral edges of the suture zone. It is important to note that while the suture zones have been drawn as relatively wide features encompassing the entire domain downstream of the peninsulas, the key material heterogeneities are likely narrow, laterally discrete features, as observed in the calving front radargram (Figure 4.6d) and thus, the rifts may partially extend into the suture zones as they have been delineated. The subsequent image (Figure 4.4d) on January 8, 2005 clearly shows a detached iceberg, the result of the northward propagating rift eventually penetrating through the suture zone. There is no evidence for what reinitiated rift propagation, although the role of the suture zone in delaying the calving of this iceberg is apparent. This in turn highlights the role of heterogeneity in a minority of the ice thickness, since it is unlikely that the upper 60% of the ice column with homogenous mechanical properties would be responsible for this delay.

The Cole Peninsula radar observations are dominated by discrete widths of heavily fractured ice that obscure a basal return, outside of which the basal return progresses from heavily fractured to smooth between the sequential along-flow radar transects. Ice thickness calculations, assuming hydrostatic equilibrium, confirm the presence of ice beneath this layer, although the results from the integrated mass conservation model suggest that whatever thickness of basally accreted marine ice that may have formed closer to the grounding line has subsequently been melted away, more than 50 km from the modern calving front (which roughly coincides with the northward propagating rift

that resulted in the 2004/05 iceberg calving). As noted previously, this interpretation is based solely on the large-scale mass conservation model, which does not have the ability to capture small-scale processes such as the local production of marine ice in rifts (*Khazendar and Jenkins, 2003*), and therefore likely underestimates the marine ice thickness in these locations. In contrast to the mass-conservation model, the radar observations suggest that the ice mélange that forms in the wake of the peninsula, and therefore likely contains marine ice produced through small-scale processes, persists to the calving front.

The Churchill Peninsula profile offers an interesting comparison to Cole Peninsula, since both the interpreted radargrams (i.e. mottled reflectors at depth in Figure 4.5c) and flowline model (i.e. green line in Figure 4.8b) suggest the presence of >40 m of marine ice at the point of rift termination in the suture zone. However, the large-scale mass conservation model suggests that marine ice only persists continuously for another ~15 km downstream, although we do not have radar observations to confirm this result and the basal mass balance calculations are particularly questionable in this area (Figure 4.7). We note, however, that the rifts (Figure 4.2) remain bound by the lateral edge of the suture zone all the way to the calving front. Similar stagnant behavior is observed for the series of rifts originating from the Hollick-Kenyon Peninsula in the southern sector of Larsen C, which do not penetrate the suture-zone ice from Joerg Peninsula (Figure 4.9; *Glasser et al., 2009; Jansen et al., 2010*). Such static behavior may simply be due to spatial variation in the stress environment: rifts are opened due to tension next to the peninsulas and bound by the marine ice there, but as they are advected downstream the

tension relaxes, so that they don't subsequently propagate regardless of any change in the suture-zone ice structure. Alternatively, some property of the suture-zone ice remains sufficiently different from the meteoric band to counteract any tension further downstream. The flowline model suggests that the locally accumulated meteoric layer reaches ~68% of the total thickness, with the remainder of the ice column consisting of 'interior ice.'

The presence of interior ice, between the overlying locally accumulated meteoric wedge and the basally accreted marine ice layer, is persistent in both suture zone flowlines. Our observations do not clarify the origin of this interior ice, although a number of possibilities exist. First, as discussed previously, it is likely that higher localized accumulation rates exist in the wake of peninsulas due to wind re-deposition in these surface troughs, resulting in a greater thickness of the locally accumulated meteoric ice layer and less interior ice. Second, the large-scale mass conservation model likely underestimates basal accretion rates in the immediate wake of the peninsula, due to both local processes (individual rift-scale marine ice production) and uncertainty in the model inputs (specifically ice thickness and surface velocity) near the grounding line. If the ice-thickness gradient were greater in reality than it is in the model, higher basal accretion rates would exist immediately downstream of the peninsula. This would result in a thicker basally accreted marine ice layer and less interior ice. Additionally, while peninsulas certainly limit the flux of grounded ice into suture zone domains (i.e. no major outlet glaciers), there remain extensive regions where slow moving grounded meteoric ice flows into the shelf, as observed on both Churchill and Cole Peninsulas (Figure 4.3).

Finally, any remaining interior ice may also be sourced by lateral flow convergence around the peninsula, which will be affected by the detail of velocity and ice thickness fields in this region. We conclude that a proportion of the interior ice in these profiles likely consists of marine ice produced from local sources, and therefore, marine ice may well persist to the calving front in these narrow bands, in agreement with the missing basal reflectors in *Holland et al. (2009)*.

An additional line of anecdotal evidence supporting the notion that marine ice persists in suture zones further than the large-scale mass balance model suggests is seen in Figure 4.9. Two large tributaries of Mobiloil Inlet join together ~10 km upstream of the grounding line, creating a distinct surface lineation that can be traced along-flow on the floating ice shelf (Figure 4.9). The series of large rifts / fractures that propagate northward from the eastern tip of the Hollick-Kenyon Peninsula are clearly observed to propagate through this suture zone. These rifts, however, coherently terminate along a second suture zone, which is known to contain marine ice (*Holland et al., 2009*; D. Jansen, pers. comm. 2013). This observation, while not conclusive, emphasizes that the presence of marine ice is likely the key component responsible for rift termination, rather than mechanical properties inherent to all suture zones and thus, supports the persistence of marine ice to the calving front.

From our observations of both the Churchill and Cole Peninsula suture zones, it is apparent that a small section of the ice thickness can have a proportionally outsized affect on rift termination, and subsequently, the structural stability of ice shelves. This material

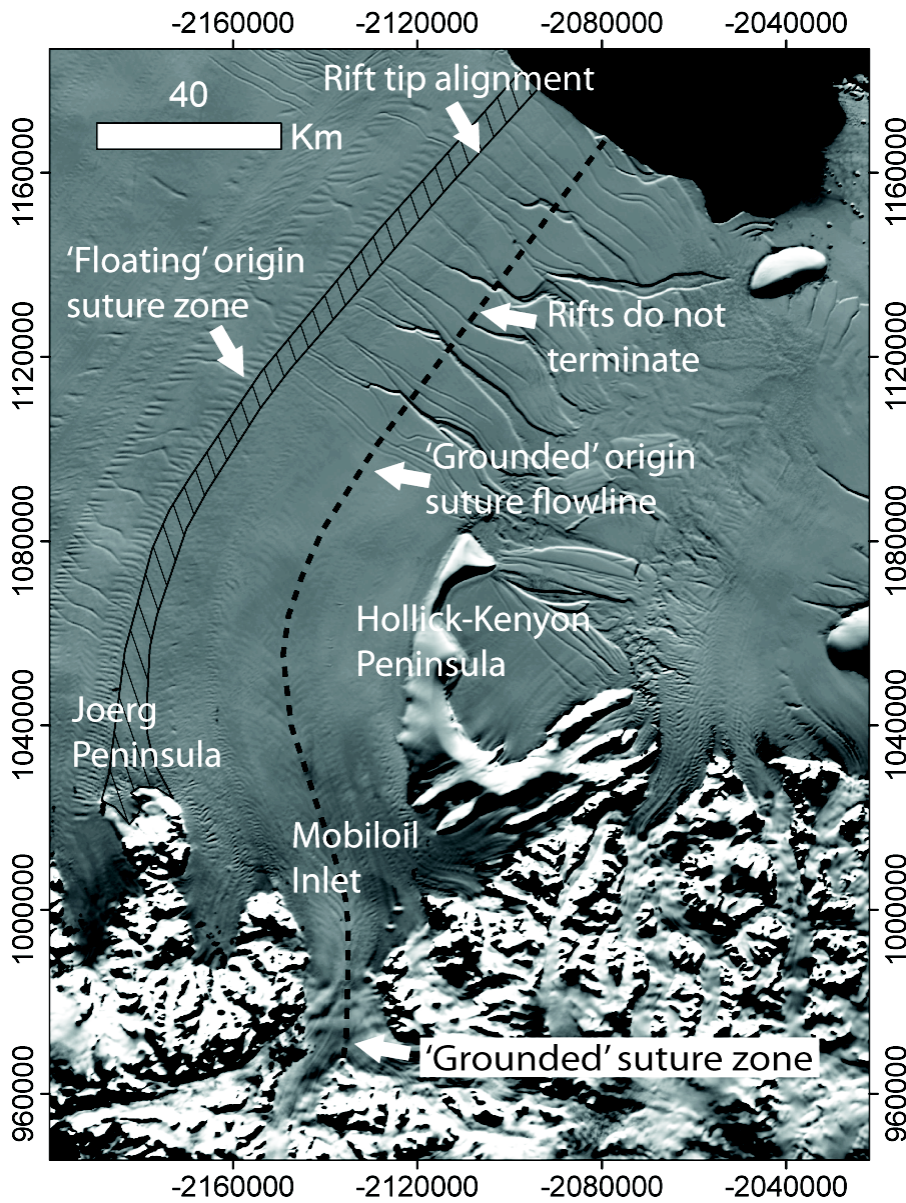


Figure 4.9. MOA image of the southern sector of the Larsen C Ice Shelf detailing the suture zone that forms in the wake of Joerg Peninsula, which contains marine ice, and the suture zone that forms in a grounded section of Mobiloil Inlet, which does not contain marine ice. Rifts, propagating off the tip of the Hollick-Kenyon Peninsula, extend through the suture zone with grounded origins but coherently terminate along the lateral edge of the Joerg Peninsula suture zone.

heterogeneity likely comes from a combination of marine ice and the presence of fracture. In the absence of the heterogeneity in these zones, the continued propagation of fractures would result in a greatly weakened ice shelf and likely contribute to increased tabular iceberg calving. Ultimately this increased calving could threaten the stability of the ice shelf. For example, if the large fractures / rifts that currently terminate in the Churchill and Joerg suture zones were allowed to propagate toward each other, the eastward half of Larsen C, unconstrained by sidewalls, would appear unviable (Figure 4.1). This is an important, and non-linear, sensitivity of ice shelves to oceanic forcings, for if either the rate of basal accretion decreases or basal melt increases, such features, located at the base of the ice shelf, would likely be removed.

This sensitivity is further exacerbated because a significant proportion of the fractures on the Larsen C Ice Shelf are initially not full-thickness rifts, but rather basal crevasses and therefore likely only penetrate through 40-60% of the ice thickness (Figure 4.10; *McGrath et al.*, 2012). The lack of full-thickness penetration of the basal crevasses emphasizes the importance of the mechanical properties of the lower half of the ice shelf, as this would likely have the greatest control over whether the fractures continue to propagate or terminate. The series of fractures near the calving front Whirlwind Inlet domain (Figure 4.1), which are bound on either side by suture zones, appear as broad surface troughs in visible imagery, consistent with their interpretation as basal crevasses (Figure 4.10b). For comparison, a crosscutting, front-perpendicular full-thickness rift (with considerable mélange infill) is also shown, which is a notably sharper feature and represents a structural discontinuity within the shelf (Figure 4.10c). As basal crevasses

propagate through approximately the lower 50% of the ice column, they would likely be far more sensitive to the mechanical properties present in this section of the ice column.

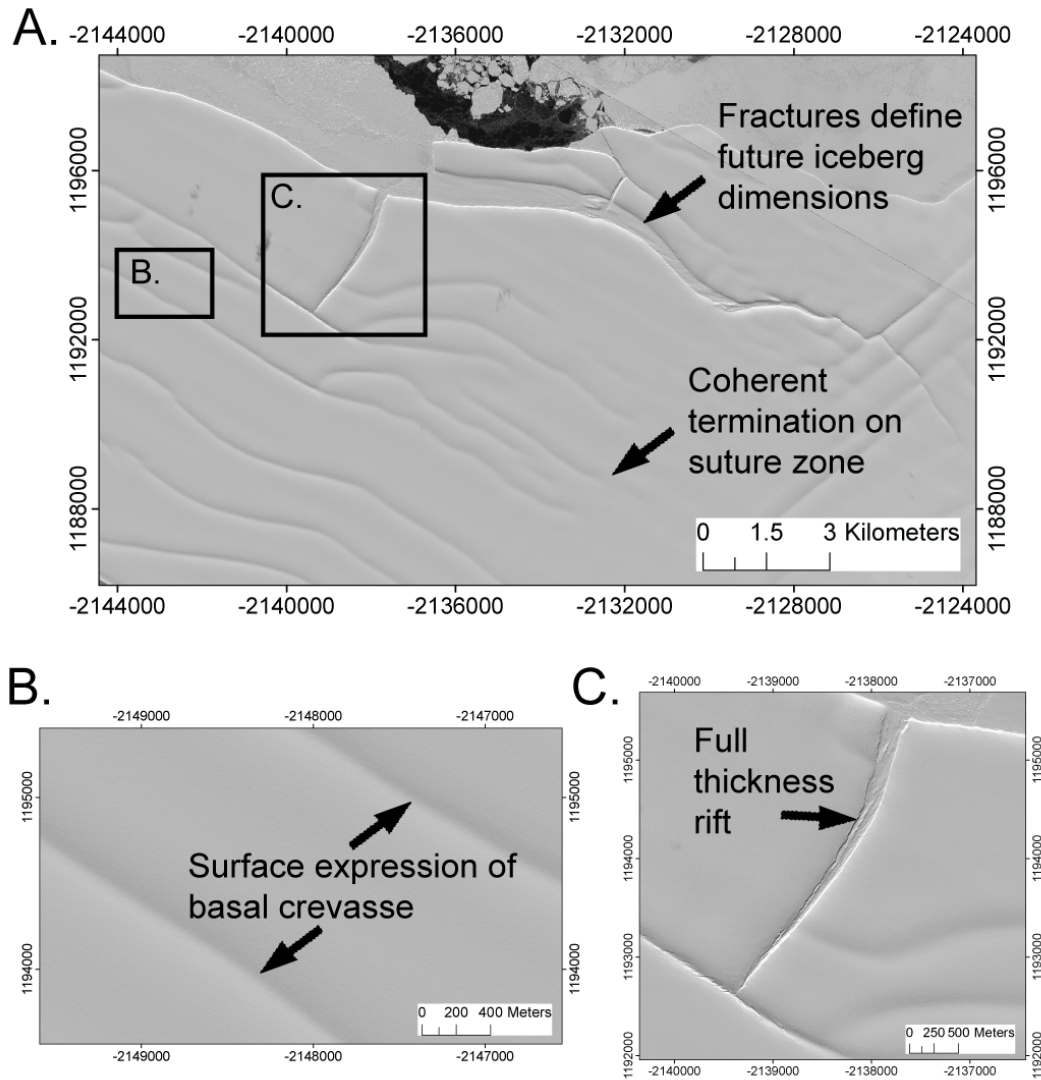


Figure 4.10. *a) High-resolution visible imagery (Nov. 2009) of the calving front in the region of ice originating in Whirlwind Inlet, which contains b) numerous basal crevasses, as indicated by the surface troughs, and c) an ice mélange filled full thickness rift.*

Imagery copyright GeoEye Inc., 2011.

4.5 - Conclusions

In situ radar observations and visible imagery are used to demonstrate that material heterogeneity, such as the presence of marine ice or fracture, limit rift propagation on the Larsen C Ice Shelf. A large 25 km-long rift terminates at the suture zone originating downstream of Churchill Peninsula. Radar surveys demonstrate the presence of ~60 m of marine ice within the suture zone at the point of rift termination. The along-flow evolution of the suture zone downstream of Cole Peninsula demonstrates that the growing wedge of *in situ* accumulation, with likely homogenous material properties, comes to account for ~60 % of the total ice thickness. The implications of this are twofold: i) the remaining heterogeneity is sufficient, even as a minority of the total thickness, to arrest rift propagation and ii) this represents an important sensitivity of ice shelves, as changes in ocean forcings may erode these features, thereby allowing basal crevasses and rifts to propagate earlier, likely increasing tabular iceberg calving rates and ultimately determining the stability of the ice shelf.

Acknowledgments

This work is funded by NSF OPP research grant 0732946. The British Antarctic Survey and field assistant, Tom Weston, provided exceptional field support, without which this work would not have been possible. Geospatial support for this work was supported by the Polar Geospatial Center under NSF OPP agreement ANT-1043681. We thank Jan Lenaerts and Michael van den Broeke for the RACMO2.1/Ant surface mass balance data, and Jenny Griggs and Jonathan Bamber for the surface elevation data.

Chapter 5

Summary and Future Directions

5.1 - Summary

Atmospheric warming of ~ 2.5 °C over the last half-century (*Turner et al.*, 2005), and concurrent environmental changes, including a dramatic decline in sea ice extent, widespread tidewater glacier retreat and acceleration, and the disintegration of numerous ice shelves totaling over 28,000 km² has made the AP one of the fastest changing locations on the planet (*Parkinson and Cavalieri*, 2012; *Pritchard and Vaughan*, 2007; *Cook and Vaughan*, 2010). The subsequent, and sustained, acceleration and dynamical thinning of the outlet glaciers following the collapse of floating ice shelves has increased the AP's contribution to observed sea level rise (*Scambos et al.*, 2004; *Pritchard et al.*, 2011; *Berthier et al.*, 2012). As nearly 75% of the ice flux from the Antarctic Ice Sheet occurs through ice shelves ringing the continent, these observations amplify the importance of understanding ice shelf stability in order to make meaningful predictions of future sea level rise (*Bindschadler et al.*, 2011b). This thesis sought to contribute to this understanding, by examining certain structural aspects of ice shelves, in an effort to understand how these features may affect, both as a hindrance to and reinforcement of, ice shelf stability in a warming climate.

Chapter 2 examines a series of basal crevasses that form in the vicinity of Churchill Peninsula and are subsequently advected towards the calving front. While basal crevasses have been observed on numerous ice shelves, even as early as the mid-1960s in airborne radio-echo sounding surveys, this study provides the first detailed observations of their

size, along-flow evolution, and importantly, the subsequent surface structures that form. The basal crevasses first form due to increased along-flow strain rates as the ice exits Cabinet Inlet and joins the main body of the ice shelf. An along-flow 30 km ground penetrating radar survey found the basal crevasses to initially penetrate between 120-134 m or the equivalent of ~45% of the total ice thickness. Over the survey length, the basal crevasses decrease in height by ~40 m, reaching an equivalent penetration height of 25%. The opening of the basal crevasses at the base of the ice shelf is also observed to evolve along-flow, increasing from ~100 m to more than 200 m. Along the survey, surface troughs, 3-4 m in depth, were observed above the apices of the basal crevasses.

High-resolution visible satellite imagery illustrates that closer to the origin of the basal crevasses the surface trough amplitude is likely much larger, and the combined impact of two neighboring basal crevasses creates a surface crest, with large (8-24 m width) surface crevasses aligned parallel to these features. Combining these observations, I hypothesize that the formation of a basal crevasse causes the ice shelf surface layers to vertically shear in order to re-establish hydrostatic equilibrium. The downwarped surface firm layers in the radargram are evidence of this process (Figure 2.2). However, this column of ice remains partially supported by beam stresses of the full-thickness ice columns on either side, which gives rise to bending stresses that result in the along-flow widening of the basal crevasses. This hypothesis is further supported by visible imagery, which shows a pronounced increase in the along-flow direction of both the amplitude of the surface troughs and the number and width of the surface crevasses along the crests, which are related to the increased vertical shear and bending stresses, respectively.

Following the observations presented in Chapter 2, subsequent field seasons on Larsen C were directed, amongst other goals, at examining basal crevasses in greater detail, including a 100 km along-flow transect that extended the profile collected in 2008 to near the calving front, and a focused effort, on an isolated but larger basal crevasse in the Cabinet Inlet outflow. This basal crevasse extends 4.5 km in length and reaches a height of 233 m above the ice shelf base, or the equivalent of 66% of the mean local ice thickness. In this chapter, additional support is provided for the hypothesis presented in Chapter 2, in the form of radar surveys near the origin of the basal crevasses, and an elastic bending beam model, which examines the surface deformation and stress distribution for an idealized floating ice shelf perturbed by a basal crevasse like weakness. Radar surveys completed in the area upstream of the basal crevasses described in Chapter 2 (in the vicinity of Churchill Peninsula) show two large basal crevasses (~300 m tall), although, the ice shelf surface does not reflect their full presence, as there is only a low-amplitude surface trough and no apparent surface crevassing. This supports the notion that basal crevasses form first, and that the surface features form subsequently, as the ice shelf column seeks to return to hydrostatic balance. Second, the elastic bending beam model supports the stress distribution and the magnitude of the surface deformation observed in the field. The modeled stress distribution shows a coherent pattern of extensional stresses at the surface crests and compression in the surface troughs, consistent with the observed locations of surface crevasses. Further, the magnitude of the stress at the crests exceeds the fracture toughness of ice, suggesting that the surface deformation and subsequent bending stresses drive the formation of the surface crevasses. Lastly, high-resolution visible imagery illustrates the relative abundance of basal

crevasses on other ice shelves around Antarctica, including the Getz and Amery. It is shown that basal crevasses likely existed on the Larsen B Ice Shelf prior to its breakup and may have played an important role during the disintegration process.

Chapter 4 examines the structure and along-flow evolution of two suture zones in the Larsen C Ice Shelf in order to gain a better understanding of how these features result in rift termination, and therefore, contribute to ice shelf stability. Ground penetrating radar surveys demonstrate that a large rift propagating through meteoric ice in Adie Inlet terminates in the Churchill Peninsula suture zone, which is found to have ~60 m of basally accreted marine ice. A steady-state field of basal melting and freezing is determined, and applied to a flowline model to delineate the along-flow evolution of layers within the ice shelf, which, importantly, comes to be dominated by a thickening wedge of locally accumulated meteoric ice. However, the ice mélange, which accounts for <40% of the total ice thickness near the calving front, is responsible for delaying the propagation of rifts and therefore tabular calving events. A time series of satellite images show rifts propagating towards and terminating on the Cole Peninsula suture zone for more than 40 years prior to one rift penetrating through, thereby calving the most recent major iceberg from Larsen C. This work demonstrates that material heterogeneity in a minority of the ice thickness can limit rift propagation, but similarly, suggests that this property of ice shelf stability is highly sensitive to oceanic forcings that may lead to the loss of these features.

5.2 - Future Directions

Understanding ice shelf stability is paramount to making useful predictions of the Antarctic Ice Sheet's contribution to sea level rise over the coming century. The structural features examined in this thesis are deserving of continued and enhanced study, considering the control ice shelf stability has over future sea level contributions. In particular, an increased understanding of suture zone structure and composition, and how this varies both spatially for an individual ice shelf and around the continent is essential. In addition, it is necessary to understand the temporal evolution of these features in response to changing environmental forcings.

Specific approaches to this research include:

i) A series of ice cores extracted from a suture zone, such as that originating from Cole Peninsula, to elucidate the composition of the ice shelf structure. Quantifying the thickness of the basally accreted marine ice layer proximal to the suture zone is key to estimating basal accretion rates in this region, which is likely not well represented in large-scale mass conservation models.

ii) Installation of an instrument package in the water column beneath the ice shelf measuring both the water properties and changes to the basal ice-ocean interface, using an upward looking sonar.

iii) Additional cores within suture zones in the vicinity of rift termination, with those located in either Adie Inlet or originating off the Hollick-Kenyon Peninsula being good targets to determine the composition of the ice column where the rifts terminate.

iv) Further laboratory experiments to examine and quantify the material properties of marine ice.

v) The ongoing NASA IceBridge airborne mission has collected extensive datasets covering a number of ice shelves both on the peninsula and in the Amundsen Sea sector. The combination of altimetry and a number of radar products can be utilized to map the structure of suture zones on these shelves. This work could be combined with the mass conservation-flowline models used in Chapter 4 to elucidate the structure of numerous ice shelves around the continent and to explore the influence of contrasting climate regimes on the evolution of this structure.

A second area of continued research should focus on basal crevasses and their subsequent impact on a number of important ice shelf processes. A linear elastic fracture mechanics model was applied in Chapter 2 to examine the sensitivity of propagation height to a series of parameters, including strain rate, ice temperature and ice thickness. The importance in understanding how these parameters affect basal crevasse propagation is amplified by the observation in Chapter 4 that a vast majority of fractures in the Larsen C Ice Shelf are actually basal crevasses and not full-thickness rifts. However, either prior to or during a calving event these basal crevasses fracture through the full-thickness of the ice shelf; a process deserving of further attention. Lastly, it was hypothesized in Chapter 3 that meltwater would likely pond in the surface depressions overlying basal crevasses, and if this water reached a sufficient volume, it could contribute to the hydrofracture of an initial flaw in the depression or by intersecting a fracture on the flank of a surface crest. These processes could be examined in greater detail with an integrated flow and fracture

model similar to that applied by *Jansen et al.* (2010) to examine how the presence of these large-scale fractures affect ice shelf stability.

Lastly, it would be remiss to examine the structural components of ice shelves without considering how changes in atmospheric and oceanic forcings may affect these features in the future, and hence, their influence on ice shelf stability. As an illustration, consider that the basal crevasses examined in Chapter 2 have likely existed for more than 400 years without causing the ice shelf to disintegrate, and likewise, the suture zones throughout the ice shelf continue to arrest propagating rifts despite changing environmental forcings. Thus, a key area of research needs to assess how changing environmental forcings will affect these features. For example, quantifying future meltwater production is a necessary first step in considering how basal crevasse-induced surface troughs will control the ponding of this meltwater. Likewise, future estimates of basal mass balance forced with large-scale ocean models are necessary in order to assess whether suture zones will remain effective at arresting rift propagation despite a potentially modified composition.

An overarching goal of this research remains in deciphering and understanding the different forcings that led to the dramatic warming in the second half of the 20th century, and importantly, understanding how these forcings will affect the climate of this region in the coming decades. Atmospheric variability over the past decade (discussed in Chapter 1) has rendered many of these trends to be no longer statistically significant, despite the SAM index remaining positive throughout this period (*Barrand et al.*, 2013). This

amplifies the recent evidence that the climate of West Antarctica, and perhaps the peninsula as well, is driven by variability in Pacific tropical sea surface temperatures (*Ding et al.*, 2011). Thus, many important questions remain in understanding the forcings and connections driving AP climate.

A tractable aspect, and one with direct implications for ice shelf stability, is to understand the spatial and temporal variability of föhn air flow over the peninsula. Föhn flow causes high surface temperatures on the lee side of the peninsula, resulting in increased meltwater production on the surface of Larsen C. This process likely contributed to the formation of melt ponds on Larsen B prior to its disintegration (*van den Broeke*, 2005). It has been recognized that the air content of Larsen C, which is inversely related to melt duration, is strongly influenced by föhn flow (i.e. longitudinal gradient overlaid on strong latitudinal gradient; *Holland et al.*, 2011). One approach for Larsen C is to identify significant melt events (i.e. large increases in melt extent over days) in either the passive microwave or scatterometer datasets and examine these events through a combination of meteorological observations and atmospheric re-analysis products to elucidate the connection between föhn flow and meltwater production on the ice shelf. Quantifying the role of föhn flow as a percentage of total melt on the ice shelf would be one key result. A second result would be the quantification of the distance from the peninsula over which föhn flow can affect surface melt (boundary layer mixing typically limits the reach of such events).

References

- Arblaster, J.M. and G.A. Meehl (2006), Contributions of external forcings to Southern Annual Mode trends, *J. Climate*, **19**, 2896-2905.
- Barrand, N.E., D.G. Vaughan, N. Steiner, M. Tedesco, P. Kuipers Munneke, M.R. van den Broeke and J.S. Hosking (2013), Trends in Antarctic Peninsula surface melting conditions from observations and regional climate modeling, *J. Geophys. Res.*, **118**, doi:10.1029/2012JF002559.
- Bassis, J.N., H.A. Fricker, R. Coleman, Y. Bock, J. Behrens, D. Darnell, M. Okal, and J.-B. Minster (2007), Seismicity and deformation associated with ice-shelf rift propagation, *J. Glaciol.*, **53**(183), 523-536.
- Bassis, J.N. and C.C. Walker (2012), Upper and lower limits on the stability of calving glaciers from the yield strength envelope of ice, *Proc. R. Soc. A*, **468**, 913-931, doi: 10.1098/rspa.2011.0422.
- Bentley, C.R., J.W. Clough, K. Jezek and S. Shabtaie (1979), Ice-thickness patterns and the dynamics of the Ross Ice Shelf, Antarctica, *J. Glaciol.*, **24**(90), 287-294.
- Berthier, E., T. Scambos and C. Shuman (2012), Mass loss of Larsen B tributary glaciers (Antarctic Peninsula) unabated since 2002, *Geophys. Res. Lett.*, **39**, L13501, doi:10.1029/2012GL051755.
- Bindschadler, R., D.G. Vaughan and P. Vornberger (2011a), Variability of basal melt beneath the Pine Island Glacier ice shelf, West Antarctica, *J. Glaciol.*, **57**(204), 581-595.
- Bindschadler, R., H. Choi, A. Wichlacz, R. Bingham, J. Bohlander, K. Brunt, H. Corr, R. Drews, H. Fricker, M. Hall, R. Hindmarsh, J. Kohler, L. Padman, W. Rack, G. Rotschky, S. Urbini, P. Vornberger and N. Young (2011b), Getting around Antarctica: new high-resolution mappings of the grounded and freely-floating boundaries of the Antarctic ice sheet created from the International Polar Year, *The Cryosphere*, **5**, 569-588, doi:10.5194/tc-5-569-2011.
- Braun, M., A. Humbert and A. Moll (2009), Changes of Wilkins Ice Shelf over the past 15 years and inferences on its stability, *The Cryosphere*, **3**, 41-56.
- Burton, J.C., J.M. Amundson, D.S. Abbot, A. Boghosian, L.M. Cathles, S. Correa-Legisios, K.N. Darnell, N. Guttenberg, D.M. Holland and D.R. MacAyeal (2012), Laboratory investigations of iceberg capsize dynamics, energy dissipation and tsunamigenesis, *J. Geophys. Res.*, **117**, F01007, doi:10.1029/2011JF002055.
- Casassa, G. and I.M. Whillans (1994), Decay of surface topography on the Ross Ice Shelf, Antarctica, *Ann. Glaciol.*, **20**, 249-253.

- Chen, J.L., C.R. Wilson, D. Blankenship and B.D. Tapley (2009), Accelerated Antarctic ice loss from satellite gravity measurements, *Nat. Geosci.*, **2**(12), 859-862.
- Clark, P.U., A.S. Dyke, J.D. Shakun, A.E. Carlson, J. Clark, B. Wohlfarth, J.X. Mitrovica, S.W. Hostetler and A.M. McCabe (2009), The Last Glacial Maximum, *Science*, **325**, 710-714, doi:10.1126/science.1172873.
- Colling, A. (2001), *Ocean Circulation*, Butterworth-Heinemann, Oxford, 286 p.
- Cook, A.J., A.J. Fox, D.G. Vaughan and J.G. Ferrigno (2005), Retreating glacier fronts on the Antarctic Peninsula over the past half-century, *Science*, **308**, doi:10.1126/science.1104235.
- Cook, A.J. and D.G. Vaughan (2010), Overview of areal changes of the ice shelves on the Antarctic Peninsula over the past 50 years, *The Cryosphere*, **4**, 77-98.
- Craven, M., I. Allison, H.A. Fricker and R. Warner (2009), Properties of a marine ice layer under the Amery Ice Shelf, East Antarctica, *J. Glaciol.*, **55**(192), 717-728.
- Cuffey, K.M. and W.S.B. Pateron (2010), *The Physics of Glaciers*, fourth edition, Oxford, Butterworth-Heinemann, 693 p.
- Dahl-Jensen et al. (2012), Eemian interglacial reconstructed from a Greenland folded ice core, *Nature*, **493**, 489-494, doi:10.1038/nature11789.
- Das, S., I. Joughin, M.D. Behn, I.M. Howat, M.A. King, D. Lizarralde and M.P. Bhattia (2008), Fracture propagation to the base of the Greenland Ice Sheet during supraglacial lake drainage, *Science*, **320**, 778-781, doi:10.1126/science.1153360.
- Dierckx, M. and J-L. Tison (2013), Marine ice deformation experiments: an empirical validation of creep parameters, *Geophys. Res. Lett.*, **40**, 134-138, doi:10.1029/2012GL054197.
- Ding, Q., E. Steig, D. Battisti and M. Kuttel (2011), Winter warming in West Antarctica caused by central tropical Pacific warming, *Nat. Geosci.*, **4**, 398-403, doi:10.1038/NGEO1129.
- Doake, C.S.M., H.F.J. Corr, H. Rott, P. Skvarca and N.W. Young (1998), Breakup and conditions for stability of the northern Larsen Ice Shelf, Antarctica, *Nature*, **391**, 778-780.
- Domack, E., D. Duran, A. Leventer, S. Ishman, S. Doane, S. McCallum, D. Amblas, J. Ring, R. Gilbert and M. Prentice (2005), Stability of the Larsen B ice shelf on the Antarctic Peninsula during the Holocene epoch, *Nature*, **436**(4), 681-685, doi:10.1038/nature03908.

Fahnestock, M.A., T.A. Scambos, R.A. Bindschadler and G. Kvaran (2000), A millenium of variable ice flow recorded by the Ross Ice Shelf, Antarctica, *J. Glaciol.*, **46**(155), 652-664.

Fahnestock, M. A., W. Abdalati and C. A. Shuman (2002), Long melt seasons on ice shelves of the Antarctic Peninsula: an analysis using satellite-based microwave emission measurements, *Ann. Glaciol.*, **34**, 127-133.

Fahrbach, E., M. Hoppema, G. Rohardt, M. Schroder and A. Wisotzki (2004), Decadal-scale variations of water mass properties in the deep Weddell Sea, *Ocean Dynamics*, **54**, 77-91.

Fleet, M. (1965), Occurrence of rifts in the Larsen Ice Shelf near Cape Dissapointment, *Brit. Antarct. Surv. Bull.*, 63-66.

Förste, C., R. Schmidt, R. Stubenvoll, F. Flechtner, U. Mery, R. König, H. Neumayer, R. Biancale, J-M. Lemoine, S. Bruinsma, S. Loyer, F. Barthelmes and S. Esselborn (2008), The GeoForschungsZentrum Potsdam/Groupe de Recherche de Geodesie Spatiale satellite-only and combined gravity field models: EIGEN-GL04S1 and EIGEN-GL04C, *J. Geod.*, **82**, 331–346, doi: 10.1007/s00190-007-0183-8.

Fountain, A.G., R.W. Jacobel, R. Schilchting and P. Jansson (2005), Fractures as the main pathways of water flow in temperate glaciers, *Nature*, **433**, 618-621.

Fricker, H.A. and L. Padman (2012), Thirty years of elevation change on Antarctic Peninsula ice shelves from multitmission satellite radar altimetry, *J. Geophys. Res.*, **117**, C02026, doi:10.1029/2011JC007126.

Gilbert, R. and E.W. Domack (2003), Sedimentary record of disintegrating ice shelves in a warming climate, Antarctic Peninsula, *Geochem. Geophys. Geosys.*, **4**(4), doi:10.1029/2002GC000441.

Gille, S. (2002), Warming of the Southern Ocean since the 1950s, *Science*, **295**, 1275-1277, doi:10.1126/science.1065863.

Glasser, N.F. and T.A. Scambos (2008), A structural glaciological analysis of the 2002 Larsen B ice shelf collapse, *J. Glaciol.*, **54**(184), 3-16.

Glasser, N.F., B. Kulesa, A. Luckman, D. Jansen, E.C. King, P.R. Sammonds, T.A. Scambos and K.C. Jezek (2009), Surface structure and stability of the Larsen C ice shelf, Antarctic Peninsula, *J. Glaciol.*, **55**(191), 400-410.

Gong, D. and S. Wang (1999), Definition of Antarctic oscillation index, *Geophys. Res. Lett.*, **26**, 459-462.

Griggs, J.A. and J.L. Bamber (2009), Ice shelf thickness over Larsen C, Antarctica, derived from satellite altimetry, *Geophys. Res. Lett.*, **36**, L19501, doi:10.1029/2009GL039527.

- Guttenberg, N., D.S. Abbot, J.M. Amundson, J.C. Burton, L. Mac Cathles, D.R. MacAyeal and W.W. Zhang (2011), A computational investigation of iceberg capsize as a driver of explosive ice shelf disintegration, *Ann. Glaciol.*, **52**(59), 51-59.
- Haran, T., J. Bohlander, T. Scambos, T. Painter and M. Fahnestock (2005), updated 2006, *MODIS mosaic of Antarctica (MOA) image map*. Boulder, Colorado USA: National Snow and Ice Data Center, digital media.
- Hodgson, D.A. (2011), First synchronous retreat of ice shelves marks a new phase of polar deglaciation, *Proc. Natl. Acad. Sci.*, **108**(47), 18859-18860, doi:10.1073/pnas.1116515108.
- Holland, P.R., H.F.J. Corr, D.G. Vaughan, A. Jenkins and P. Skvarca (2009), Marine ice in Larsen Ice Shelf. *Geophys. Res. Lett.*, **36**, doi:10.1029/2009gl038162.
- Holland, P.R., H.F.J. Corr, H.D. Pritchard, D.G. Vaughan, R.J. Arthern, A. Jenkins and M. Tedesco (2011), The air content of Larsen Ice Shelf, *Geophys. Res. Lett.*, **38**, doi:10.1029/2011GL047245.
- Hulbe, C.L., C. LeDoux and K. Cruikshank (2010), Propagation of long fractures in the Ronne Ice Shelf, Antarctica, investigated using a numerical model of fracture propagation, *J. Glaciol.*, **56**(197), 459-472.
- Humbert, A. and D. Steinhage (2011), The evolution of the western rift area of the Fimbul Ice Shelf, Antarctica, *The Cryosphere*, **5**, 931-944, doi:10.5194/tc-5-931-2011.
- Ivins, E.R., M.M. Watkins, D-N. Yuan, R. Dietrich, G. Casassa and A. Rulke (2011), On-land ice loss and glacial isostatic adjustment at the Drake Passage: 2003-2009, *J. Geophys. Res.*, **116**, B02403, doi:10.1029/2010JB007607.
- Jacobs, S. (2006), Observations of change in the Southern Ocean, *Phil. Trans. R. Soc. A.* **364**, 1657-168, doi:10.1098/rsta.2006.1794.
- Jacobs, S.S., A. Jenkins, C.F. Giulivi and P. Dutrieux (2011), Strong ocean circulation and increased melting beneath Pine Island Glacier ice shelf, *Nat. Geosci.*, **4**, 519-523, doi:10.1038/ngeo1188.
- Jansen, D., B. Kulesa, P.R. Sammonds, A. Luckman, E.C. King and N.F. Glasser (2010), Present stability of the Larsen C ice shelf, Antarctic Peninsula, *J. Glaciol.*, **56**(198), 593-600.
- Jenkins, A., H.F.J. Corr, K.W. Nicholls, C.L. Stewart and C.S.M. Doake (2006), Interactions between ice and ocean observed with phase-sensitive radar near an Antarctica ice-shelf grounding line, *J. Glaciol.*, **52**(78), 325-346.

Jenkins, A., P. Dutrieux, S.S. Jacobs, S.D. McPhail, J.R. Perrett, A.T. Webb and D. White (2010), Observations beneath Pine Island Glacier in West Antarctica and implications for its retreat, *Nat. Geosci.*, **3**, 468-472, doi:10.1038/NGEO890.

Jezek, K.C., C.R. Bentley and J.W. Clough (1979), Electromagnetic sounding of bottom crevasses on the Ross Ice Shelf, Antarctica, *J. Glaciol.*, **24**(90), 321-330.

Jezek, K.C. (1984), A modified theory of bottom crevasses used as a means for measuring the buttressing effect of ice shelves on inland ice sheets, *J. Geophys. Res.*, **89**, 1925-1931.

Johnston, T.L. and E.R. Parker (1957), Preliminary investigation of surface effects in flow and fracture. *Sixteenth technical report*, **27**(16), Mineral Research Lab., U.

Kim, K., K.C. Jezek and H. Liu (2007), Orthorectified image mosaic of Antarctica from 1963 Argon satellite photography: image processing and glaciological applications, *Intern. J. Remote Sens.*, **28**(23), 5357-5373.

King, J. C., and J. Turner (1997), *Antarctic Meteorology and Climatology*, Cambridge Univ. Press, New York.

King, J.C. and J.C. Comiso (2003), The spatial coherence of interannual temperature variations in the Antarctic Peninsula, *Geophys. Res. Lett.*, **30**(2), doi:10.1029/2002GL015580.

Khazendar, A. and A. Jenkins (2003), A model of marine ice formation within Antarctic ice shelf rifts, *J. Geophys. Res.*, **108**(C7), doi:10.1029/2002JC001673.

Khazendar, A., E. Rignot and E. Larour (2007), Larsen B Ice Shelf rheology preceding its disintegration inferred by a control method, *Geophys. Res. Lett.*, **34**, doi:10.1029/2007GL030980.

Khazendar, A., E. Rignot and E. Larour (2011), Acceleration and spatial rheology of Larsen C Ice Shelf, Antarctic Peninsula, *Geophys. Res. Lett.*, **38**, doi:10.1029/2011GL046775.

Kwok, R. and J. C. Comiso (2002), Spatial patterns of variability in Antarctic surface temperature: Connections to the Southern Hemisphere Annular Mode and the Southern Oscillation, *Geophys. Res. Lett.*, **29**, 1705-1708.

Lambrecht, A., H. Sandhäger, D.G. Vaughan and C. Mayer (2007), New ice thickness maps of Filchner-Ronne Ice Shelf, Antarctica, with specific focus on grounding lines and marine ice, *Ant. Science*, **19**(4), 521-532, doi:10.1017/S0954102007000661.

Larour, E., E. Rignot and D. Aubry (2004), Modelling of rift propagation on Ronne Ice Shelf, Antarctica, and sensitivity to climate change, *Geophys. Res. Lett.*, **31**, L16404, doi:10.1029/2004GL020077.

- Leonard, K.C., L.-B. Tremblay, D.R. MacAyeal and S.S. Jacobs (2008), Interactions of wind-transported snow with a rift in the Ross Ice Shelf, Antarctica, *Geophys. Res. Lett.*, **35**, L05501, doi:10.1029/2007GL033005.
- Lenaerts, J.T.M., M.R. van den Broeke, W.J. van de Berg, E. van Meijgaard and P. Kuipers Munneke (2012), A new, high-resolution surface mass balance map of Antarctica (1979-2010) based on regional atmospheric climate modeling, *Geophys. Res. Lett.*, **39**, L04501, doi:10.1029/2011GL050713.
- Luckman, A., D. Jansen, B. Kulesa, E.C. King, P. Sammonds and D.I. Benn (2012), Basal crevasses in Larsen C Ice Shelf and implications for their global abundance, *The Cryosphere*, **6**, 113-123, doi:10.5194/tc-6-113-2012.
- MacAyeal, D.R., T.A. Scambos, C. Hulbe and M. Fahnestock (2003), Catastrophic ice-shelf break-up by an ice-shelf-fragment-capsize mechanism, *J. Glaciol.*, **49**(164), 22-36.
- MacGregor, J.A., G.A. Catania, M.S. Markowski and A.G. Andrews (2012), Widespread rifting and retreat of ice-shelf margins in the eastern Amundsen Sea Embayment between 1972 and 2011, *J. Glaciol.*, **58**(209), 458-466, doi:10.3189/2012JoG11J262.
- Marshall, G.J. (2002), Analysis of recent circulation and thermal advection change in the northern Antarctic Peninsula, *Int. J. Climatol.*, **22**, 1557-1567.
- Marshall, G. J. (2003), Trends in the Southern Annular Mode from observations and reanalysis, *J. Clim.*, **16**, 4134-4143.
- Marshall, G.J., A. Orr, N.P.M. van Lipzig and J.C. King (2006), The impact of a changing Southern Hemisphere Annular Mode on Antarctic Peninsula summer temperatures, *J. Climate*, **19**, 5388-5404.
- Marshall, G.J. (2007), Short Communication: Half-century seasonal relationships between the Southern Annular Mode and Antarctic temperatures, *Int. J. Clim.*, **27**, 373-383, doi:10.1002/joc.1407.
- Martinson, D.G. (2011), Antarctic circumpolar current's role in the Antarctic ice system: An overview, *Palaeogeog., Palaeoclim., Palaeoecol.*, **335-336**, 71-74, doi:10.1016/j.palaeo.2011.04.007.
- Mason, D. (1950), The Larsen Shelf Ice, *J. Glaciol.*, **1**(8), 409-413.
- Massom, S.E. Stammerjohn, W. Lefebvre, S.A. Harangozo, N. Adams, T. Scambos, M. Pook and C. Fowler (2008), West Antarctic Peninsula sea ice in 2005: Extreme ice compaction and ice edge retreat due to strong anomaly with respect to climate. *J. Geophys. Res.*, **113**, C02S20, doi:10.1029/2007JC004239.

- McGrath, D., K. Steffen, T. Scambos, H. Rajaram, G. Casassa and J.L. Rodriguez Lagos (2012), Basal crevasses and associated surface crevassing on the Larsen C ice shelf, Antarctica, and their role in ice-shelf instability, *Ann. Glaciol.*, **58**(60), doi:10.3189/2012AoG60A005.
- Meredith, M.P. and J.C. King (2005), Rapid climate change in the ocean west of the Antarctic Peninsula during the second half of the 20th century, *Geophys. Res. Lett.*, **32**, L19604, doi:10.1029/2005GL024042.
- Monaghan, A.J., D.H. Bromwich, W. Chapman and J.C. Comiso (2008), Recent variability and trends of Antarctic near-surface temperature, *J. Geophys. Res.*, **113**, D04105, doi:10.1029/2007JD009094.
- Morris, E.M. and D.G. Vaughan (2003), Spatial and temporal variation of surface temperature on the Antarctic Peninsula and the limit of viability of ice shelves, *Antarctic Peninsula Climate Variability*, Ant. Res. Series, **79**, 61-68.
- Mueller, R.D., L. Padman, M.S. Dinniman, S.Y. Erofeeva, H.A. Fricker and M.A. King (2012), Impact of tide-topography interactions on basal melting of Larsen C Ice Shelf, Antarctica, *J. of Geophys. Res.*, **117**, C05005, doi:10.1029/2011JC007263.
- Mulvaney, R., N.J. Abram, R.C.A. Hindmarsh, C. Arrowsmith, L. Fleet, J. Triest, L.C. Sime, O. Alemany and S. Foord (2012), Recent Antarctic Peninsula warming relative to Holocene climate and ice-shelf history, *Nature*, **489**, 141-145, doi:10.1038/nature11391.
- Muto, A., T.A. Scambos, K. Steffen, A.G. Slater and G.D. Clow (2011), Recent surface temperature trends in the interior of East Antarctica from borehole firn temperature measurements and geophysical inverse methods, *Geophys. Res. Lett.*, **38**, L15502, doi:10.1029/2011GL048086.
- Nicholls, K.W., C.J. Pudsey and P. Morris (2004), Summertime water masses off the northern Larsen C Ice Shelf, Antarctica. *Geophys. Res. Lett.*, **31**, doi:10.1029/2004GL019924.
- Nicholls, K.W., K. Makinson and E.J. Venables (2012), Ocean circulation beneath Larsen C Ice Shelf, Antarctica from in situ observations, *Geophys. Res. Lett.*, **39**, L19608, doi:10.1029/2012GL053187.
- Orheim, O. (1982), Radio echo-sounding of Riiser-Larsenisen, *Ann. Glaciol.*, **3**, 355.
- Orr, A., D. Cresswell, G.J. Marshall, J.C.R. Hunt, J. Sommeria, C.G. Wang and M. Light (2004), A 'low-level' explanation for the recent large warming trend over the western Antarctic Peninsula involving blocked winds and changes in zonal circulation, *Geophys. Res. Lett.*, **31**, doi:10.1029/2003GL019160.
- Orr, A. G.J. Marshall, J.C.R. Hunt, J. Sommeria, C.-G. Wang, N.P.M. van Lipzig, D. Cresswell and J.C. King (2008), Characteristics of summer airflow over the Antarctic

Peninsula in response to recent strengthening of westerly circumpolar winds, *J. Atmos. Sci.*, **65**, 1396-1412, doi:10.1175/2007JAS2498.1

Overpeck, J.T., B. L. Otto-Bliesner, G.H. Miller, D.R. Muhs, R.B. Alley and J.T. Kiehl (2006), Paleoclimatic evidence for future ice-sheet instability and rapid sea-level rise, *Science*, **311**, 1747-1750, doi:10.1126/science.1115159.

Padman, L., H.A. Fricker, R. Coleman, S. Howard and L. Erofeeva (2002), A new tide model for the Antarctic ice shelves and seas, *Ann. Glaciol.*, **34**, 247–254.

Parkinson, C.L. and D.J. Cavalieri (2012), Antarctic sea ice variability and trends, 1979-2010, *The Cryosphere*, **6**, 871-880, doi:10.5194/tc-6-871-2012.

Pritchard, H.D. and D.G. Vaughan (2007), Widespread acceleration of tidewater glaciers on the Antarctic Peninsula, *J. Geophys. Res.*, **112**, F03S29, doi:10.1029/2006JF000597.

Pritchard, H.D., R. Arthern, D.G. Vaughan and L.A. Edwards (2009), Extensive dynamic thinning on the margins of the Greenland and Antarctic ice sheets, *Nature*, **461**, 971-975, doi:10.1038/nature08471.

Pritchard, H.D., S.R.M. Lichtenberg, H.A. Fricker, D.G. Vaughan, M.R. van den Broeke and L. Padman (2012), Antarctic ice-sheet loss driven by basal melting of ice shelves, *Nature*, **484**, 502-505, doi:10.1038/nature10968.

Ridley, J., W. Cudlip, N. McIntyre and C. Rapley (1989), The topography and surface characteristics of the Larsen Ice Shelf, Antarctica, using satellite altimetry, *J. Glaciol.*, **35**(121), 299-310.

Rignot, E. and D.R. MacAyeal (1998), Ice-shelf dynamics near the front of the Filchner-Ronne Ice Shelf, Antarctica, reveal by SAR interferometry, *J. Glaciol.*, **44**(147), 405-418.

Rignot, E. and S.S. Jacobs (2002), Rapid bottom melting widespread near Antarctic Ice Sheet grounding lines, *Science*, **296**, 2020-2023, doi:10.1126/science.1070942.

Rignot, E., G. Casassa, P. Gogineni, W. Krabill, A. Rivera and R. Thomas (2004), Accelerated discharge from the Antarctic Peninsula following the collapse of Larsen B ice shelf, *Geophys. Res. Lett.*, **31**, doi:10.1029/2004GL0206974.

Rignot, E., J.L. Bamber, M.R. van den Broeke, C. Davis, Y. Li, W.J. van de Berg, E. van Meijgaard (2008), Recent Antarctic ice mass loss from radar interferometry and regional climate modelling, *Nature Geosci.*, **1**(2), 106-110.

Rignot, E., I. Velicogna, M.R. van den Broeke, A. Monaghan and J.T.M. Lenaerts (2011), Acceleration of the contribution of the Greenland and Antarctic ice sheets to sea level rise, *Geophys. Res. Lett.*, **38**, L05503, doi:10.1029/2011GL046583.

- Rist, M.A. (1996), Fracture mechanics of ice shelves, in Filchner-Ronne Ice Shelf Program, Rep. 7., 102-105, Alfred-Wegener Inst. Bremerhaven, Germany.
- Rist, M.A, P.R. Sammonds, S.A.F. Murrell, P.G. Meredith, H. Oerter and C.S.M. Doake (1996), Experimental fracture and mechanical properties of Antarctic ice: preliminary results, *Ann. Glaciol.*, **23**, 284-292.
- Rist, M.A. and P.R. Sammonds (2002), Fracture of Antarctic shelf ice, *J. Geophys. Res.*, **107**(B1), doi:10.1029/2000JB000058.
- Robertson, R., M. Visbeck, A.L. Gordon and E. Fahrbach (2002), Long-term temperature trends in the deep water of the Weddell Sea, *Deep-Sea Res. II*, **49**, 4791-4806, doi:10.1016/S0967-0645(02)00159-5.
- Robin, G. de Q. (1979), Formation, flow and disintegration of ice shelves, *J. Glaciol.*, **24**(90), 259-271.
- Rott, H., P. Skvarca and T. Nagler (1996), Rapid collapse of northern Larsen Ice Shelf, Antarctica, *Science*, **271**, 788-792.
- Sandhäger, H., W. Rack and D. Jansen (2005), Model investigations of Larsen B Ice Shelf dynamics prior to the breakup, *Forum for Research into Ice Shelf Processes (FRISP)*, Rep. **16**, 5-12.
- Scambos, T.A., C. Hulbe, M. Fahnestock and J. Bohlander (2000), The link between climate warming and break-up of ice shelves in the Antarctic Peninsula, *J. Glaciol.*, **46**, 516-530.
- Scambos, T.A., C. Hulbe and M. Fahnestock (2003), Climate-induced ice shelf disintegration in the Antarctic Peninsula, *Antarctic Peninsula Climate Variability*, Ant. Res. Series, **79**, 79-92.
- Scambos, T.A., J.A. Bohlander, C.A. Shuman and P. Skvarca (2004), Glacier acceleration and thinning after ice shelf collapse in the Larsen B embayment, Antarctica, *Geophys. Res. Lett.*, **31**, L18402, doi:10.1029/2004GL020670.
- Scambos, T.A., H.A. Fricker, C.-C. Liu, J. Bohlander, J. Fastook, A. Sargent, R. Massom and A.-M. Wu (2009), Ice shelf disintegration by plate bending and hydro-fracture: Satellite observations and model results of the 2008 Wilkins ice shelf break-ups, *Earth and Planet. Sci. Lett.*, **280**, 51-60, doi:10.1016/j.epsl.2008.12.027.
- Scientific Committee on Antarctic Research (SCAR) (2009), Antarctic climate change and the environment, Scott Polar Research Institute, Cambridge, UK, www.scar.org/publications/.

- Shabtaie, S. and C.R. Bentley (1982), Tabular icebergs: Implications from geophysical studies of ice shelves, *J. Glaciol.*, **28**(100), 413-430.
- Shepherd, A., D. Wingham, T. Payne and P. Skvarca (2003), Larsen Ice Shelf has progressively thinned, *Science*, **302**(5646), 856-859, doi: 10.1126/science.1089768.
- Shepherd, A. et al. (2012), A reconciled estimate of ice-sheet mass balance, *Science*, **338**, 1183-1189, doi:10.1126/science.1228102.
- Shevenell, A.E., A.E. Ingalls, E.W. Domack, and C. Kelly (2011), Holocene Southern Ocean surface temperature variability west of the Antarctic Peninsula, *Nature*, **470**, 250-254, doi:10.1038/nature09751.
- Sinha, N.K. (1978), Short-term rheology of polycrystalline ice, *J. Glaciol.*, **21**(85), 457-473.
- Smith, B.M.E. (1972), Airborne radio echo sounding of glaciers in the Antarctic Peninsula, *Brit. Antarc. Surv. Scien. Rep.*, **72**, 1-11.
- Smith, B.M.E. and S. Evans (1972), Radio echo sounding: Absorption and scattering by water inclusion and ice lenses, *J. Glaciol.*, **11**(61), 133-146.
- Stammerjohn, S., R. Massom, D. Rind and D. Martinson (2012), Regions of rapid sea ice change: An inter-hemispheric seasonal comparison, *Geophys. Res. Lett.*, **39**, L06501, doi:10.1029/2012GL050874.
- Steig, E.J., D.P. Schneider, S.D. Rutherford, M.E. Mann, J.C. Comiso and D.T. Shindell (2009), Warming of the Antarctic ice-sheet surface since the 1957 International Geophysical Year, *Nature*, **457**, 459-463, doi:10.1038/nature07669.
- Steig, E.J., Q. Ding, D.S. Battisti and A. Jenkins (2012), Tropical forcing of Circumpolar Deep Water Inflow and outlet glacier thinning in the Amundsen Sea Embayment, West Antarctica, *Ann. Glaciol.*, **53**(60), 19-28, doi:10.3189/2012AoGG0A110.
- Steig, E.J. et al. (2013), Recent climate and ice-sheet changes in West Antarctica compared with the past 2,000 years, *Nat. Geosci.*, **6**, 372-375 doi:10.1038/ngeo1778.
- Swithinbank, C. (1977), Glaciological research in the Antarctic Peninsula, *Philos. Trans. R. Soc. London, Ser. B.* **279**, 161-184.
- Tapley B.D., D.P. Chambers, S. Bettadpur and J.C. Ries (2003), Large scale ocean circulation from the GRACE GGM01 Geoid, *Geophys. Res. Lett.*, **30**(22), doi:10.1029/2003GL018622.
- Thoma, M., A. Jenkins, D. Holland and S. Jacobs (2008), Modelling Circumpolar Deep Water intrusions on the Amundsen Sea continental shelf, Antarctica, *Geophys. Res. Lett.*, **35**, L18602, doi:10.1029/2008GL034939.

Thompson, D.W.J. and S. Solomon (2002), Interpretation of recent Southern Hemisphere climate change, *Science*, **296**, 895-899, doi:10.1126/science.1069270.

Turner, J., S.R. Colwell, G.J. Marshall, T.A. Lachlan-Cope, A.M. Carleton, P.D. Jones, V. Lagun, P.A. Reid and S. Iagovkina (2005), Antarctic climate change during the last 50 years, *Int. J. Climatol.*, **25**, 279–294.

Turner, J., J.C. Comiso, G.J. Marshall, T.A. Lachlan-Cope, T. Bracegirdle, T. Maksym, M.P. Meredith, Z. Wang and A. Orr (2009), Non-annular atmospheric circulation change induced by stratospheric ozone depletion and its role in the recent increase of Antarctic sea ice extent, *Geophys. Res. Lett.*, **36**, L08502, doi:10.1029/2009GL037524.

van den Broeke, M.R. and N.P.M. van Lipzig (2004), Changes in Antarctic temperature, wind and precipitation in response to the Antarctic Oscillation, *Ann. Glaciol.*, **39**, 119-126.

van den Broeke, M.R. (2005), Strong surface melting preceded collapse of Antarctic Peninsula ice shelf, *Geophys. Res. Lett.*, **32**, doi:10.1029/2005gl023247.

van den Broeke, M.R., C. Reijmer, D. van As and W. Boot (2006), Daily cycle of the surface energy balance in Antarctica and the influence of clouds, *Int. J. Climatol.*, **26**, 1587-1605, doi:10.1002/joc.1323.

van der Veen, C.J. and I.M. Whillans (1989), Force budget: I. Theory and numerical methods, *J. Glaciol.*, **35**, 53-60.

van der Veen, C.J. (1998a), Fracture mechanics approach to penetration of bottom crevasses on glaciers, *Cold Reg. Sci. and Tech.*, **27**, 213-223.

van der Veen, C.J. (1998b), Fracture mechanics approach to penetration of surface crevasses on glaciers, *Cold Reg. Sci. and Tech.*, **27**, 31-47.

van der Veen, C.J. (2007), Fracture propagation as means of rapidly transferring surface meltwater to the base of glaciers, *Geophys. Res. Lett.*, **34**, L01501, doi:10.1029/2006GL028385.

Vaughan, D.G. (1995), Tidal flexure at ice shelf margins, *J. Geophys. Res.*, **100**(B4), 6213-6224.

Vaughan, D.G. and C.S.M Doake (1996), Recent atmospheric warming and retreat of ice shelves on the Antarctic Peninsula, *Nature*, **379**, 328-331.

Vaughan, D.G., G.J. Marshall, W.M. Connolley, J.C. King and R. Mulvaney (2001), Devil in the detail, *Science*, **293**, 1777-1779, doi:10.1126/science.1065116.

Vaughan, D.G., G.J. Marshall, W.M. Connolley, C. Parkinson, R. Mulvaney, D.A. Hodgson, J.C. King, C.J. Pudsey and J. Turner (2003), Recent rapid regional climate warming on the Antarctic Peninsula, *Clim. Change*, **60**, 243-274.

Vaughan, D.G. (2006), Recent trends in melting conditions on the Antarctic Peninsula and their implications for ice-sheet mass balance and sea level, *Arctic, Antarc., Alpine Res.*, **38**(1), 147-152.

Velicogna, I. (2009), Increasing rates of ice mass loss from the Greenland and Antarctic ice sheets revealed by GRACE, *Geophys. Res. Lett.*, **36**, doi:10.1029/2009GL040222.

Vieli, A., A.J. Payne, A. Shepherd and Z. Du (2007), Causes of pre-collapse changes of the Larsen B ice shelf: Numerical modelling and assimilation of satellite observations, *Earth Planet. Sci. Lett.*, **259**, 297-306, doi:10.1016/j.epsl.2007.04.050.

Weertman, J. (1973), Can a water-filled crevasse reach the bottom surface of a glacier? *IAHS Publ.*, **95**, 139-145.

Weertman, J. (1980), Bottom Crevasses, *J. Glaciol.*, **25**(91), 185-188.

Zwally, H.J., J.C. Comiso, C.L. Parkinson, D.J. Cavalieri and P. Gloersen (2002a), Variability of Antarctic sea ice 1979-1998, *J. Geophys. Res.*, **107**(3041), doi:10.1029/2000JC000733.

Zwally, H.J., W. Abdalati, T. Herring, K. Larson, J. Saba, and K. Steffen (2002b), Surface melt-induced acceleration of Greenland ice-sheet flow, *Science*, **297**(5579), 218-222, doi:10.1126/science.1072708.

Zwally, H.J., M.B. Giovinetto, J. Li, H.G. Cornejo, M.A. Beckley, A.C. Brenner, J.L. Saba and D. Yi (2005), Mass changes of the Greenland and Antarctic ice sheets and shelves and contributions to sea-level rise: 1992-2002, *J. Glaciol.*, **51**(175), 509-527.